Proceedings of the 28th Annual Biochemical Engineering Symposium

October 3, 1998

Peter J. Reilly
Editor

Department of Chemical Engineering
College of Engineering
Iowa State University, Ames, Iowa

ISU-ERI-Ames-99269

Proceedings of the Annual Biochemical Engineering Symposium

October 3, 1998

Peter J. Reilly
Editor

Department of Chemical Engineering
College of Engineering
Iowa State University, Ames, Iowa

ISU-ERI-Ames-99269

Preface

This series of Annual Biochemical Engineering Symposia was started in 1971 by Professors Larry E. Erickson of Kansas State University and Peter J. Reilly, then of the University of Nebraska-Lincoln. It is designed for graduate students and occasionally postdoctoral fellows and undergraduates to present the results of their research and the directions of their future work to audiences not so familiar as those at their home institutions but not so seemingly intimidating as those at national professional meetings. It also serves as a vehicle for those engaged in similar lines of research to become acquainted with each other and with each others' work. To that end, discussions both during the meeting and at social events are encouraged. To improve students' skills in the writing of articles, in general those that follow were first drafted by the students who presented the work.

In recent years, the symposium has rotated among the University of Colorado, Boulder; Colorado State University; Iowa State University; the University of Kansas; Kansas State University; the University of Missouri, Columbia; and the University of Oklahoma. This 28th Annual Biochemical Engineering Symposium took place at Iowa State University, Ames, IA, on October 3, 1998. Those attending were the following:

Cargill, Inc., Eddyville, IA:	Bryson N. Bergerud, Weiyu Fan
University of Colorado, Boulder:	Robert Davis, Stephanie Bryant, Ryan Cooper, Jeffrey Heys, Scott Lyman, L. A. Pietryszewski, Rick St. John, Jing Xu
Iowa State University:	Chuck Glatz, Surya Mallapragada, Zivko Nikolov, Peter Reilly, Yutaka Okamoto, Lisa Allen, Yun Bai, Qinglong Chang, Kendall Cradic, Dawn Downey, Zhiliang Fan, Pinghua Feng, Patrick Lawler, Theodore T. Moore, Mark C. Mowry, Xiaojing Pan, Greg Rutkowski, Ian Schneider, Ruta Waghmare, David Wendt, Süleyman Yildirim, Chenming Zhang
University of Kansas:	Nikhil Pednekar, Sridhar Sunderam
Kansas State University:	Larry E. Erickson, Jiang Hu, R. Karthikeyan, Doug Lupher, Noel Nevers, Qizhi Zhang
University of Missouri, Columbia:	Stephanie Münscher, Christine Schramm, Jiuli Zhang

As noted on the following pages, eight papers were delivered orally and twelve posters were exhibited. They covered areas that have strayed substantially from the original emphasis on fermentation kinetics and technology. This of course mirrors the expansion of biochemical engineering into biomedical and genetic engineering, as well as bioremediation. All eight oral presentations are represented here by articles, as are eight of the twelve posters.

Peter J. Reilly Department of Chemical Engineering
2114 Sweeney Hall
Iowa State University
Ames, IA 50011-2230
December 1998
Phone: +1-515-294-5968
Fax: +1-515-294-2689
E-mail: reilly@iastate.edu

Contents

Oral Presentations

Posters

HIGH PRESSURE CRYSTALLIZATION OF PURAFECT SUBTILISIN

Ruta Y. Waghmare[1], Jonathan N. Webb[2], Theodore W. Randolph[2], Maurice A. Larson[1], Charles E. Glatz[1]

[1]Department of Chemical Engineering, Iowa State University, Ames, IA 50011
[2]Department of Chemical Engineering, University of Colorado, Boulder, CO 80309

ABSTRACT

The effect of pressure on crystallization of the protease Purafect subtilisin was studied. No irreversible conformational change or activity loss was observed after subjecting subtilisin to pressure from 0.1 to 200 Mpa, indicating good protein stability in this pressure range. Increasing pressure, however, increased the solubility of subtilisin, and the volume change for crystallization was calculated as +34.3 cm^3/mol. Short exposures to high pressures followed by atmospheric crystallizations did not result in increased crystalline yield, indicating no increased nucleation at high pressure. The linear crystal growth rate dropped as pressure increased from 0.1 to 13.6 MPa. Crystal size distribution (CSD) measurements were obtained in this pressure range for crystallization with agitation, which prevented aggregation. The nucleation and growth rate expressions were obtained by fitting a population balance model to residual supernatant concentration and the final CSD.

1. INTRODUCTION

Interest in the area of high-pressure crystallization was initiated when Visuri et al. found that glucose isomerase (GI) crystallized an order of magnitude faster at 200 MPa than at atmospheric pressure (0.1 MPa) [1]. They attributed the enhanced rate of crystallization at high pressure to increased supersaturation but did not measure the solubilities. Subsequent studies in this area were done only on lysozyme where pressure had a different effect on crystallization. The overall crystallization of lysozyme slowed down as pressure increased [2-8]. However, increasing pressure increased the nucleation rate [5]. The effect of high pressure on solubility still remains unresolved, with some researchers reporting an increase in solubility with pressure [2,6,7] and others reporting unchanged solubility at high pressure [4,8].

The process of crystallization can be represented as the following reaction:

Protein (in solution) $\leftrightarrow$ transition state $\leftrightarrow$ protein (in crystal) [nucleus/growth unit]

The overall reaction is accompanied by volume changes in the protein molecule, the water of hydration, and the bulk solvent. The difference between the volume of protein in crystal and protein in solution is the overall volume change for crystallization, and the volume change between the transition state and the protein in solution is the activation volume.

High pressure can affect the crystallization process by compression of the protein and increased hydration of surface residues of the protein [9], and can also be used as a probe to calculate the volume changes involved in the crystallization process. High-pressure crystallization of subtilisin was studied with the aim of studying the effect of high pressure on the crystallization

of a protein other than GI and lysozyme. Also, the availability of subtilisin mutants would enable further studies on the effect of known structural changes on crystallization.

2. MATERIALS AND METHODS

The starting material for crystallization studies was redissolved crystals (40 mg/ml protein). The first step was the removal of stabilizers by diafiltration with 10mM sodium acetate (NaAc) buffer. NaCl (3% w/v) was added to initiate crystallization. The sample purity was checked using non-denaturing gel electrophoresis followed by Coomassie Blue and silver staining. The samples were heat-sealed in polyethylene vials, which were then put in the high-pressure cells. Activity assays were performed to determine the supernatant protein concentration at the end of the crystallizations.

For crystallization with agitation, the high-pressure cells were isolated and put on a roller that rotated at a speed of 120 rpm. Agitation was used to prevent aggregation. Concentration profiles, CSD measurements, and total number of crystals obtained for crystallization with agitation were used for modeling for the estimation of kinetic parameters. The expressions used for the nucleation and growth processes were

$$G = k_G[(c/s) - 1]^a \quad (1)$$

$$B = k_N[(c/s) - 1]^b * \text{mass of existing crystals} \quad (2)$$

where G and B are the growth and nucleation rates, respectively, c is the concentration, s is the solubility, and k_N and k_G are the nucleation and growth rate constants, respectively. The exponent a for the growth rate expression was determined from the single crystal growth measurements.

The algorithm used for the calculation of kinetic parameters is as follows:

Assume k_N, k_G, b $\leftrightarrow$ calculate $c(t)$, $n(l,t)$, $N(t)$ $\leftrightarrow$ Calculate error $\leftrightarrow$ minimize error by adjusting k_N, k_G, b

where n and N represented the number density and total crystal numbers, respectively.

For the details of materials and methods, the reader is referred to refs. 10 and 11.

3. RESULTS AND DISCUSSION

The activity assays and IR spectra of pressure-treated and untreated subtilisin samples were equivalent, indicating no irreversible conformational changes in subtilisin at high pressure. For a detailed study, the reader is referred to ref. 12.

Subtilisin solubility increased with an increase in pressure from 1.12 mg/ml at 0.1 MPa to 2.93 mg/ml at 68 Mpa, giving a volume change for crystallization as +34.3 cm^3/mol.

Short exposures to high pressure followed by atmospheric crystallizations showed no increase in crystalline yield, indicating no increased nucleation at high pressure (Figure 1). On the

other hand, the overall crystalline yield after 24 h was lower at high pressures than at atmospheric pressure, indicating a decrease in the nucleation rate (Figure 1).

A measurable effect of pressure on the crystal growth rate was seen in the pressure range 0.1 MPa to 13.6 MPa (Figure 2). At higher supersaturations at atmospheric pressure, the growth rate was almost independent of supersaturation, indicating the crystal surface to be saturated with growth units, the incorporation of which is rate-controlling. At lower supersaturations, the growth rate dependence on supersaturation changed to 2.8. Lower growth rates at lower supersaturations have also been reported for lysozyme, where Forsythe et al. [13] explained the decrease of growth rates by the dissociation of growth units at lower supersaturations. The growth rates at high pressure were lower than those at atmospheric pressure, with diffusion as the controlling step at high supersaturations. The difference between the growth rates at atmospheric and high pressure could be due to either a change in conformation of protein at high pressure or differing activation volumes for the steps of surface incorporation and diffusion.

The estimated concentration and CSD profiles for crystallization with agitation are given in Figures 3 and 4, respectively. Increasing ressure decreased the crystallization rate for crystallization with agitation. The estimated kinetic parameters are shown below in Table 1. The growth rate constant, nucleation rate constant, and the total number of crystals decreased as the pressure increased. A higher number of smaller crystals confirmed the assumption of secondary nucleation. Activation volumes for the nucleation and growth processes could not be calculated due to the differences in the dependence of growth rates on supersaturations.

Table 1: Modeling parameters with c_0 = initial concentratio. Growth and nucleation rate expressions are given by equations (1) and (2), respectively.

	0.1 Mpa (c_0 = 39.9 mg/ml)	6.8 Mpa (c_0 = 39.3 mg/ml)	13.6 MPa (c_0 = 37.2 mg/ml)	0.1 Mpa (c_0 = 23.7 mg/ml)
Growth rate constant, k_G	4.4×10^{-8}	2.0×10^{-9}	4.3×10^{-12}	7.3×10^{-8}
Nucleation rate constant, k_N	2.9×10^{3}	1.2×10^{3}	3.5×10^{2}	3.0×10^{3}
Growth rate exponent, a	2.8	4.0	6.0	2.8
Nucleation rate exponent, b	2.45	2.39	2.43	2.47
Total number of crystals calculated after 48 h	5.3×10^{8}	2.8×10^{8}	1.3×10^{8}	2.4×10^{8}

For detailed discussion and results, the reader is referred to refs. 10 to 12.

4. CONCLUSIONS

Subtilsin did not undergo any irreversible conformational change at high pressure. The solubility of subtilisin increased with pressure. Increasing pressure decreased both the nucleation and growth rate for subtilisin. There was a possibility of change in the rate-controlling step at higher

pressures and at lower supersaturations at 0.1 MPa. Crystallization with agitation prevented aggregation and led to secondary nucleation. The kinetic parameters for crystallization were estimated using modeling.

ACKNOWLEDGMENTS

The authors would like to thank NSF (grant number BES-9510302) for funding this project, Mark E. Aument for performing the CSD measurements, and Todd Becker of Genencor International for the generous supply of subtilisin.

REFERENCES

1. K. Visuri, E. Kaipainen, J. Kivimaki, H. Niemi, M. Leisola, S. Palosari, Bio/Technol. 8 (1990) 547.
2. M. Groß, R. Jaenicke, FEBS Lett. 87 (1991) 284.
3. M. Groß, R. Jaenicke, Biophys. Chem. 45 (1993) 245.
4. C. A. Schall, J. M. Wiencek, M. Yarmush, E. Arnold, J. Crystal Growth 135 (1994) 548.
5. M. V. Saikumar, C. E. Glatz, M. A. Larson, J. Crystal Growth 151 (1995) 173.
6. B. Lorber, G. Jenner, R. Giege, J. Crystal Growth 158 (1996) 103.
7. K. J. Takano, H. Harigae, Y. Kawamura, M. Ataka, J. Crystal Growth 171 (1997) 554.
8. M. V. Saikumar, C. E. Glatz, M. A. Larson, J. Crystal Growth 187 (1998) 277.
9. P. Cioni, G. B. Strambini, J. Mol. Biol. 242 (1994) 291.
10. R. Y. Waghmare, J. N. Webb, T. W. Randolph, M. A. Larson, C. E. Glatz, J. Crystal Growth, manuscript to be submitted.
11. J. N. Webb, R. Y. Waghmare, T. W. Randolph, M. A. Larson, C. E. Glatz, J. Crystal Growth, manuscript to be submitted.
12. J. N. Webb, R. Y. Waghmare, T. W. Randolph, M. A. Larson, C. E. Glatz, J. Crystal Growth, manuscript to be submitted.
13. E. L. Forsythe, F. L. Ewing, M. L. Pusey, Acta Cryst. D50 (1994) 614.

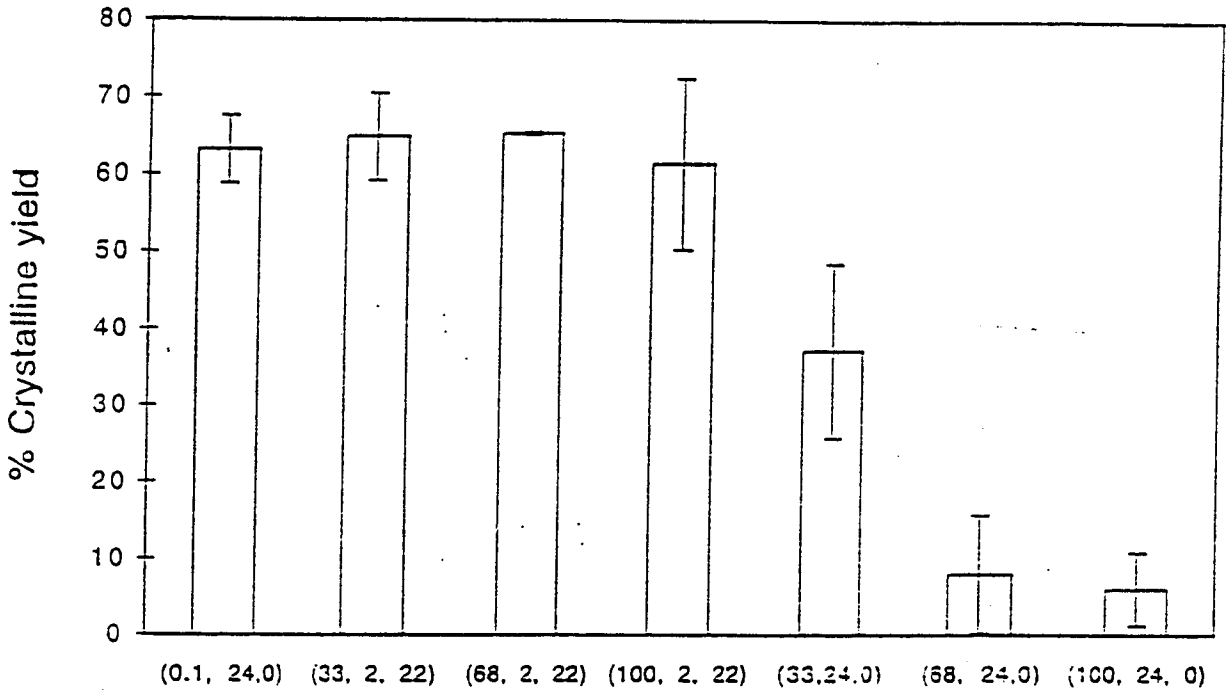

Figure 1: Effect of time and level of pressurization on subtilisin crystallization. Numbers in parentheses are pressure (MPa), time at high pressure (h), and time at atmospheric pressure (h), respectively. The error bars represent 1 standard deviation.

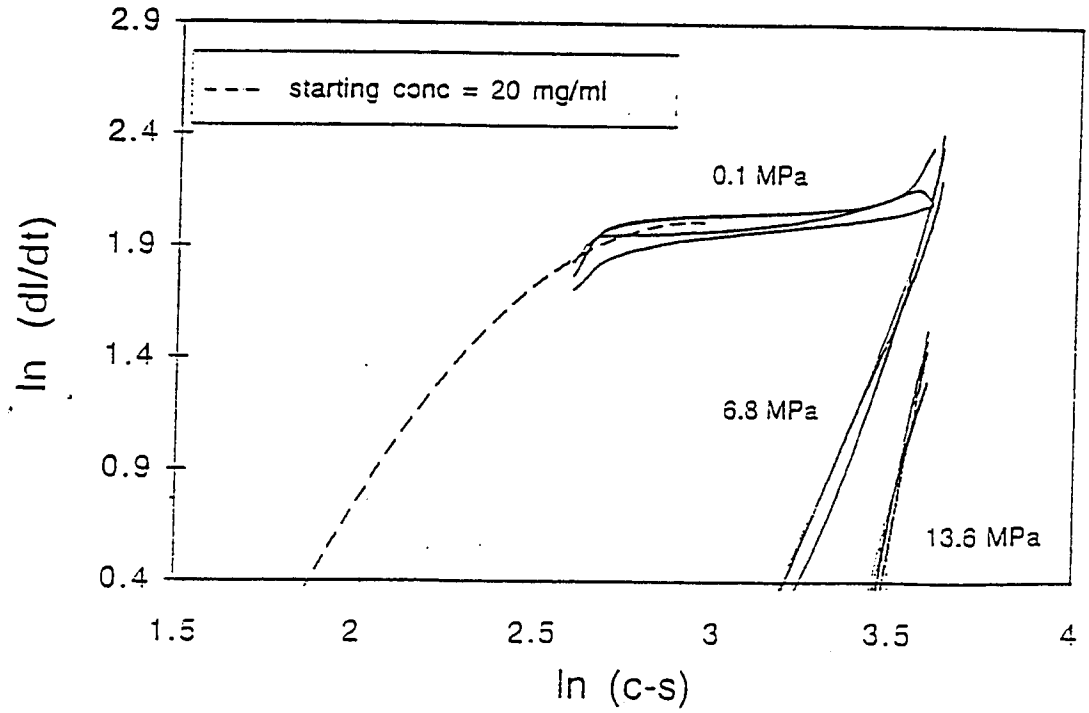

Figure 2: Ln (growth rate) vs. ln (supersaturation) calculated from the curve fits of crystal lengths and concentration vs. time at different pressures. *s* represents the solubility. The growth rate (d*l*/d*t*) is in μm/h and the concentration (*c*) is in mg/ml.

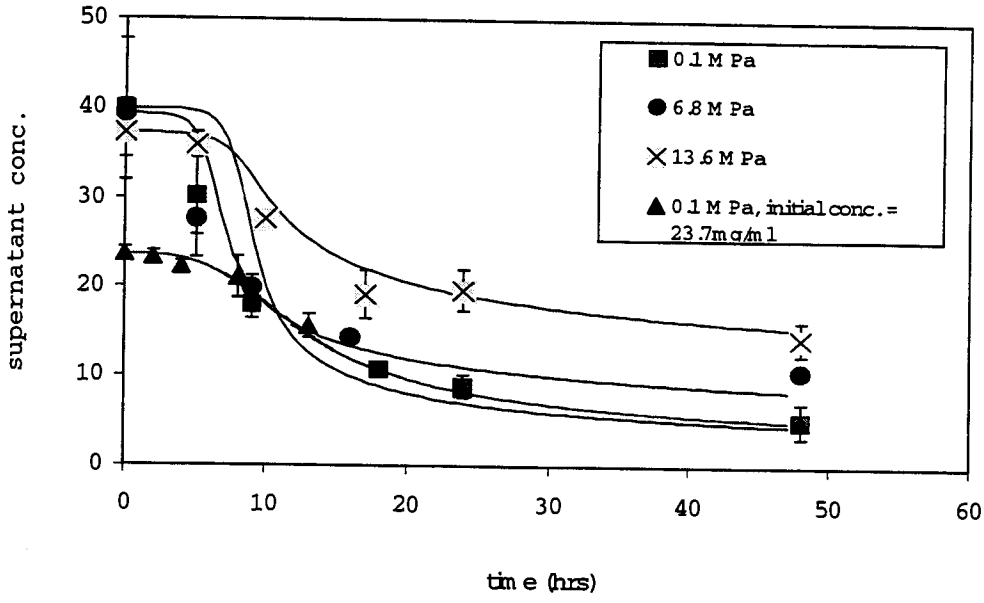

Figure 3: Model calculations (curves) and experimentally observed (points) concentration profiles for crystallization with agitation (speed of agitation = 120 rpm) at various pressures. The error bars represent 95% confidence intervals.

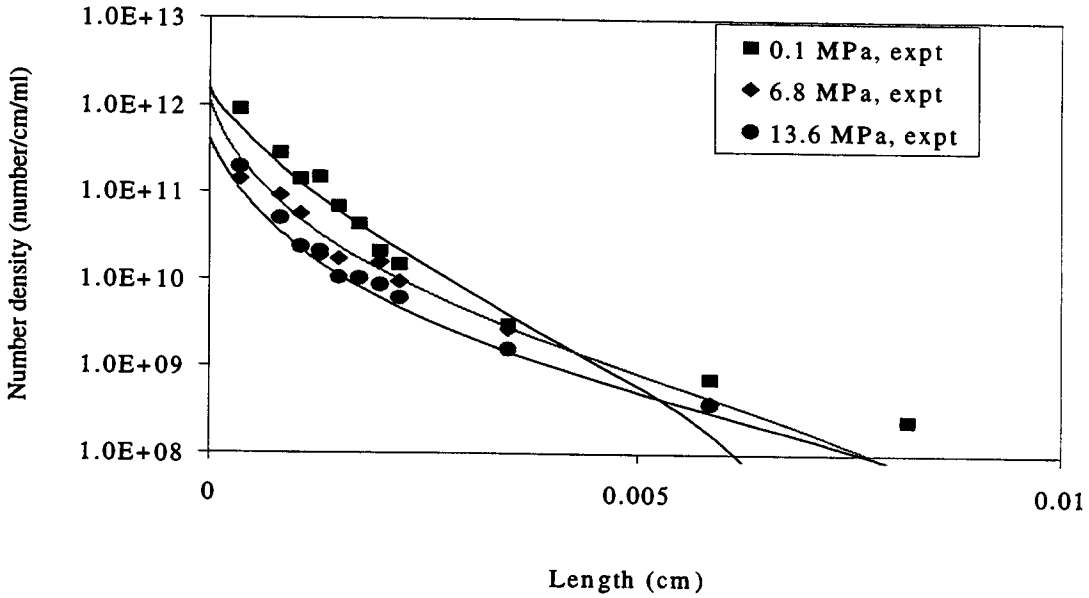

Figure 4: Calculated (curves) and experimentally observed (points) number density profiles for crystallization with agitation (speed of agitation = 120 rpm) at various pressures.

High Pressure Refolding of Protein Aggregates

Richard J. St. John, John F. Carpenter, and Theodore W. Randolph

Center of Pharmaceutical Biotechnology and Department of Chemical Engineering
University of Colorado
Boulder, CO 80309-0424

Abstract

High hydrostatic pressures (1-2 kbar), combined with non-denaturing concentrations of guanidine hydrochloride foster refolding of denatured and aggregated human growth hormone and lysozyme. Full recovery of properly folded protein can be obtained by applying pressures of 2 kbar to suspensions containing 1 mg/mL recombinant human growth hormone aggregates and 0.75M guanidine hydrochloride. Covalently cross-linked, insoluble aggregates of lysozyme could be refolded to native, functional protein at a 70% yield, independent of protein concentration up to 2 mg/mL.

Introduction

Understanding how a polypeptide chain folds into the requisite three-dimensional structure for function remains one of the greatest challenges in science today (1). In spite of recent progress in theoretical and computational approaches, experimental efforts to manipulate protein folding *in vitro* are hampered by competing off-pathway aggregation processes. Protein aggregation itself can have severe consequences in human diseases (*e.g.,* Alzheimer's, glaucoma, and primary emphysema) and in manufacturing, shipping, storage and delivery of protein therapeutics. For instance, if even a minor amount (*e.g.* 1%) of a parenterally delivered protein is aggregated, adverse reactions including anaphylactic shock can be induced.

The formation of non-native protein aggregates from native protein molecules plagues the entire processing, shipping and delivery stream for recombinant protein drugs. Aggregation can occur during purification, concentration, vial filling, freeze-thawing, lyophilization/rehydration and delivery to patients. This is a severe problem for therapeutic proteins that are delivered parenterally, because protein aggregates can cause adverse reactions in patients ranging from sensitization to anaphylatic shock (2-4). Particularly dramatic manifestations of the competition between proper folding pathways and off-pathway formation of non-native aggregates occur during attempts to obtain native recombinant proteins from inclusion bodies or precipitates formed during processing, both of which are essentially completely aggregated protein with substantial non-native structure (5, 6).

Currently, refolding proteins from non-native aggregates and inclusion bodies requires proteins to be disaggregated and then refolded into their native conformation. Most commonly, aggregates are solubilized in a strong chaotrope, such as 8M guanidine hydrochloride (Gdn·HCl) (7-11), which results in nearly complete unfolding of the protein molecules. Once soluble and unfolded, the proteins are first diluted with additional Gdn·HCl solution and then refolded by removing the chaotrope by dialysis or

additional dilution. The refolding step, however, is very difficult and depends strongly on renaturing conditions (11-13). For example, redox conditions, pH, rates of dialysis and protein concentration must all be empirically optimized for each protein (12). Furthermore, because the process of protein folding is first-order in protein concentration and the overall aggregation process is at least second-order, aggregation is favored over refolding at higher protein concentrations. Hence, achieving acceptable yield (*e.g.* > 10%) of refolded protein often requires protein to be refolding at very low concentrations (10-100 μg/mL) (11,12,14,15). As a result, once the proteins are refolded, they must be concentrated (typically 100- to 1000-fold) to final dosage concentrations. Losses of native protein can also occur during this step. In addition, yield of properly folded protein upon renaturation is often low regardless of refolding conditions. Finally, the large volumes of waste chaotrope solution generated are expensive to dispose of properly.

High pressure is an alternative to the use of high concentrations of denaturants. Pressures between 1 and 3 kbar will reversibly dissociate oligomeric proteins into subunits (16-19). Pressures above 4 kbar begin to denature the secondary structure of proteins (20-22). If the pressure effects on aggregates of non-native protein molecules are similar to those on native multimeric proteins, then hypothetically there must exist a "pressure window" where pressure is high enough to solubilize aggregates, but still allow refolding to the native conformation. In order for this effect to be of practical value, it is essential that that the yield of native protein be high (> 50%) upon return to atmospheric pressure.

The purpose of the current study was to address these questions and to determine whether pressure alone or pressure in combination with an appropriate level of chaotrope could be used to refold proteins. We also compared the refolding yields of native protein from insoluble protein aggregates containing different degrees of non-native intermolecular β–sheet structure and scrambled disulfide bonds. The model proteins chosen for this study were recombinant human growth hormone and hen egg white lysozyme.

Materials and Methods

Materials

Recombinant human growth hormone lyophilized in ammonium bicarbonate was obtained from Genentech Inc. Hen egg white lysozyme, three times crystallized, dialyzed and lyophilized (Cat. # L-6876, lot # 65H7025), EDTA (Cat. # E-5134), sodium azide (Cat. # S-8032), and Gdn·HCl (Cat. # G-4505) were obtained from Sigma (St. Louis, MO). Dithiothreitol (DTT) (Cat. # D-5545), glutathione, GSSG (Cat. # G-6654) and *Micrococcus lysodeikticus* cells (Cat. # M-3770) were also obtained from Sigma. Tris base (Cat. # BP152-500) was purchased from Fischer. Sodium citrate (Cat. # 3643-1) was purchased from J. T. Baker.

Aggregation

Lysozyme was aggregated by first unfolding and reducing 40 mg/mL lysozyme in 8M Gdn·HCl and 40mM DTT. Samples were shock-diluted between 10- and 40-fold with 50mM Tris buffer (1mM EDTA, pH 8.0) to induce aggregation. Tris buffer containing

DTT, GSSG, and Gdn·HCl was then added to yield a refolding buffer of 50mM Tris (pH 8.0), 0.8M Gdn·HCl, 5mM GSSG and 2mM DTT.

rhGH was aggregated under two separate buffer conditions: buffer and buffer containing 0.75M Gdn·HCl. Samples were prepared in 10mM sodium citrate buffer (1mM EDTA, 0.1% sodium azide, pH 6.0) at a concentration of 2 mg/mL rhGH. The samples were aggregated by rotating at 8 rpm for 48 h at room temperature (23). Prior to pressurization, samples were diluted to 1 mg/mL rhGH with appropriate Gdn·HCl solutions to yield desired refolding conditions.

Pressure

Pressure was generated using high-pressure nitrogen (6000 psi) connected to equipment from High Pressure Equipment Company (Erie, PA). The nitrogen was connected to a 10-fold hydraulic intensifier, which is connected to a 2-L clover leaf reactor rated to 30,000 psi. Samples were prepared in heat-sealed bulbs of SAMCO® transfer pipettes. Pressure was ramped up over a period of 10 min, while depressurization was conducted at approximately 200 psi/min.

Spectroscopic Analysis

Prior to spectroscopic measurements, all samples were centrifuged for 15 min to remove any insoluble aggregates. Spectroscopic absorbance combined with an extinction coefficient of 1.16 (cm·mg/mL) at 278 nm was used to ascertain the concentration of human growth hormone (23). All spectrophotometer readings were conducted on a Hewlett Packard 8452A diode array spectrophotometer. Measurements were made in general scanning mode, and buffer containing no protein was used as a blank. Contributions due to soluble aggregates were subtracted from the signal as described by Leach and Scheraga (24).

Spectroscopic analysis of lysozyme was used to determine lysozyme concentration in both denatured and renatured solutions. Samples were centrifuged as described above to eliminate insoluble aggregates. Extinction coefficients for denatured and native lysozyme are 2.37 and 2.63 $(cm \cdot mg/mL)^{-1}$, respectively (25). The Hewlett Packard spectrophotometer was used as described above.

Lysozyme Activity Assay

Lysozyme activity was measured by a method similar to the one described by Jolles (26). Exactly 0.25 mg/mL of *M. lysodeikticus* cells were suspended in 67mM potassium phosphate buffer, pH 6.2. All samples were diluted in Tris buffer (pH 8.0, 1mM EDTA) to a concentration between 0.05 and 0.25 mg/mL. Exactly 10 µL of the diluted samples were then mixed into 990 µL of cell suspension just prior to measurement. Absorbance of the sample was measured at 450 nm for 90 s. Linear slopes were calculated on points between 30 and 90 s. Lysozyme concentrations were determined by comparing rate values with those obtained from standard solutions of lysozyme.

Fourier Transform Infrared Spectroscopy (FTIR)

FTIR was used to determine the secondary structure of growth hormone aggregates in solution. All spectra were collected on a Nicolet Magna model 550 spectrometer

equipped with a dTGS detector. A 256-scan interferogram was acquired in single-beam mode with a 4 cm^{-1} resolution. Aggregate slurries were placed in an adjustable path-length IR cell set at 8 μm. The same cell was used to collect a buffer blank (the buffer used for the blank was identical to the buffer in the aggregate slurry). Buffer and water vapor contributions were subtracted from the spectrum using the Nicolet software. Second derivative analysis was used for peak narrowing and resolution. Contributions from the second derivative of the water vapor spectrum were also subtracted from the spectrum. A seven-point smoothing was used to remove white noise, and baseline correction was performed over the amide I region. Finally, specta were normalized by their total area over the amide I region.

Circular Dichroism (CD)

CD was used to analyze the secondary and tertiary structure of dilute protein solutions. CD scans were made on an Aviv Model 62DS spectrometer. Far UV wavelength ranges (180-250 nm) were scanned for secondary structural elements, and near UV wavelength ranges (250-320 nm) were scanned for tertiary structure. In the far UV scan, a protein concentration of approximately 0.1 mg/mL and a path length of 0.1 cm, and in the near UV scan, a protein concentration of 1 mg/mL and a path length of 1 cm, were used. Buffer containing no protein was used as a blank.

Results

Recombinant human growth hormone (rhGH) is a 22-kDa protein formed into a four-α-helix bundle. Its surface contains two relatively large regions with a high percentage of hydrophobic residues (27, 28). Even gentle agitation of rhGH solutions results in aggregation and precipitation of insoluble aggregates (23). The work of Gorovits and Horowitz (29) suggests that aggregates with more structural perturbation are more recalcitrant during refolding experiments. We created insoluble aggregates of rhGH with differing degrees of non-native structure by agitation in buffer alone or in buffer containing 0.75M Gdn·HCl. With either solution condition, 95% of the protein formed insoluble aggregates. The secondary structure of rhGH aggregates was determined by infrared spectroscopy. The second derivative spectra in the conformationally-sensitive amide I region of native and aggregated growth hormone are given in Figure 2. The spectrum of native rhGH is dominated by a strong band at 1654 cm^{-1}, which is due to high proportion of α-helices. The spectrum for the protein aggregated in the absence of Gdn·HCl retains a substantial absorbance at 1654 cm^{-1}, demonstrating partial retention of α-helices. In contrast, in the spectrum for the protein aggregated in the presence of Gdn·HCl, the α-helix band is greatly reduced and broadened. Thus, not only is there a loss in α-helix content, but also the environments of the remaining helices are more heterogeneous than in the native protein. In both protein aggregate spectra, other bands at 1627 cm^{-1}, 1683 cm^{-1} and 1695 cm^{-1}, which are not pronounced in the native protein spectrum, are prominent. The bands at 1627 cm^{-1} and 1695 cm^{-1} are attributed to intermolecular β-sheet structure at the contact regions between protein molecules in the aggregates. Overall, infrared spectroscopy indicates that the structural perturbations relative to the native state are greater for the protein aggregated in the presence of Gdn·HCl.

The effect of pressure on refolding of rhGH from both types of aggregates was examined at a protein concentration of 0.87 mg/mL. In addition, the effects of Gdn·HCl were tested to determine whether chaotropes augment the effects of pressure on dissolving protein aggregates. The range of Gdn·HCl tested (0-1M) was chosen to remain well below the concentrations where, at atmopheric pressure, rhGH begins to unfold or form molten globules (30). At atmospheric pressure, unfolding is first detected at 3.5M Gdn·HCl. Thus, assuming that pressure (up to 2 kbar) does not greatly increase the effectiveness of Gdn·HCl as a denaturant, native rhGH is favored in the presence of the Gdn·HCl concentrations tested here.

At atmospheric pressure and in the absence of GdmHCl, no protein refolding was detected (*i.e.*, 95% of the protein remains aggregated) after 24 h. In contrast, pressurization to 2 kbar for 24 h and return to atmospheric pressure increased soluble protein to 15% (Figure 2). With the aggregates formed by agitation alone, as the concentration of Gdn·HCl increases, the amount of soluble protein recovered after 24 h incubation at 2 kbar increases nearly linearly until approximately 0.7M Gdn·HCl, where the recovery reached a maximum of 100%. The soluble protein was fully native based on examination of far- and near-UV circular dichroism spectra (31) (data not shown), documenting, respectively, that native secondary and tertiary structures were recovered. For samples aggregated in 0.75M Gdn·HCl a similar trend is displayed, but slightly higher Gdn·HCl concentrations (1M) are required to reach 100% recovery of soluble protein. Thus, in agreement with the suggestion by Gorovits and Horowitz (29), it appears that response to pressure will be different for aggregates with different levels of structural perturbation. Control samples, for both aggregate types, maintained at atmospheric pressure had markedly less recovery of soluble protein (Figure 2). The greatest recovery of approximately 40% was noted for the aggregates formed in Gdn·HCl after incubation in the presence of 1M Gdn·HCl.

These surprising results document that neither pressure alone nor Gdn·HCl alone (<1M) is sufficient to allow 100% recovery of native, soluble rhGH. Furthermore, the effect of the combination of factors is synergistic, for reasons that are not clear at this point. Even if the mechanism for this effect is not known, the current results show that it is critical to optimize the concentration of chaotrope used in a pressure-mediated disaggregation and refolding process.

Next, we investigated the effects of duration of pressure exposure on the degree of refolding measured after return to atmopheric pressure (Figure 3). At a given concentration of Gdn·HCl, refolding yields reach a plateau at approximately 24 h in samples exposed to pressure (Figure 3A) as well as those held at atmospheric pressure (Figure 3B). Thus, the values previously shown in Figure 2 all represent results taken after the refolding had reached a maximum for the respective conditions, and 24 h is sufficient to maximize the refolding yields. The existence of the plateaus implies that a steady-state (but nonequilibrium) condition is achieved within 24 h for each Gdn·HCl concentration. There are, thus, undefined kinetic barriers to complete refolding in samples with less than 0.75M Gdn·HCl.

We also examined the effects of varying pressure on rhGH refolding in 0.75M Gdn·HCl. For both types of aggregates, after 24 h of incubation at pressure and return to atmospheric pressure, recovery of soluble protein as a function of pressure increases almost linearly until 100% recovery is achieved at approximately 1.5 kbar (Figure 4).

Proteins containing cysteine can form covalent aggregates with intermolecular disulfide bonds and, potentially, non-native intramolecular disulfide bonds (*i.e.*, "disulfide scrambling"). Clearly, proper refolding of these covalent aggregates cannot be achieved with treatment with chaotrope alone and can be much more complicated than refolding from non-covalent aggregates. Proper refolding of these proteins requires complete reduction of the protein in order to perform the solubilization step. Then, the correct disulfide bonds must be reformed via air oxidation, an oxido-shuffling system, or exposure to mixed disulfides (12). Most frequently, a mixture of low molecular weight thiols such as glutathione (oxidized and reduced) is employed to reshuffle disulfide bonds during refolding (32). Although these conditions have been useful in attempts to refold lysozyme (whose native conformation contains four disulfides) from initially soluble, unfolded molecules, studies on lysozyme inclusion bodies have been less successful (33).

Precipitates of denatured, covalently crosslinked, lysozyme were pressurized to 2 kbar for 48 h and tested for soluble protein and catalytic activity after depressurization. Recovery of catalytic activity is a sensitive indicator of proper refolding and requires reforming of the four proper disulfides in the native conformation. Recovered activity after pressurization increased linearly with lysozyme concentration. Remarkably, at all concentrations tested up to 2 mg/mL, yields of catalytically active protein were approximately 70% (Figure 5). No attempt was made to optimize ratios of oxidized glutathione to dithiothreitol for maximum refolding; it is conceivable that the 30% unrecoverable protein is the result of suboptimal redox conditions. Less than 30% recovery was noted with samples held at atmospheric pressure.

We conclude that pressure, when augmented by subdenaturing Gdn·HCl concentrations, provides a powerful tool for obtaining native protein molecules from insoluble aggregates. This process allows proteins to be refolded from such aggregates at concentrations orders of magnitude greater than reported previously and at yields approaching 100%. All previous refolding studies report strong negative dependence of recovery of native protein on protein concentration (11), even when concentrations were very low (*e.g.* usually 1-50 μg/mL) (11). For example, a study on lysozyme recovery from inclusion bodies required protein concentrations of less than 40 μg/mL (33), while another study on refolding from soluble, denatured lysozyme reported that recovery of active protein dropped from ca. 95% at 50 μg/mL to ca. 25% at 1 mg/L (32). Refolding from a denatured (but not aggregated) protein at concentrations above 1 mg/mL has been achieved, but proper refolding required dialysis from high concentration of denaturant (34). In our new pressure-aided process, denaturant concentrations are low, while protein concentrations and refolding yields are high. Thus, our initial hypothesis that a pressure/denaturant window can be found that fosters disaggregation while allows protein refolding appears to be correct.

References

1. H. J. C. Berendsen, *Science* **282**, 642-643 (1998).
2. C. A. Thornton, M. Ballow, *Arch. Neurol.* **50**, 135-136 (1993).
3. W. V. Moore, P. Leppert, *J. Clin. Endocrinol. Metabol.* **51**, 691-697 (1980).
4. R. E. Ratner, T. M. Phillips, M. Steiner, *Diabetes* **39**, 728-733 (1990).
5. T. Przybycien, J. P. Dunn, P. Valax, G. Georgiou, *Protein Eng.* **7**, 131-136 (1994).
6. K. Oberg, B. A. Chrunyk, R. Wetzel, A. L. Fink, *Biochemistry* **33**, 2628-2634 (1994).
7. A. Mitraki, J. Betton, M. Desmadril, J. Yon, *Eur. J. Biochem.* **163**, 29-34 (1987).
8. N. K. Puri, M. Cardamone, *FEBS Lett.* **305**, 177-180 (1992).
9. K. Vandenbroeck, E. Martens, S. D'Andrea, A. Billiau, *Eur. J. Biochem.* **215**, 481-486 (1993).
10. R. DeLoskey, D. Van Dyk, T. Van Aken, S. Campbell-Burk, *Arch. Biochem. Biophys.* **311**, 72-78 (1994).
11. R. Rudolph, H. Lilie, *FASEB J.* **10**, 49-56 (1996).
12. R. Rudolph, *Modern Methods in Protein and Nucleic Acid Research (*Tschesche, H., ed.*)*, 149-172 (1990).
13. R. Rudolph, *Protein Engineering: Principles and Practice (*J. Cleland and C. Craik, eds.*)*, 283-298 (1996).
14. M. Goldberg, R. Rudolph, R. Jaenicke, *Biochemistry* **30**, 2790-2797 (1991).
15. J. Maachupalli-Reddy, B. Kelley, E. DeBernardez-Clark, *Biotechnol. Prog.* **13**, 144-150 (1997).
16. A. Paladini, G. Weber, *Biochemistry* **20**, 2587-2593 (1981).
17. K. Muller, H. Ludemann, R. Jaenicke, *Biophys. Chem.* **16**, 1-7 (1982).
18. G. Weber, *High Pressure Chemistry and Biochemistry (*R. van Eldik and J. Jonas, eds.*)*, 401-420 (1987).
19. K. Ruan, G. Weber, *Biochemistry* **27**, 3295-3301 (1988).
20. R. Lange, N. Bee, J. Frank, C. Balny, *Prog. Biotechnol.* **13**, 135-140 (1996).
21. G. Tang, K. Ruan, *Prog. Biotechnol.* **13**, 163-166 (1996).
22. T. Yamaguchi, H. Yamada, K. Akasaka, *Prog. Biotechnol.* **13**, 141-146 (1996).
23. N. B. Bam et al. (in press).
24. S. J. Leach, H. A. Scheraga, *J. Am. Chem. Soc.* **82**, 4790-4792 (1960).
25. D. L. Hevehan, E. De Bernardez Clark, *Biotechnol. Bioeng.* **54**, 221-230 (1997).
26. P. Jolles, *Meth. Enzymol.* **5**, 137-140 (1962).
27. A. M. de Vos, M. Ultcsh, A. A. Kossiakoff, *Science* **255**, 306-312 (1992).
28. M. H. Ultsch, W. Somers, A. A. Kossiakoff, A. M. de Vos, *J. Molec. Biol.* **236**, 286-299 (1994).
29. B. M. Gorovits, P. M. Horowitz, *Biochemistry* **37**, 6132-6135 (1998).
30. N. B. Bam, J. L. Cleland, T. W. Randolph, *Biotechnol. Prog.* **12**, 801-809 (1996).
31. CD, .
32. E. De Bernardez Clark, D. Hevehan, S. Szela, J. Maachupalli-Reddy, *Biotechnol. Prog.* **14**, 47-54 (1998).
33. B. Fischer, B. Perry, I. Sumner, P. Goodenough, *Protein Eng.* **5**, 593-596 (1992).
34. Y. Maeda, T. Ueda, T. Imoto, *Protein Eng.* **9**, 95-100 (1996).

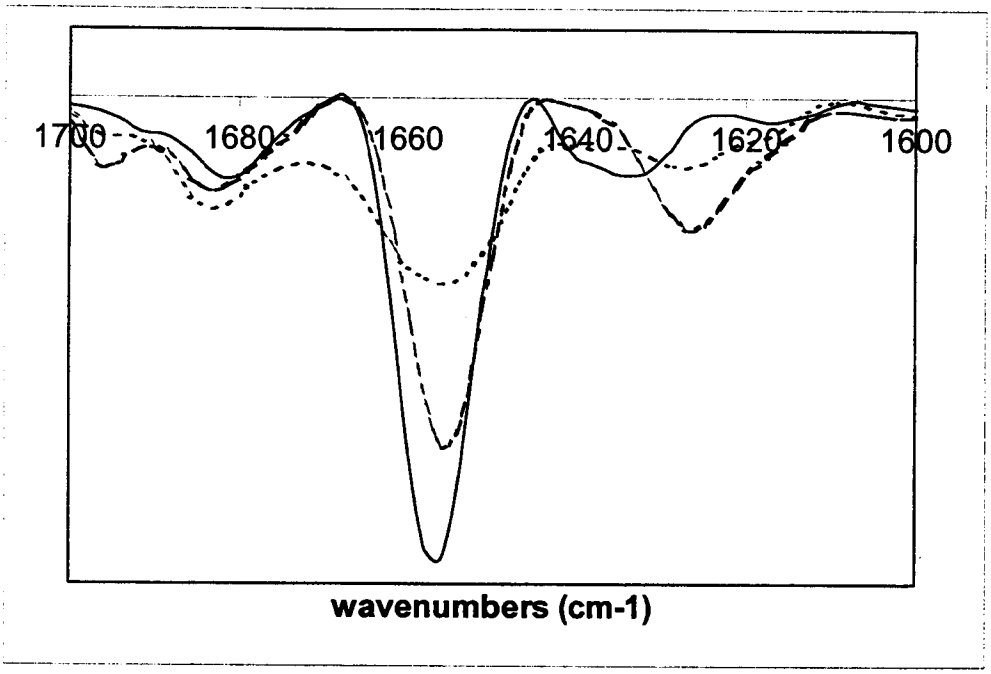

Figure 1: Second derivative FTIR spectra of native recombinant human growth hormone (solid line), growth hormone aggregated in buffer alone (heavy dashed line), and growth hormone aggregated in the presence of 0.75M GdmHCl (lightly dashed line). Spectra for native (reference) and aggregated (reference) protein samples were collected and processed (reference) as previously described.

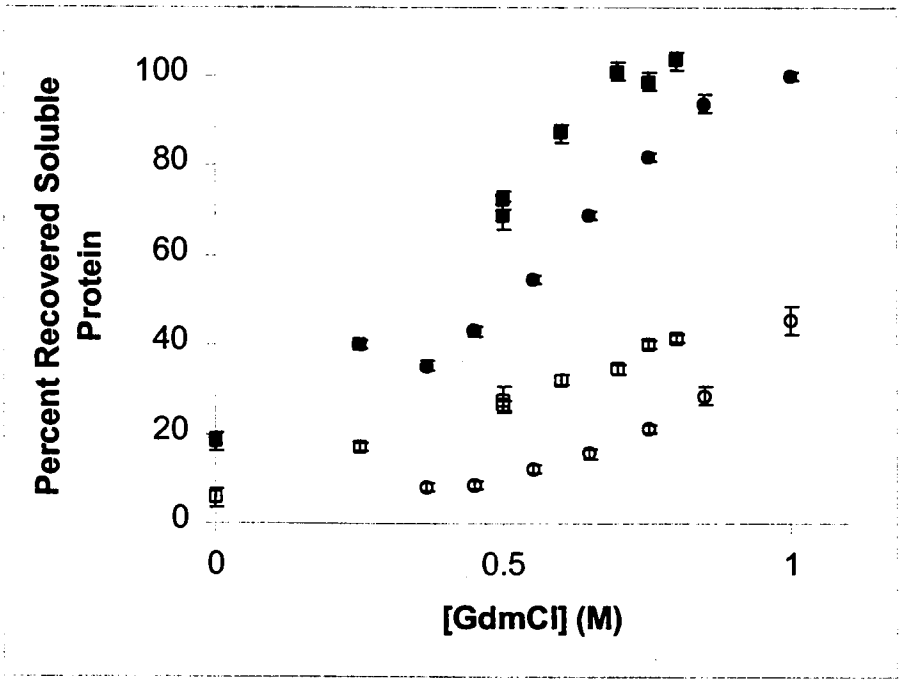

Figure 2: Percent recovered soluble rhGH as a function of GdmHCl concentration. Squares represent samples aggregated in buffer (10mM NaCitrate (6.0), 1mM EDTA, 0.1% NaN3) alone. Circles represent samples aggregated in 0.75M GdmHCl. Outlined points (○,□) represent atmospheric samples and solid points (●,■) represent samples pressurized to 2 kbar for 24 hours. In this and the following figures. error bars represent +/- 1 standard deviation, with data points taken at least in triplicate. Points with no apparent error bars have error bars smaller than the size of the data marker.

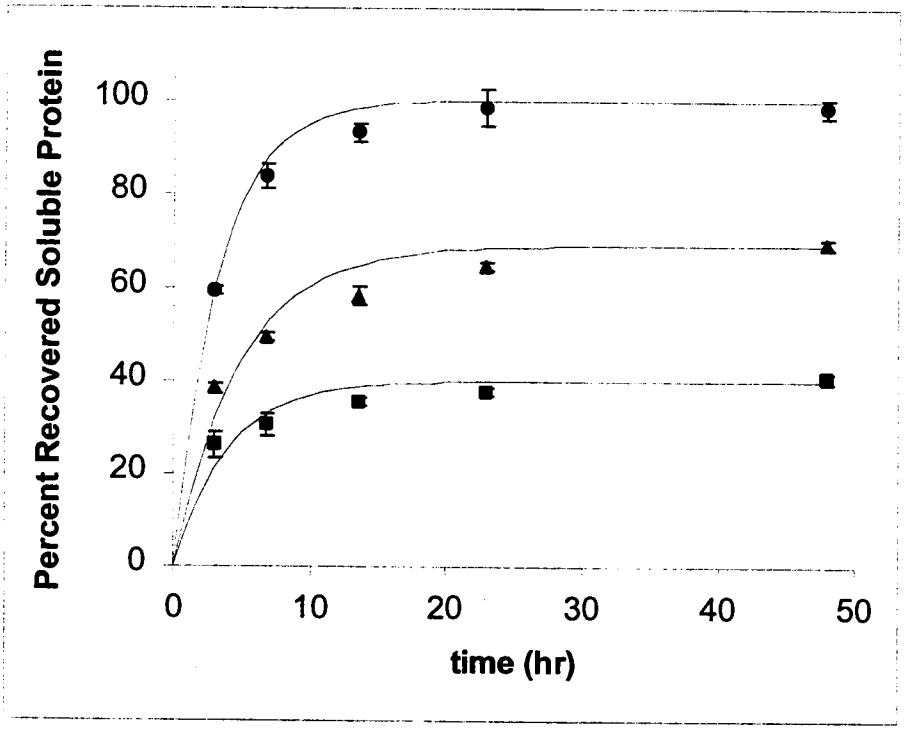

Figure 3a: Percent recovered soluble rhGH as a function of time under 2kbar. All protein was aggregated in buffer (10mM NaCitrate (6.0), 1mM EDTA, 0.1% NaN3) alone. Squares (■) represent samples refolded in 0.25M GdmHCl, triangles (▲).represent samples refolded in 0.5M GdmHCl, and circles (●) represent samples refolded in 0.75M GdmHCl.

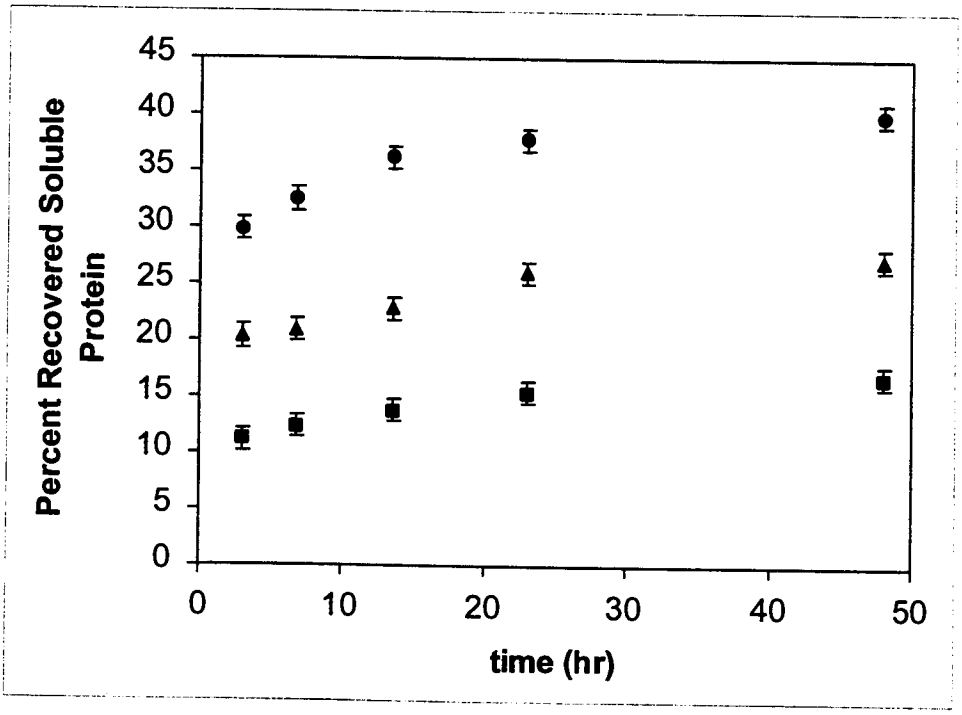

Figure 3b: Percent recovered soluble rhGH as a function of time under atmospheric pressure. All protein was aggregated in buffer (10mM NaCitrate (6.0), 1mM EDTA, 0.1% NaN3) alone. Squares (■) represent samples refolded in 0.25M GdmHCl, triangles (▲).represent samples refolded in 0.5M GdmHCl, and circles (●) represent samples refolded in 0.75M GdmHCl.

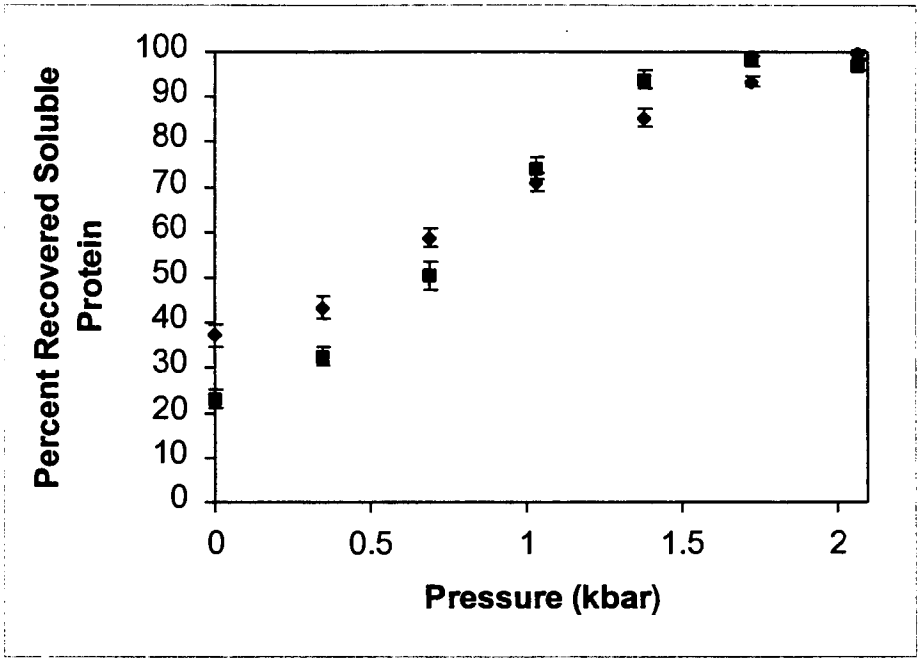

Figure 4: Percent recovered soluble rhGH as a function of pressure. Samples were refolded in 0.75M guanidine-HCl and pressurized for 24 hours. Squares (■) represent samples were aggregated in buffer (10mM NaCitrate (6.0), 1mM EDTA, 0.1% NaN3) alone. Diamonds (◆) represent samples aggregated in 0.75M GdmCl. The dashed line merely assists in distinguishing the data; no mechanistic interpretation is implied

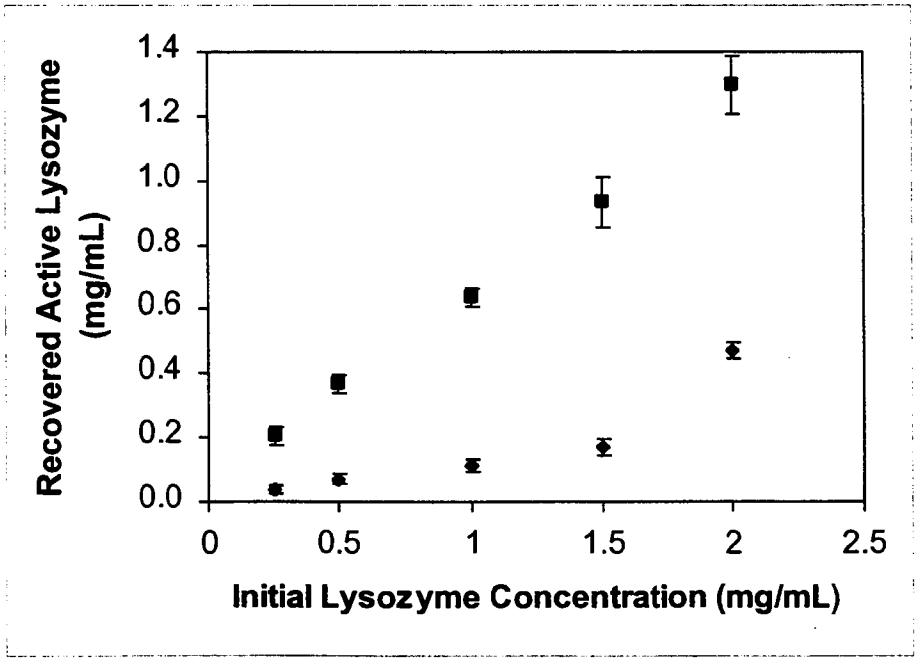

Figure 5: Recovered active lysozyme vs. initial lysozyme concentration. Refolding buffer of 50mM tris (8.0), 0.8 M GdmHCl, 1mM EDTA, 5mM GSSG, and 2mM DTT was used. Diamonds (◆) represent atmospheric samples and squares (■) represent samples pressurized to 2 kbar for 48 hours.

Purification of β-glucuronidase and its fusions from spiked canola protein extract by anion exchange chromatography

Chenming Zhang and Charles E. Glatz
Department of Chemical Engineering
Iowa State University
Ames, IA 50011

ABSTRACT

This paper continues our work on exploring the possibility of using canola as a recombinant protein production host. Native canola proteins were characterized by chromatography on alternative anion exchange resins to choose ones providing the best "gaps" to which recombinant proteins could be engineered to elute. We genetically engineered three β-glucuronidase (GUS) fusion proteins containing polyaspartic acid tails to test the effect of charge on the recovery by anion exchange chromatography from the canola system. The fusion proteins, designated GUSD5, GUSD10, and GUSD15, were constructed with C-terminal tails of 5, 10, and 15 aspartic acid residues, respectively. Purified proteins from an *Escherichia coli* fermentation were spiked into canola protein extract for anion exchange chromatography experiments. The stability of different fusions in canola protein extract was also addressed to provide information on the effect of the length of the fusion tail on the enzymatic activity and stability of the protein.

INTRODUCTION

Plants as recombinant protein production hosts have many attractions. As they can carry out post-translational processes properly, it is easy to scale up their production, and methods for plant harvesting, transporting, and storing have been well established. Many proteins have been expressed in various plants, for example, avidin in corn (Hood et al., 1997), erythropoietin in tobacco (Matsumoto et al., 1993), and phytase in tobacco (Verwoerd et al., 1995). However, there still are two major challenges to face in using transgenic plants as recombinant protein production hosts. One is to increase target protein expression to the highest level possible, and the other is to develop efficient downstream processes to recover the target protein from a large quantity of biomass. This paper deals with the second challenge.

Canola is an interesting plant. It is a traditional oil source, and it has a fairly simple protein composition. Its proteins are composed of mainly two groups:12S protein, which has an average molecular weight of 300 kDa and a pI value of 7.2; and 2S protein, which has an average molecular weight of 12-17 kDa and a pI value of no less than 10.

The scope of this work is to chromatographically investigate the possibility of using canola as a recombinant protein production host, and to test the feasibility of purifying a modified target protein from canola protein extract by anion exchange chromatography.

Experimental procedures

The whole experimental process can be illustrated by Fig. 1.

Target protein

The target protein for this experiment is β-glucuronidase (GUS) from *E. coli*. This protein is absent from most plants, and it is very stable. It is a tetramer, and its molecular weight is about 270 kDa. It has a pI value of 5.5, estimated from its amino acid sequence. From the wild-type GUS, we developed a series of fusion GUS with 5, 10, or 15 aspartic acid residues attached to the C-terminal of each monomer, and they are designated as GUSD0 (wild-type GUS), GUSD5, GUSD10, and GUSD15, respectively. The charges of each protein at pH 7.0 are estimated by

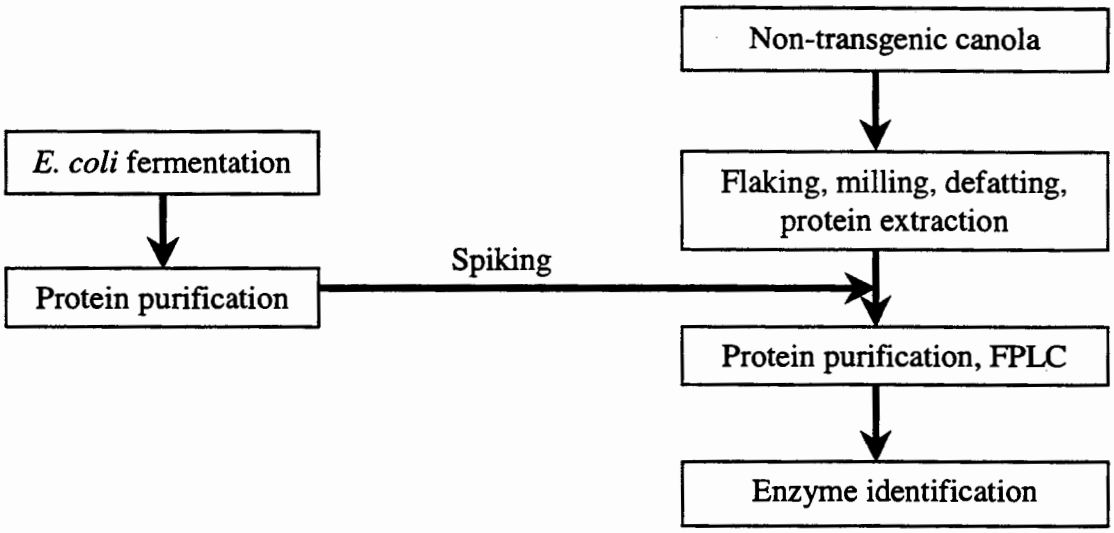

Figure 1. Schematic illustration of experimental procedures.

the Henderson-Hasselbalch equation based on their amino acid compositions and are summarized in Table 1.

Table 1. The estimated charge of GUS and its fusions.

Mutants	No. of aspartates on tail	Estimated charge at pH 7.0
GUSD0	0	-75
GUSD5	5	-95
GUSD10	10	-115
GUSD15	15	-135

RESULTS AND DISCUSSION

1. *Native canola proteins on anion exchange chromatography (AEC)*

Figure 2 shows the native canola protein profile on different anion exchangers, while Figure 3 is the native canola protein profile on Q-Sepharose fast flow singled out from Figure 2. The three arrows point to possible sites on the target protein. It is worth mentioning that major purification has been achieved by just passing a canola sample through the selected anion exchangers because of the huge wash peak before salt gradient elution starts, assuming the target protein would bind to the column under experimental conditions (pH 7.0).

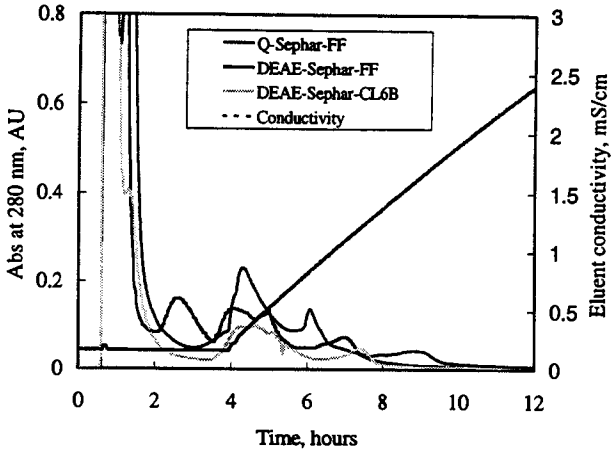

Fig. 2. Native canola protein elution profiles on different anion exchangers.

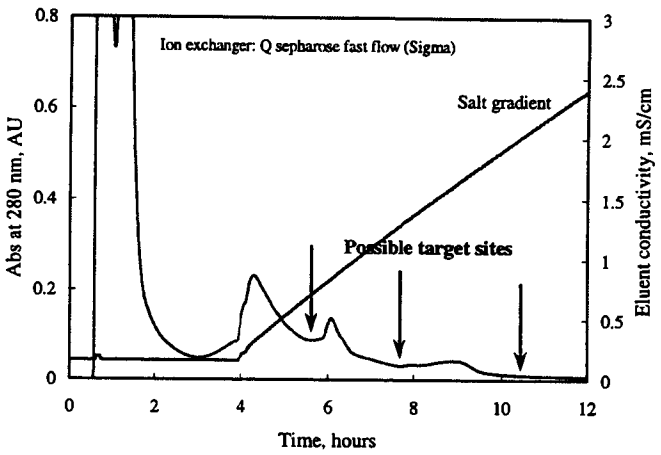

Fig. 3. Native canola protein profile on Q-Sepharose fast flow. Arrows point to possible sites to target a genetically engineered protein.

2. *Beta-GUS stability in canola protein extract*

Concerning the possible effects from native canola protein extract on GUS and its fusions, such as precipitation, protease functioning on proteins and fusion tails, and inhibition, the stability of GUS in canola extract was tested. Figure 4 shows the results.

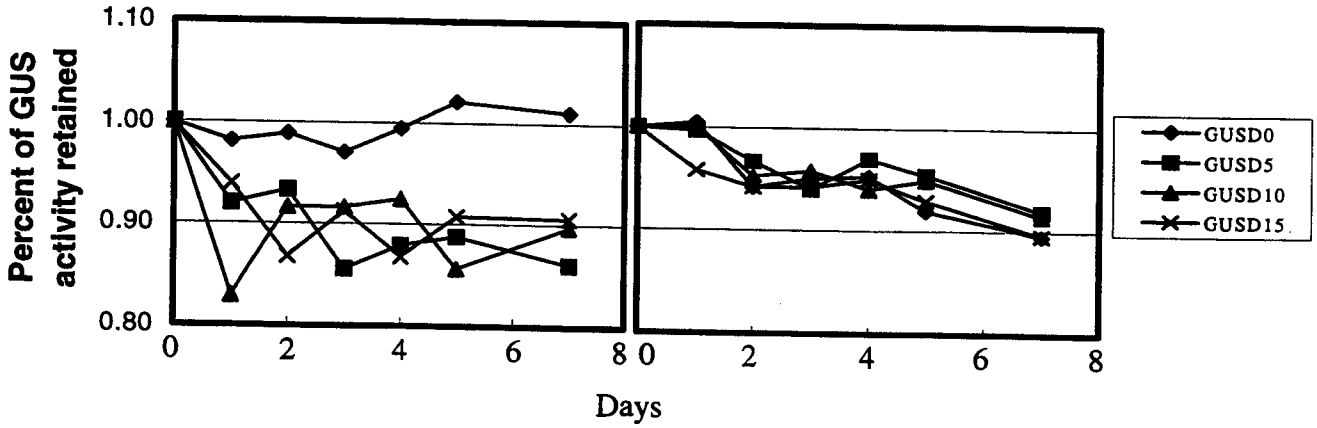

Fig. 4. GUS stability in canola protein extract. The figure on the left shows control samples in storage buffer, 50 mM NaPi (pH 7.0). The figure on the right is GUS-spiked canola samples.

3. *GUS-spiked canola samples on AEC*

Figure 5 shows the chromatographic profiles of different GUS-spiked canola protein samples, and Figure 6 is the enlarged view of the boxed area in Figure 5 with peaks corresponding to GUS activity of different fusions.

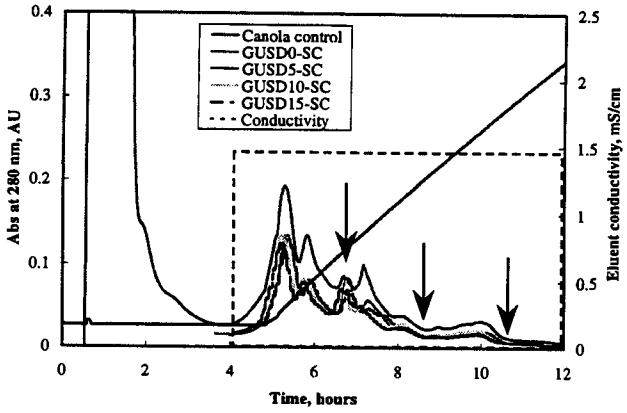

Fig. 5. Elution profiles of GUS spiked canola samples. Arrows point to possible sites to target an interested protein.

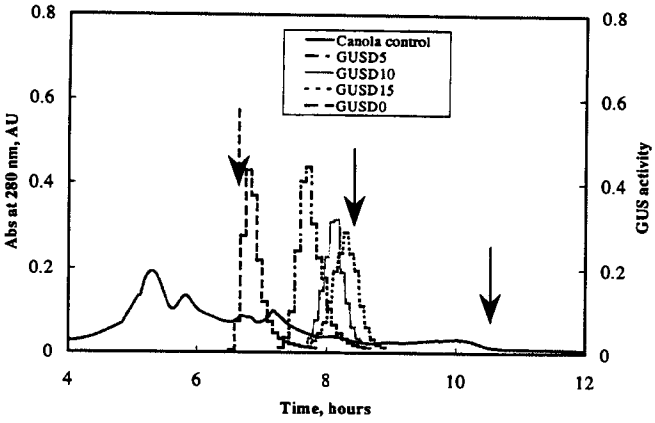

Fig. 6. Superimpose of GUS activity of different fusions on native canola protein profile (boxed area in Fig. 5).

From Fig. 6, wild-type GUS is eluted out at the first target site, meanwhile GUSD10 and D15 are eluted at the second target site. In addition, negatively charged fusion proteins behave better (sharper activity peaks) than positively charged fusion proteins (Zhang and Glatz) during chromatographic processes.

4. *Purification efficiency of possible target sites*

The purification efficiency is a measure of the native canola protein contamination level on the possible target sites. The efficiency of the first two target sites was examined by carrying out SDS-PAGE on various GUS fusions (Fig. 7).

From Figure 7 a-d), it is easy to see that the native canola protein contamination level decreases along with the increase of number of aspartic acid in the fusion tail. At the first target site where wild-type GUS (GUSD0) was eluted, the native canola protein contamination level is the highest. However, when the attached fusion tail has moved the GUS to the second target site, the contamination from native canola protein has been significantly decreased. It is evident for the case of GUSD10 and GUSD15.

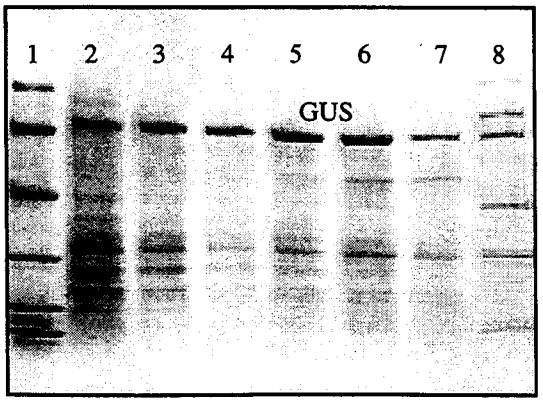

a) GUSD0-SC

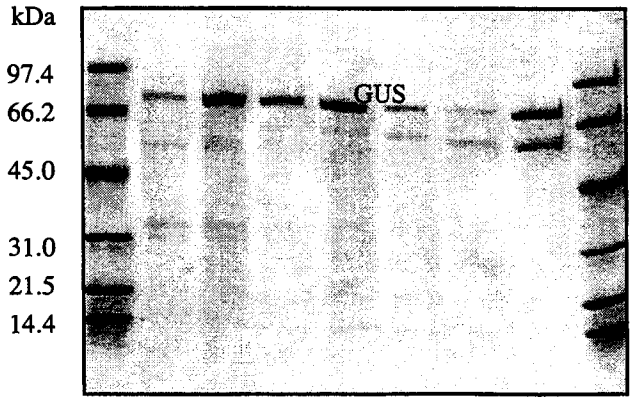

b) GUSD5-SC

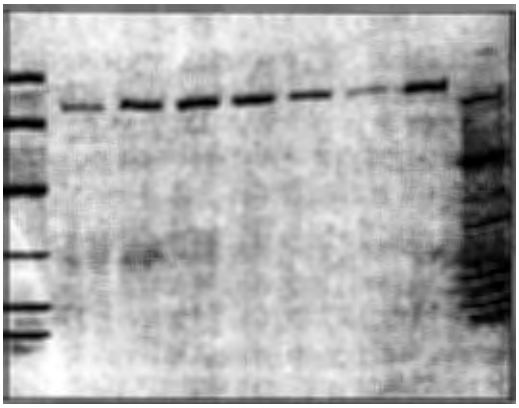

c) GUSD10-SC

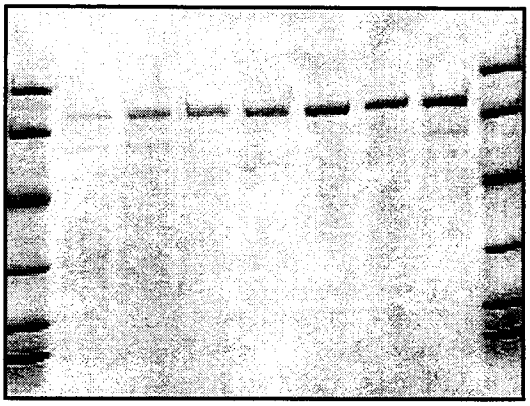

d) GUSD15-SC

Fig. 7. SDS-PAGE of six fractions (lanes 2-7) showing highest GUS activity in Fig. 6 from different GUS fusion-spiked canola samples. All fractions have been concentrated ~17 times prior to SDS-PAGE. Lanes 1 and 9 (except a)) are molecular markers, and lane 8 is the corresponding GUS protein stock solution used in spiking experiments.

The recovery and enrichment ratio of each GUS fusion based on the six fractions mentioned above are tabulated in Table 2:

Table 2. GUS recovery from each fusion spiked canola sample.

Protein sample	Initial specific activity, U/mg	Final specific activity, U/mg	Yield %	Enrichment ratio
GUSD 0-SC	690	37973	76.6	55
GUSD 5-SC	451	44239	70.3	98
GUSD 10-SC	331	49667	70.3	150
GUSD 15-SC	422	80076	53.4	190

Total protein loaded in each experiment is 70.49 ± 0.25 mg.

Table 2 shows the same results as in Fig.7. GUSD0 has the lowest enrichment ratio; however, when the protein is moved to the second target site at higher salt concentration during elution, the enrichment ratio has been significantly increased. In the case of GUSD15, the enrichment ratio has been increased almost four times compared to GUSD0. The low yield of GUSD15 is misleading. Because of the wider spread of the GUS activity for GUSD15, higher yield (~70%) would have been reached if more fractions had been included in the recovery calculation without sacrificing too much of the final protein purity.

CONCLUSIONS

This study indicates that canola is suitable to be used as a host for producing negatively charged proteins. As a target protein, GUS and its fusions are stable in canola protein extract. With a fusion tail of more than 10 aspartate residues, GUS can be purified by single-step anion-exchange chromatography with high purity. In addition, the target site with intermediate eluent conductivity is accessible and provides a significant possibility of single-step purification.

ACKNOWLEDGEMENT

This work was funded by NSF Grant # BES9522644 and USDA NRICGP Grant # 95031130. We would also like to thank ProdiGene Inc., College Station, TX for providing GUS and its fusions and Pioneer Hi-Bred International, Johnston, IA for providing non-transgenic canola seed.

REFERENCES

Hood, E.E., Witcher, D.R., Maddock, S., Meyer, T., Baszcynski, C., Bailey, M., Flynn, P., Register, J., Marshall, L., Bond, D., Kullisek, E., Kusnadi, A., Evangelista, R., Nikolov, Z., Wooge, C., Mehigh, R.J., Hernan, R., Kappel, W.K., Ritland, D., Li, C.-P., Howard, J.A., Commercial production of Avidin from transgenic maize: Characterization of transformant, production, processing, extraction and purification, *Mol. Breed.*, in press.

Matsumoto, S., Ishii, A., Ikura, K., Ueda, M.. and Saski, R., Expression of human erythropoietin in cultured tobacco cells, *Biosci. Biotechnol. Biochem.*, 57 (1993) 1249-1252.

Verwoerd, T.C., van Paridon, P.A., van Ooyen, A.J.J., van Lent, J.W.M., Hoekema, A., Pen, J., Stable accumulation of *Aspergillus niger* phytase in transgenic tobacco leaves, *Plant Physiol.*, 109 (1995) 1199-1205.

Zhang, C. and Glatz, C.E., Genetic engineering strategy for recombinant protein recovery from canola by cation ion exchange chromatography, submitted to *Biotechnol. Prog.*

Biodegradation and Remediation of Methyl *tert*-Butyl Ether

Qizhi Zhang[1], Lawrence C. Davis[2], and Larry E. Erickson[1], Departments of [1]Chemical Engineering and [2]Biochemistry, Kansas State University, Manhattan, KS 66506

Abstract

Several factors make methyl *tert*-butyl ether (MTBE) an important groundwater contaminant. Besides its widespread use, MTBE is more mobile, persistent, and has the potential to occur at much higher concentrations in water than other gasoline species. Although MTBE has been suggested to be resistant to biodegradation, a review of recent studies of biodegradation of MTBE indicates that *in situ* biodegradation may be an effective remediation alternative for soil and groundwater contaminated with MTBE. While many of the studies indicate aerobic decay of MTBE, little evidence of MTBE degradation under anaerobic conditions has been found. Most MTBE degradation occurred under controlled conditions for the particular culture, and needed a long acclimation period. Using an experimental channel system, we studied the fate and transport of MTBE in groundwater under vegetation conditions, and found that vegetation helped to bring MTBE up from the groundwater into the atmosphere. A further study is going on by introducing strains capable of degrading MTBE into the vegetated channel system.

Introduction

Methyl *tert*-butyl ether (MTBE), with a systematic name of 2-methoxy-2-methyl propane, is a colorless, flammable liquid with a strong distinctive odor (Duffy et al., 1992). It is synthesized from methanol plus butylene.

As an octane-enhancing replacement for tetraethyl lead, MTBE was originally approved in 1979 for use in the United States, primarily in mid- and high-grade gasoline, at concentrations as high as 8% by volume. Since the mid-1980's, it has been widely used throughout the country for this purpose. It is also used as a fuel oxygenate at higher concentration (11-15% by volume) as part of the USEPA's programs to reduce ozone and carbon monoxide levels to meet the requirements of the 1990 Clean Air Act Amendments (CAAA) in the most polluted areas of the country. The increase in molecular oxygen for fuels containing oxygenates results in fewer products of incomplete combustion, which are responsible for many problems in urban air quality. MTBE is the most widely used oxygenate in fuel because of its favorable transfer and blending characteristics, ease of production, and low cost.

MTBE is used in approximately fifteen states to meet air quality requirements. In oxygenated fuels for winter use, the amount of MTBE added is 2.7% oxygen by weight or 15% by volume. In reformulated fuels for year-round use, the amount is 2% oxygen by weight or 11% by volume.

The environmental properties, behavior, and fate of MTBE have been documented by Squillace et al. (1997). Table 1 lists the physical and chemical properties of MTBE. MTBE is highly soluble in water, with a solubility of 51.26 g/L. The organic carbon-based partition coefficient (K_{oc}) is 12.3 or 11.0, indicating that MTBE does not adsorb strongly to carbon or soil particles and is likely to be very mobile in the subsurface.

Table 1. Physical and chemical properties of MTBE (from Squillace et al., 1997 except where otherwise noted)

Physical state	Colorless liquid
Molecular formula	$C_5H_{12}O$
Molecular weight	88.15
Melting point	-109°C
Boiling point	55.2°C
Water solubility	51.26 g/L @ 25°C
density	0.7404 @ 25°C
K_{oc}	12.3; 11.0 (estimated)
Log K_{ow}	1.24
Vapor pressure	245 mm Hg @ 25°C (Budavari et al., 1989)
Henry's Law constant	0.0216 at 25°C (Robbins et al., 1993)
Odor threshold	15-40 ppb
Taste threshold	40-140 ppb
Volume in gasoline	Up to 15%
Water solubility when in gasoline	Up to 5100 ppm

MTBE Contamination

In recent years, the persistence of MTBE in groundwater has been observed (Angel, 1991; Garrett et al., 1986; McKinnon and Dyksen, 1984; Newman, 1995; Oil & Gas Journal, 1995; Squillace et al, 1996; Taylor and O'Brien, 1993; and Worthington and Perez, 1993). MTBE has been found in drinking water supply wells for the City of Santa Monica, Cal. The city has had to shut down all its wells and truck in fresh water from Los Angeles (Ballard and Landwehr, 1998). Recently MTBE was banned in the state of Maine, as reported by National Public Radio.

MTBE was reported as the second most frequently detected volatile organic compound of 60 compounds measured in urban areas, and the seventh most frequently detected VOC in samples of stormwater (Squillace et al., 1996). Possible sources of MTBE in groundwater include point sources, such as leaking storage tanks, and nonpoint sources such as recharge of precipitation and stormwater runoff.

In 1987, MTBE was identified by the USEPA for priority testing because of its large production volume, potential widespread exposure, and limited data on long-term health effects (Duffy et al., 1992). Because MTBE does not bind well to soil and is highly soluble in water, it can migrate with groundwater rapidly (EPA, 1998). In an Army Aberdeen Proving Ground field site study, the baseline contour maps indicated that MTBE migrated approximately 1.5 times the distance the BTEX constituents migrated in an unspecified length of time (Damera et al., 1997). Accidental spills of gasoline containing MTBE or leaks from storage tanks can pose a hazard to groundwater supplies.

Like most gasoline compounds, MTBE is a skin and eye irritant that possesses a highly detectable odor (Garrett et al., 1986). Oral ingestion of MTBE can be expected to produce nausea, vomiting, coughing, bronchitis, and sedation. At sufficient concentrations, MTBE is likely to act

as a respiratory and nervous system depressant. The U.S. EPA has classified MTBE as a possible human carcinogen. EPA is currently considering a drinking water health advisory standard in the range of 20-200 ppb (20-200 µg/L) (EPA, 1997).

Biodegradation of MTBE

Poor biodegradability of MTBE has been generally supported by laboratory testing of anaerobic biodegradation (Suflita and Mormile, 1993) and by both bench- and field-scale tests of aerobic biodegradation (API, 1994b). Some evidence suggests that MTBE can biodegrade in the subsurface very slowly.

Recent studies have shown that enhanced or cultured microbial populations can consume enough MTBE to be used in biotreatment systems (Salanitro et al., 1994). Biodegradation of MTBE by pure or mixed bacterial cultures has been reported in several laboratory studies. Two MTBE-degrading cultures have been identified by Salanitro et al. (1994) and Mormile et al. (1994). From acclimated sludge, Salanitro et al. (1994) isolated an aerobic consortium that used MTBE as the sole source of carbon. MTBE was degraded to *tert*-butyl alcohol (TBA), which was subsequently degraded by the enrichment culture.

Lee (1986) conducted one of the first studies on the degradation of MTBE (and the only one to have shown aerobic decay by soil organisms). Using soil from a site in Traverse City, Mich., 84% of the initial MTBE was degraded after four weeks in an aerobic environment. Soil from another location along the Texas Gulf Coast showed no capacity for MTBE degradation after eight weeks of aerobic incubation.

Salanitro et al. (1994) were able to enrich a mixed bacterial culture for degrading MTBE. The bacterial enrichment was derived from an industrial chemical plant biotreater sludge. While none of the individual bacteria in this culture used MTBE as the sole carbon source, the culture as a whole was able to convert radiolabeled MTBE to $^{14}CO_2$ and radiolabeled cell mass. The aerobic degradation of MTBE was significant. In batch experiments, the culture was capable of degrading 120 mg/L of MTBE within 4 h at a rate of 34 mg MTBE/g cells-h. In addition, their results showed that TBA was a metabolic product of MTBE. TBA also decreased but at a slightly slower rate (14 mg TBA/g cells-h). These results give strong evidence of MTBE degradation under controlled conditions for a particular culture, but do not necessarily support the likelihood of MTBE degradation in natural environments. In addition, the mechanism for the initial oxidative attack on MTBE is still unknown.

Steffan et al. (1997) tested several propane-oxidizing bacteria for their ability to degrade gasoline oxygenates, including MTBE, ethyl *tert*-butyl ether (ETBE), and *tert*-amyl methyl ether (TAME). Both a laboratory strains and natural isolates were able to degrade each compound after growth on propane. One of the strains converted greater than 60% of the added labeled [^{14}C] MTBE to $^{14}CO_2$ in less than 30 h. MTBE was oxidized to TBA by camphor-grown *Pseudomonas putida* CAM. Rates of MTBE degradation by propane-oxidizing strains ranged from 3.9 to 9.2 nmol/min-mg of cell protein at 28°C. Based on their results, these authors proposed that the use of propanotrophs for MTBE treatment could potentially provide new remediation alternatives.

An aerobic mixed culture has been developed that is capable of degrading MTBE as sole carbon and energy source, and mixtures of MTBE, benzene, and toluene showed enhanced MTBE degradation due to growth of the culture on benzene and toluene (Park and Cowan, 1997). Horan and Brown (1997) tested carbon-limited microbial consortia and found that adding MTBE increased O_2 consumption, but greater concentrations (approaching 740 mg/L) may adversely affect the overall biodegradation of hydrocarbon constituents of liquid fuels.

A research group at the University of Notre Dame (Mo et al., 1995, 1996) isolated fifteen pure bacterial strains from biotreater sludge and other sources with the capacity to degrade MTBE when it was the sole carbon source. These strains degraded up to 40% of 200 ppm of MTBE in 1-2 weeks of incubation at 22-25°C. They also developed a mixed culture in bioreactors using MTBE as sole carbon source for over one year. The mixed culture degraded 160 ppm of MTBE after three days incubation in batch experiments and showed greater capability for degradation of MTBE than pure cultures.

Most studies under anaerobic conditions have not shown any substantial support for the degradation of MTBE. The laboratory results of Suflita and Mormile (1993) showed no evidence of MTBE degradation after 182 days of methanogenic conditions. Having studied the degradability of a number of fuel additives, however, they suggested that the chemical structure of these compounds greatly affect their susceptibility to biological decay. Compounds that contain a tertiary or quaternary carbon atom, like MTBE, are far more recalcitrant than other unbranched or moderately branched chemicals. Another study by Mormile et al. (1994) examined whether MTBE could be anaerobically degraded with various terminal electron acceptors. Their results showed no MTBE degradation after 244 days in a sulfate-reducing environment. However, under denitrifying conditions MTBE was degraded in one of three incubations. In this instance, MTBE was partially transformed to TBA after 152 days. While the single observation is supportive of potential biological decay, the overall results suggest that it occurred only rarely. In addition, they found TBA to also be resistant to anaerobic decay.

Yeh and Novak (1994) provided the most substantial evidence for anaerobic degradation of MTBE. Using soils of varying natural organic content, they evaluated the potential for MTBE biodegradation under denitrifying, sulfate reducing, and methanogenic conditions. While there was no loss of MTBE after 250 days in the organically rich soils, degradation was observed for microcosms made with organically poor soil under methanogenic conditions. However, degradation was evident only when nutrient amendments were added. They suggest that an organically rich environment such as fuel-contaminated soil is not likely to be conducive to MTBE degradation. Based on their results, they believe that MTBE degradation, if it is to occur at all, is highly dependent on the site conditions and a long acclimation period. They also hypothesized that the first and rate-limiting step in MTBE degradation may be cleavage of the ether bond. As was seen in the study of Mormile et al. (1994), this could account for the presence of TBA as a transformation product in the degradation of MTBE. Actually, an accumulation of TBA suggests that its degradation is more rate-limiting.

Laboratory microcosm studies conducted under aerobic and denitrifying conditions and field-scale reports have shown similar patterns of biodegradation of BTEX and MTBE. That is, biodegradation rates were higher near the contaminant source and lower further downgradient (Daniel and Borden, 1997).

A field experiment by Barker et al. (1990) investigated the influence of MTBE on the transport and degradation of monoaromatic hydrocarbons in groundwater. The test site at the Canadian Forces' Base in Borden, Ont. was used for previous natural gradient experiments, so that its hydrogeology was well understood. The results of the experiment showed that MTBE had no apparent effect on the rate of migration or decay for the BTEX compounds. While the BTEX compounds were readily degraded, MTBE exhibited no mass loss over the 16-month period of the study. The results of this field experiment did not support the notion suggested by Mihelcic (1990) that the presence of MTBE in contaminated groundwaters could potentially increase the movement of other gasoline compounds by cosolvency effects. Using sediment from the Borden test site, Hubbard et al. (1994) found MTBE to be recalcitrant in both aerobic and oxygen-limited microcosms over incubation periods of 8 to 15 months. As in the field studies, biotransformation of the monoaromatics appeared to be unaffected by the presence of MTBE.

A field study by LeBrun (1993) utilized a contaminant mass flux approach to estimate rates of intrinsic bioremediation for MTBE and BTEX at a gasoline-contaminated shallow aquifer in Sampson County, N.C. His results suggested that MTBE degradation was occurring near the source area at a rate of 0.13%/day. Since the contaminant plumes appear to have been degrading under a mixture of aerobic and denitrifying conditions, it is unclear which mechanism would have contributed to MTBE decay.

In the aqueous phase, reaction of MTBE with the hydroxyl radical can also be important in engineered treatment systems (Barreto et al., 1995). In surface waters, soils, and groundwaters, the only expected pathways for MTBE degradation are microbially mediated hydrolysis and oxidation (Cartwright and Smith, 1967). The major product of both biodegradation pathways is TBA. The major degradation pathways for MTBE and TBA are summarized in Figure 1 (Church et al., 1997).

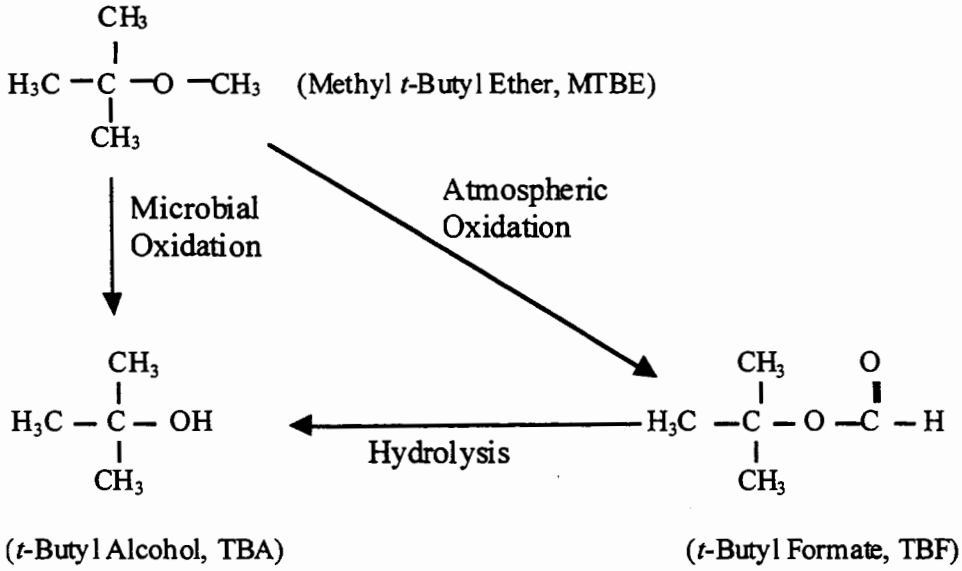

Figure 1. Summary of initial transformation pathways of MTBE. TBA is subject to further biodegradation to acetone, 2-propanol, formate, and ultimately CO_2.

Additional information on the biodegradation capabilities and fate and transport of this compound will become available as more data are accumulated through routine groundwater monit-

oring of leaking underground storage tank sites and sampling of drinking water systems.

Remediation of MTBE in Groundwater

Because MTBE has a low octane/water distribution coefficient and a high solubility, subsurface MTBE will occur predominantly in groundwater. The widespread occurrence of gasoline oxygenates in groundwater (Squillace et al., 1996) has led to a concern about their ultimate environmental fate and a search for remediation alternatives. Chemical characteristics of MTBE make its movement and remediation different from other gasoline components in several crucial ways. Because of its affinity for water and, consequently, its tendency to form large plumes, petroleum releases with MTBE can be more difficult and costly to remediate than petroleum releases that do not contain MTBE. Available cleanup technologies are costly.

In contrast with the preferred remediation techniques for petroleum hydrocarbons such as benzene (*e.g.,* bioremediation), pumping contaminated groundwater and treating it above ground (*i.e.* pump-and-treat) may be an effective remediation technology for MTBE because MTBE does not adsorb significantly to soil. As a result, fewer aquifer volumes are required to remove all of the MTBE than are required to remove slowly desorbing petroleum hydrocarbons. In addition, because it is highly soluble, most of the MTBE mass may quickly dissolve into groundwater, making pumping an efficient method for removing large quantities of the contaminant.

As with petroleum hydrocarbons, however, diffusion is also a factor controlling the remediation timeframe. If micropores exist within the aquifer that are not readily influenced by groundwater flow, transfer of a contaminant from the micropores to macropores will occur through the slow process of diffusion. Moreover, water treatment can be difficult, as the moderately low volatility of MTBE requires large air to water ratios for aerating water. Hence, in spite of some favorable characteristics, pump-and-treat may not always be an efficient remediation method for MTBE contamination. Aquifers with high total porosity but with low effective porosity remain troublesome in treating any contaminant.

Because of the poor stripping efficiency and low affinity of MTBE for activated carbon, MTBE is not a good candidate for using granular-activated carbon (GAC) to remove it from contaminated groundwater. For MTBE, GAC is about 1/3 to 1/8 as effective as in removing benzene. In addition, because MTBE "prefers" to remain in water, air strippers must use a higher volume of air than is required for benzene. GAC is often expected to be expensive and only moderately effective. Heating the water increases MTBE's Henry's Law constant and improves aeration performance, but heating costs can be substantial. A heated air stripper system was designed and implemented at a gasoline station site in Massachusetts. MTBE influent levels were reduced from 50 ppb to 12 ppb when using ambient air. Using exhaust gas from the offgas catalytic oxidation unit to increase the groundwater temperature 21-24^{0}F, MTBE removal efficiency from recovered groundwater increased from 76% to 92% (Bass and Sylvia, 1992). Air stripping and liquid-phase activated carbon adsorption systems are two of the most commonly implemented water treatment technologies for removing dissolved gasoline components from groundwater.

In situ biodegradation may be an effective remediation alternative (Borden et al., 1997; Daniel, 1995; Daniel and Borden, 1997; Dvorak, 1993; Horan and Brown, 1995; and Park and Cowan, 1997), but *in situ* degradation of MTBE in aquifers has not been well studied. More

information is required to determine the specific environmental conditions that enable significant rates of biodegradation to occur (Daniel & Borden, 1997).

Phytoremediation

Phytoremediation is an emerging technology that uses plants and their associated rhizospheric microorganisms to remove, degrade, or contain chemical contaminants located in the soil, sediments, groundwater, surface water, and even the atmosphere. Plant-based remediation systems can function with minimal maintenance once they are established.

In previous work in our laboratory, we have examined the feasibility of phytoremediation on MTBE in groundwater. The experimental system we used was described in detail in Zhang et al. (1998). According to our experimental results, the presence of plants enhanced the rate of evapotranspiration and reduced the time required to remove MTBE from the system.

Our ongoing research is using the same system except bacteria capable of degrading MTBE were introduced into four of the six channels; that is bacteria #33 in channels 1 and 2 and bacteria #41 in channels 5 and 6. The bacterial numbers refer to Mo et al. (1997). An MTBE solution of 0.844 M was fed for more than 80 days before being switched back to distilled water. Groundwater effluent concentration and gas fluxes are being monitored from the introduction of MTBE onward. The effect of the bacteria on biodegradation is being monitored by using the total mass balance.

Summary

While many of the studies indicate aerobic decay of MTBE, little evidence of MTBE degradation under anaerobic conditions is found. *In situ* biodegradation may be an effective remediation alternative for contamination with MTBE.

Using an experimental channel system, we studied the fate and transport of MTBE in groundwater under vegetative conditions, and found that vegetation helped to bring MTBE up from the groundwater into the atmosphere.

A further study is in progress with strains capable of degrading MTBE introduced into the vegetated channel system.

Acknowledgments

This research was partially supported by the U.S. EPA under assistance agreements R-819653 to the Great Plains-Rocky Mountain Hazardous Substance Research Center for Regions 7 and 8 under project 94-27. It has not been submitted to the EPA for peer review and, therefore, may not necessarily reflect views of the agency and no official endorsement should be inferred. The Center for Hazardous Substance Research also provided partial funding.

References

American Petroleum Institute, 1994a. Odor threshold studies performed with gasoline and gaso-

line combined with MTBE, ETBE and TAME, API Publication **4592.**

American Petroleum Institute, 1994b. Transport and fate of dissolved methanol, methyl-tertiary-butyl-ether, and monoaromatic hydrocarbons in a shallow sand aquifer, *API Publication* **4601**.

Angel, C.R., 1991. If the tap water smells foul, think MTBE. *J. Am. Med. Assoc.,* **266**, 2985-2986.

Ballard, T. and T. Landwehr, 1998. MTBE-The benzene of the 90's? http://www.apexenvirotech.com/MTBE.html.

Barker, J.F., C.E. Hubbard, and L.A. Lemon, 1990. The influence of methanol and MTBE on the fate and persistence of monoaromatic hydrocarbons in groundwater. In: *1990 NWWA/API Conference on Petroleum Hydrocarbons and Organic Chemicals in Groundwater-Prevention, Detection and Restoration.* National Water Well Association, Dublin, Ohio. pp. 113-127.

Barreto, R.D., K.A. Gray, and K. Anders, 1995. Photocatalytic degradation of methyl-tert-butyl ether in TiO_2 slurries: a proposed reaction scheme. *Water Res.*, **29**, 1243-1248.

Bass, D.H. and T.E. Sylvia, 1992. Heated air stripping for the removal of mtbe from recovered groundwater. In Stanley, A. (ed.), *NWWA/API Petroleum Hydrocarbons & Organic Chemicals in Ground Water: Prevention, Detection, and Restoration Conference, Eastern Regional Ground Water Issues*. Houston, Tex., Nov. 4-6, 1992, [Proceedings]: National Water Well Association and American Petroleum Institute, pp. 483-492.

Borden, R.C., R.A. Daniel, L.E. LeBrun, IV, and C. W. Davis 1997. Intrinsic biodegradation of MTBE and BTEX in a gasoline-contaminated aquifer. *Water Resources Res.*, **33**, 1105-1115.

Budavari, S., M. J. O'Neil, A. Smith, and P.E. Heckelman (Eds.), 1989. The Merck Index, 11th ed., Merck & Co., Inc. Rahway, N.J., p. 951.

Church, C.D., L.M. Isabelle, J.F. Pankow, D.L. Rose and P.G. Tratnyek, 1997. Method for determination of methyl tert-butyl ether and its degradation products in water. *Environ. Sci. Technol.*, **31**, 3723-3726.

Daniel, R.A., 1995. Intrinsic biremediation of BTEX and MTBE—Field, laboratory and computer modeling studies. M.S. Thesis, North Carolina State University, Raleigh, N.C.

Daniel, R.A. and R.C. Borden, 1997. Spatial variability in intrinsic bioremediation rates: Effect on contaminant transport. in *In Situ and On-Site Bioremediation*, Alleman, B.C. and A. Leeson, (Eds.), Battelle Press, Columbus, Ohio; **1**, p. 29.

Damera, R., M.R. Hill and D. Murali, 1997. Rapid clean-up of a multiple fuel spill. In *In Situ and On-Site Bioremediation*, Alleman, B.C. and A. Leeson, ed., Battelle Press, Columbus, Ohio. **1**, p. 199.

Duffy, J.S., J.A. Del Pup and J.J. Kneiss, 1992. Toxicological evaluation of methyl tertiary-butyl ether (MTBE): Testing performed under TSCA consent agreement. *J. Soil Contam.*, **1**, 29-37.

Dvorak, B.I., D.F. Lawler, G.E. Speitel, Jr., D.L. Jones and D.A. Broadway, 1993. Selecting among physical/chemical processes for removing synthetic organics from water. *Water Environ. Res.*, **65**, 827-838.

EPA, 1997. MTBE: State perspectives. Office of Underground Storage Tanks. http:/www.epa.gov/swerust/mtbe/briefs/ellis/index.htm.

EPA 510-F-97-015, 1998. Remediation of MTBE contaminated soil and groundwater. MTBE Fact Sheet #2. Jan. 1998, pp. 1-5.

Garrett, P., M. Moreau, and J.D. Lowry, 1986. MTBE as a ground water contaminant. In: *1986*

NWWA/API Conference on Petroleum Hydrocarbons and Organic Chemicals in Groundwater-Prevention, Detection and Restoration. National Water Well Association, Dublin, OH. pp. 227-238.

Horan, C.M., and E.J. Brown, 1995. Biodegradation and inhibitory effects of methyl-tertiary-butyl ether (MTBE) added to microbial consortia. In *Proceedings of the 10th Annual Conference on Hazardous Waste Research,* Kansas State University, Manhattan, Kan., May 23-24, 1995, pp. 11-19.

Hubbard, C.E., J.F. Barker, and S.F. O'Hannesin, 1994. Transport and fate of dissolved methanol, methyl-tertiary-butyl-ether, and monoaromatic hydrocarbons in a shallow sand aquifer. American Petroleum Institute, Washington, D.C., API Publication **4601**.

LeBrun, L.E., 1993. Field measurement of intrinsic bioremediation rates using mass balance techniques. M.S. Thesis, North Carolina State University, Raleigh, N.C.

Lee, M.D., 1986. Biodegradation of organic contaminant in the subsurface of hazardous waste sites. Ph.D. Dissertation, Rice University, Houston, Tex.

Mihelcic, J.R., 1990. Modeling the potential effect of additives on enhancing the solubility of aromatic solutes contained in gasoline. *Ground Water Monitor. Rev.*, **10**, 132-137.

McKinnon, R.J., and J.E. Dyksen, 1984. Removing organics from groundwater through aeration plus GAC. *J. Am. Water Works Assoc.*, **76**, 42-47.

Mo, K., C.O. Lora, A.E. Wanken, and M. Javanmardian, 1997. Biodegradation of methyl t-butyl ether by pure bacterial cultures. Appl. Microbiol. Biotechnol. **47**, 68-72.

Mo, K., C. Lora, A. Wanken and C.F. Kulpa, 1995. Biodegradation of methyl-t-butyl ether by pure bacterial cultures. American Society for Microbiology Annual Meeting, 1995, Washington, D.C.: http:/www.nd.edu/~cbpc/kulpa3.html.

Mo, K. C. Lora, M. Javanmardian, X. Yang, and C.F. Julpa, 1996. Biodegradation of gasoline oxygenate, methyl-t-butyl by mixed and pure cultures. American Society for Microbiology Annual Meeting, 1996, New Orleans, La.: http:/www.nd.edu/~cbpc/kulpa3.html.

Mormile, M.R., S.H. Liu and J.M. Sulfita, 1994. Anaerobic biodegradation of gasoline oxygenates: Extrapolations of information to multiple sites and redox conditions. *Environ. Sci. Technol.*, **28**, 1727-1732.

Newman, A., 1995. MTBE detected in survey of urban groundwater. *Environ. Sci. Technol.*, **29**, 305A.

Oil & Gas Journal, 1995. USGS reports MTBE in groundwater. **93** (16), p21-22.

Park, K. and R. M. Cowan, 1997. Biodegradation of gasoline oxygenates. In *In Situ and On-Site Bioremediation*, Alleman, B.C. and A. Leeson, (Eds.), Battelle Press, Columbus, Ohio; **1**, p. 17.

Robbins, G.A., S. Wang and J.D. Stuart, 1993. Using the static headspace method to determine Henry's law constants. *Anal. Chem.*, **65**, 3113-3118.

Salanitro, J.P., L.A. Diaz, M.P. Williams, and H.W. Wisniewski, 1994. Isolation of a bacterial culture that degrades methyl-t-butyl ether. *Appl. Environ. Microbiol.*, **60**, 2593-2596.

Squillace, P.J., J.S. Zogorski, W.G. Wilber, and C.V. Price, 1996. Preliminary assessment of the occurrence and possible sources of MTBE in groundwater in the United States, 1993-1994. *Environ. Sci. Technol.*, **30**, 1721-1730.

Squillace, P.J., J.F. Pankow, N.E. Korte, and J.S. Zogorski, 1997. Review of the environmental behavior and fate of methyl-tert-butyl ether. *Environ. Toxic. Chem.*, **16**, 1836-1844.

Steffan, R. J., K. McClay, S. Vainberg, C. W. Condee, and D. Zhang, 1997. Biodegradation of the gasoline oxygenates methyl tert-butyl ether, ethyl tert-butyl ether, and tert-amyl methyl

ether by propane-oxidizing bacteria, *Appl. Environ. Microbiol.*, **63**, 4216-4222.

Suflita, J.M. and M.R. Mormile, 1993. Anaerobic biodegradation of known and potential gasoline oxygenates in the terrestrial subsurface, *Environ. Sci. Technol.*, **23**, 976-978.

Taylor, J.R., and T.J. O'Brien, 1993. Evaluating residential water supply wells in a fractured bedrock aquifer contaminated with MTBE—A case study. *Ground Water Management*, **16**, 929-937.

Worthington, M.A., and E.J. Perez, 1993. Dating gasoline releases using ground-water chemical analyses—Case studies. *Ground Water Management*, **17**, 203-217.

Yeh, C.K., and J.T. Novak, 1994. Anaerobic biodegradation of gasoline oxygenates in soils. *Water Environ. Res.*, **66**, 744-752.

Zhang, Q., L. C. Davis, and L. E. Erickson, 1998. Using vegetation to treat methyl-tert-butyl ether contaminated groundwater. *Proceedings of the 13th Annual Conference on Hazardous Waste Research*, (in press), Snowbird, Utah.

Function and Degradation of Benzotriazole

Doug Lupher[1], L.C. Davis[2], and L.E. Erickson[1], Departments of [1]Chemical Engineering and [2]Biochemistry, Kansas State University, Manhattan, KS 66506

Abstract

Benzotriazole and its derivatives are used in anticorrosion applications, UV stabilizers, and photography applications. Small concentrations are present in antifreeze and airplane deicer solutions. Because of this, there is a good chance that benzotriazole contaminants will leak into the environment. Benzotriazole binds weakly to most soils. Therefore, contamination of groundwater, lakes, and streams is a potential risk. The effects of benzotriazole on animals and humans have been little studied. Benzotriazole will kill plants, however, even at concentrations of 1 mM. There has been no known pathway for degradation of benzotriazole in the environment. Various methods for degradation were studied. One method was the use of *Phanerochaete chrysosporium*, also known as white rot fungus. It has a nonspecific mechanism that uses peroxidase known to degrade lignin and various other contaminants. Various concentrations of benzotriazole and methylbenzotriazole were added to fungi in a culture medium. After only a few days, some degradation was evident. After 12-17 days, levels were down by over one-half for most experiments. Methylbenzotriazole was degraded more by the fungus than benzotriazole. Small concentrations of benzotriazole and methylbenzotriazole were added to horseradish plants to see if degradation would occur. Horseradish contains a peroxidase like that of white rot fungus. In 26-27 days, levels were down by approximately 55-90%. It is not certain whether the plant is simply taking up the contaminant or if actual degradation is occurring. However, the horseradish tolerated levels that killed other plants such as sorghum, pumpkins, and milfoil.

Introduction

The benzotriazole structure is a benzene ring fused to a three-nitrogen triazole group. Information on benzotriazole is derived from a 1977 EPA report unless otherwise noted (Davis et al., 1977). Benzotriazole and its derivatives are white powders with melting points in the area of 100-150°C. They are photostable compounds and do not break down when exposed to electromagnetic radiation. Benzotriazoles have three major applications. The most prominent is for use in antifreeze, airplane deicers, and industrial processes to prevent metal corrosion. The concentration of benzotriazole or methylbenzotriazole (also known as tolyltriazole) in antifreeze is 0.01-2%. The concentration in deicers varies between manufacturers and is uncertain; in some products, it could be up to 10%. The second major use is to stabilize materials against decomposition by UV rays. Benzotrizole derivatives are added to plastics and paints since they are stable when exposed to light. The third and by far the smallest major use of benzotriazole is as an antifoggant in photography film. The N-alkyl benzotriazoles are used in many organic synthetic reactions, but the scale of use is not public information. Examples are provided in Chemical Abstracts.

Effects of benzotriazole on plant and animal systems have been little studied. Concentrations lower than 1 mM (119 mg/L) will kill plants over time (Wu et al., 1998). Animal studies have proven that breathing benzotriazole dust may damage the lungs. Some derivatives also affect bacterial cell growth and can cause mutations (Davis et al., 1977).

There are still many questions about what happens to benzotriazole in the environment. No natural pathway for degradation has been reported. Benzotriazole binds to most soils weakly. Its log K_{oc} is about 1.3, so it has relatively low affinity for organic matter. Because of this, the potential for benzotriazole seeping into groundwater, lakes, and streams is great. It has been estimated that ~1000 gallons of airplane deicer is needed for one large passenger jet. Huge amounts of benzotriazole, therefore, could be entering the environment via runoff from airfields. Various pathways for degradation need to be considered to remove this possibly harmful contaminant.

Phanerochaete chrysosporium, commonly called white-rot fungus, degrades lignin and various contaminants (Barr and Aust, 1994). The fungus produces peroxidase enzymes when supplied with low levels of carbon, nitrogen, or sulfur nutrients. These enzymes react with hydrogen peroxide, which is also produced to oxidize the contaminant via a free radical reaction. Many of the oxidized forms of the contaminants can be further degraded to carbon dioxide.

Experiments with White-Rot Fungus

An experiment was set up to see if the white-rot fungus growing on wood would degrade benzotriazole and methylbenzotriazole. Wood splints (1x6x115 mm) were washed and dried to leach out organic matter that might possibly interfere with measurements. Then 10 g of splints were placed in a Pace brand salsa jar, and 20 mL of culture medium was added. The culture medium contained the following per L: 2 g KH_2PO_4, 0.14 g $CaCl_2{\cdot}2H_2O$, 0.7 g $MgSO_4{\cdot}7H_2O$, 0.07 g $FeSO_4{\cdot}7H_2O$, 0.035 g $MnSO_4{\cdot}H_2O$, 0.046 g $ZnSO_4{\cdot}7H_2O$, 0.07 g $CuSO_4{\cdot}5H_2O$, 1.84 g diammonium tartrate, 1 g yeast extract, 2.5 mg thiamine, 2.3 g disodium tartrate, 67.3 mg veratryl alchohol, and 10 g glycerol. This culture medium supported fungus growth in previous experiments (Capdevila et al., 1990). Four bottles were set up this way. Two bottles received 2 mL of 2 mg/mL benzotriazole while the other two received 2 mL of 2 mg/mL methylbenzotriazole. The jars were labeled B1 tall wood, B2 tall wood, M1 tall wood, and M2 tall wood. All of the jars had an initial concentration of 0.18 mg/mL of contaminant.

Four 60 mL screw-top test tubes were used to set up a similar experiment. Five g of half-length washed and dried splints along with 10 mL culture medium were placed in each test tube. Two tubes received 1 mL of 2 mg/mL benzotriazole while the other two tubes received 1 mL of 2 mg/mL methylbenzotriazole. All were innoculated with a 0.5 mL suspension of white-rot fungus. The lids were loosely screwed on to each container. The jars were labeled B1 short wood, B2 short wood, M1 short wood, and M2 short wood. Each tube had a contaminant concentration of 0.17 mg/mL. All eight containers were set into a 39°C water bath and covered.

Samples were taken from each jar and analyzed after 3, 6, 12, and 20 days with 700 µL samples pipetted from each container. Samples were then centrifuged for 2.5 min and injected into a high performance liquid chromatograph (HPLC). Peak heights displayed on the HPLC recorder are representative of concentration. These peak heights were compared with 0.1 mg/mL standards of benzotriazole and methylbenzotriazole to determine concentration. The mobile phase used for the HPLC was 70% MeOH, 30% water. This mixture gives good resolution while lowering retention times. Results are summarized in Figure 1.

After three days, the first samples were analyzed using HPLC. Fungus had grown all over the splints by this time. B1 and B2 tall wood concentrations were down roughly 10%, while M1 and

M2 tall wood concentrations were down 20-30%. All of the concentrations in short wood samples were down 50-75%. This was probably a result of adsorption to the wood. More solution is in direct contact with the wood in the test tubes and, therefore, more contaminant is quickly adsorbed to the wood. Adsorption ratios for benzotriazole to wood were roughly 50-67% in our previous experiments at comparable concentrations. It is assumed that wood adsorption occurs within 24 h of experiment set-up for the short splints, with no more wood adsorption occurring after this point. An initial fast-eluting HPLC peak resulting from organic matter from the wood and veratryl alcohol from the medium were present in all samples.

All samples were assayed after six days as before. The concentrations in tall wood samples were down 15-20% from previous assay. The short samples were relatively the same. The initial peak had tripled for most samples. This is either the result of soluble aromatics from the wood or more likely a product of degradation, because the wood had been previously washed.

After twelve days, concentrations in the tall wood samples were down 60-70% from the previous assay. Concentrations in B1 and B2 short wood were down 85% while those in M1 and M2 short wood were down 60% from the six-day assay. The fast-eluting peaks for almost all the samples were roughly three times those of the previous assay.

After twenty days of growth, B1, B2, and M1 tall wood samples were run through HPLC as before. The initial peak was almost the same as in previous assays. However, the peak was so large that only shoulders appeared for benzotriazole and methylbenzotriazole. Therefore, no quantitative data could be recorded. Concentrations, however, were estimated to be significantly lower than those measured after twelve days.

Experiments with Horseradish Plants

Another method attempted to degrade benzotriazole and methylbenzotriazole was the use of horseradish plants. It is well known that horseradish root contains peroxidase enzymes. An experiment was set up to measure possible contaminant degradation by horseradish.

Seventy grams of vermiculite were added to each of four 1-L plastic containers. Four hundred mL of liquid was added to each. The liquid contained 250 mL Hoagland's nutrient solution and various amounts of water and benzotriazole stock solution to give total concentrations of 0.05, 0.075, 0.1, and 0.125 mg/mL in a total of 400 mL. The 400 mL of liquid was enough to saturate the vermiculite and leave enough runoff to take samples. One horseradish plant was placed in each container. Each container was weighed. The plants in each container had an average fresh weight of 38 g. The plants were placed under light and watered with distilled water periodically. The plants were weighed each time samples were run to estimate water amount. The difference in weight from the starting value represented the change in amount of water, assuming the weight of the plants is relatively constant. This mass of water was taken into account in the calculations.

A similar experiment was set up one day later using methylbenzotriazole. Everything was the same as before except concentrations of methylbenzotriazole were 0, 0.025, 0.05, 0.075, and 0.1 mg/mL. Four small horseradish plants with an average total fresh weight of 20 g were also planted in each container instead of just one plant.

Samples were taken on day seven for benzotriazole and day six for methylbenzotriazole. A 1-mL liquid sample was pipetted out of each container. This solution was centrifuged and 25 μL of the liquid was injected into the HPLC. The settings were the same as for the fungal system. The concentrations had decreased by 20-40%, approximately one-fourth, as shown in Figure 2.

On day 27 for benzotriazole and day 26 for methylbenzotrizole, samples were again taken. Concentrations for both benzotriazole and methylbenzotriazole were down significantly, approximately 60-80% from previous assay. Two early peaks appeared as before on the HPLC. These could be oxidized forms of the contaminants.

The horseradish plants were given a second dose of contaminant plus additional water and vermiculite at 29 days for benzotriazole and 26 days for methylbenzotriazole. These compounds nearly disappeared from the aqueous phase within nine weeks for plants exposed to all but the highest levels. Plants dosed with the highest concentrations showed root damage and eventually died, having been somewhat stunted in development from the first dose.

Nearly all the plants survived the experiment while contaminant concentrations were significantly down from starting values. There are a few possible explanations. First, the horseradish may be degrading the benzotriazole and methylbenzotriazole at the root surface. Another possibility is that adsorption to and in roots may be occurring, but it is unlikely to be greater than for wood (~50%). Previous experiments showed that adsorption to vermiculite is only 1% of input. A likely possibility is that the horseradish could be drawing the contaminant up into the leaves of the plant along with transpiration water. To test this, some leaves were clipped off and mixed with methanol to extract the contaminant. When the mixture was run through the HPLC, the organic matter in the plants made such an enormous peak that possible benzotriazole and methylbenzotriazole peaks were overshadowed.

We can set a limit on the benzotriazole level that may be present in leaves in an extractable form. If all of the benzotriazole in 800 mL water with 0.1 mg/mL is moved to leaves of ~2 g weight which are extracted with 20 mL MeOH, the potential concentration is ~4 mg/mL in the extract. Even with the high fast-moving peak we could easily observe 1/40 this level. Thus it appears that more than 95% of freely extractable benzotriazole is gone.

Conclusion

From these two experiments, it appears that white-rot fungus and horseradish plants are able to partially degrade benzotriazole and methylbenzotriazole over time.

References

Barr, D.P. and S.D. Aust, Mechanism white rot fungi use to degrade pollutants, Environ. Sci. Technol., **28:**79A-86A. 1994.

Capdevila, C., S. Moukha, M. Ghyczy, J. Theilleux, B. Gelie, M. Delattre, G. Corrieu, and M. Asther, Characterization of peroxidase secretion and subcellular organization of *Phanerochaete chrysosporium* INA-12 in the presence of various soybean phospholipid fractions, Appl. Environ. Microbiol. **56:**3811-3816. 1990.

Davis, L.N., J. Santodonato, P.H. Howard, and J. Saxena, Investigation of Selected Potential Environmental Contaminants: Benzotriazoles, Environmental Protection Agency, Washington.

1977.

Wu, X., N. Chou, D. Lupher, and L.C. Davis, Benzotriazoles: Toxicity and Biodegradation, Proceedings of the Conference on Hazardous Waste Research, Snowbird, Utah, in press, 1998.

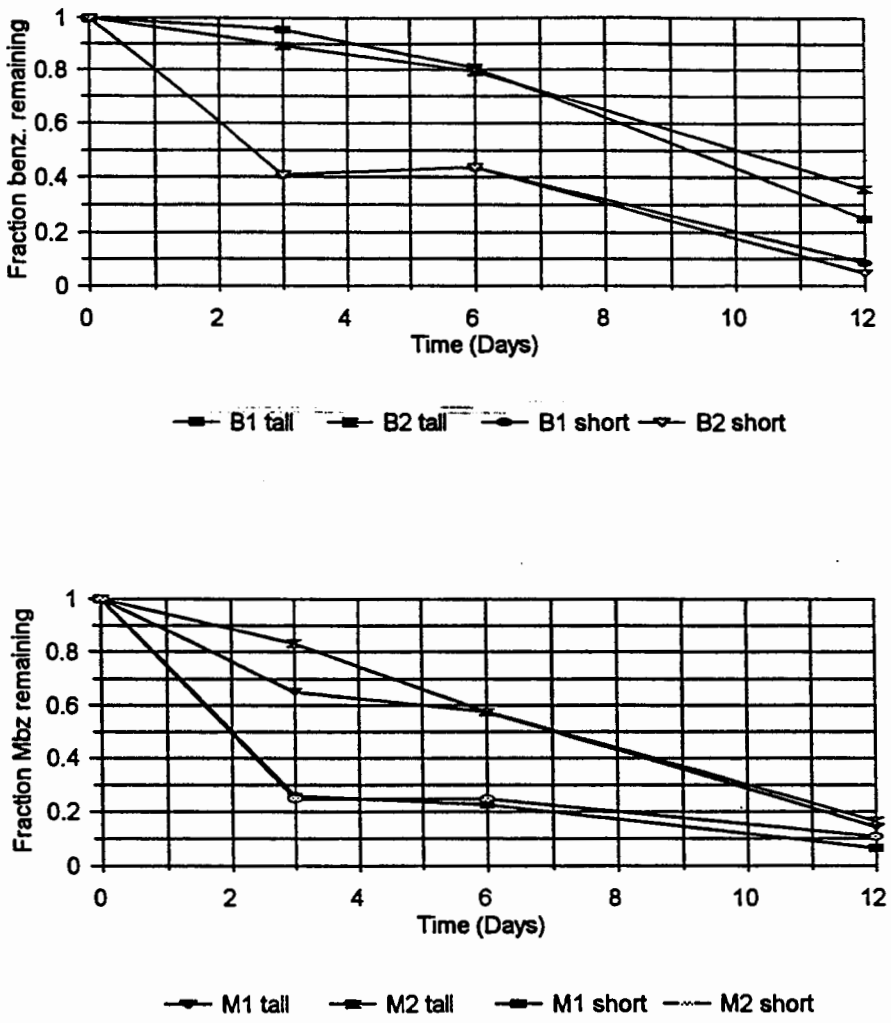

Figure 1. Dimensionless concentration of benzotriazole (top) and methylbenzotriazole (bottom) in aqueous phase vs. time for experiments with *Phanerochaete chrysosporium*.

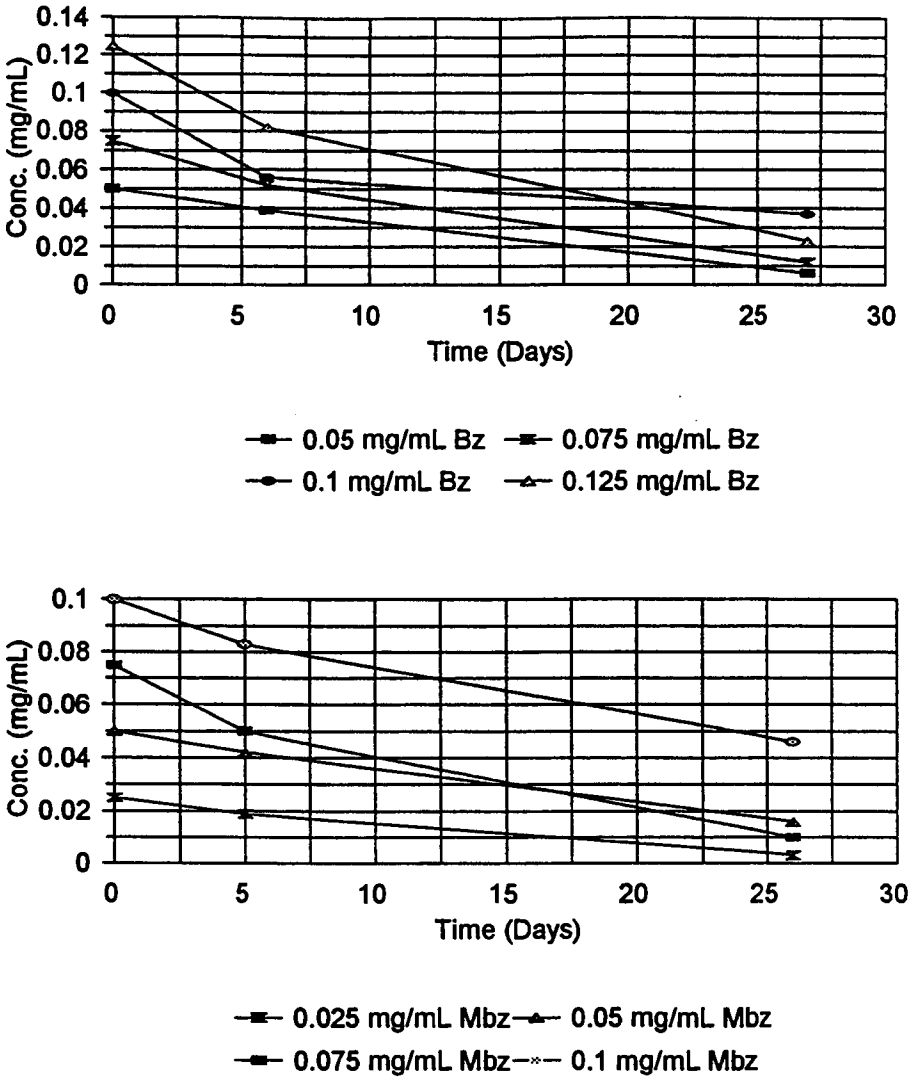

Figure 2. Variation of benzotriazole (top) and methylbenzotriazole (bottom) concentrations with time in aqueous phase of root environment of horseradish plants.

Apoptosis and Bcl-2 Expression in Hybridoma Cell Cultures

Mark C. Mowry[1], Marit Nilsen-Hamilton[2], and Carole A. Heath[1]
Departments of [1]Chemical Engineering and [2]Biochemistry, Biophysics, and Molecular Biology,
Iowa State University, Ames, IA 50011

ABSTRACT

Apoptosis or programmed cell death is a type of cell death in which the cell actively participates. Apoptosis can be a significant cause of cell death to hybridoma cells during all phases of cell growth, and can limit the viable cell density and the duration of batch culture. In a batch culture of H166 hybridoma cells, approximately 80% of the cells died as the result of apoptosis, which is similar to the results of previous investigators (Singh et al., 1994). The proto-oncogene bcl-2 has an inhibitory effect on apoptosis in many cell lines including hybridomas. Bcl-2 expression increases the viable cell density and antibody productivity of hybridomas grown in batch culture (Itoh et al., 1995). In addition to batch culture, hybridomas can be grown in both CSTR and perfusion cultures. Hybridoma cells were grown in perfusion culture at high cell retention in order to cause the build-up of dead cells, which limits the steady-state viable cell densities that can be achieved in perfusion culture. A close correlation between apoptotic and nonviable cells showed that apoptosis was the primary mode of cell death during perfusion culture.

In order to investigate the effect of bcl-2 on hybridoma cell death in perfusion culture, a hybridoma cell line was transfected with various plasmids from the Clontech Tet-off gene expression system. This system allows for the control of bcl-2 expression through a tetracycline response element. Bcl-2 is fully expressed in the absence of tetracycline, and is reduced or completely turned off as tetracycline is added. This allows for bcl-2 production to be controlled for a single cell line during batch or continuous culture. Throughout the culture, bcl-2 production will be monitored by a quantitative western blotting technique. Hybridoma cells will be grown in both batch and perfusion cultures at various concentrations of tetracycline in order to determine the effect of bcl-2 on cell density, antibody productivity and apoptosis.

INTRODUCTION

Monoclonal antibodies are widely used as therapeutic and diagnostic agents. They allow the detection and quantification of many biological compounds such as proteins, carbohydrates and nucleic acids. B cell hybridomas, which are created by the fusion of an antibody-producing spleen cell and a myeloma cell, are capable of producing monoclonal antibodies against almost any existing antigen (Kohler and Milstein, 1975). Once hybridomas producing a specific antibody have been cultured, it is necessary to scale up production to obtain high antibody yields.

There are various methods of culturing hybridomas on an industrial scale, including batch, CSTR and perfusion culture. Batch reactors are commonly used since they are easy to operate, but provide low antibody yields and cannot be operated continuously. CSTR reactors operate continuously, but do not achieve the high cell densities and productivities that can be obtained in perfusion culture. In perfusion culture, cells are maintained in a low growth state by entrapping the cells in a reactor chamber and removing spent growth medium through a membrane system. A cell bleed must be removed from a perfusion reactor in order to prevent the build-up of dead

cells. As the cell bleed rate in these reactors is decreased, there is an increase in viable cell density but a decrease in viability. This continues until the cell bleed rate is reduced to the point where dead cells begin to build up in the reactor, and both the viability and the viable cell density begin to drop rapidly. A perfusion system using internal microporous polypropylene fibers was able to obtain viable cell densities as high as 2×10^7 cells/ml (Banik and Heath, 1995).

The buildup of dead cells that occurs at low cell bleed rates may be the result of both apoptosis and necrosis. Apoptosis is genetically programmed cell death in which the cell actively participates, while necrosis is the result of a violent insult against the cell. Apoptosis is initially characterized by cell shrinkage and condensation of the nuclear chromatin (Figure 1). This is followed by extensive nuclear fragmentation and the breakup of the cells into apoptotic bodies. Apoptosis can be stimulated by numerous factors, including nutrient limitation, mechanical stress, viral infection, toxic buildup, and growth factor deprivation.

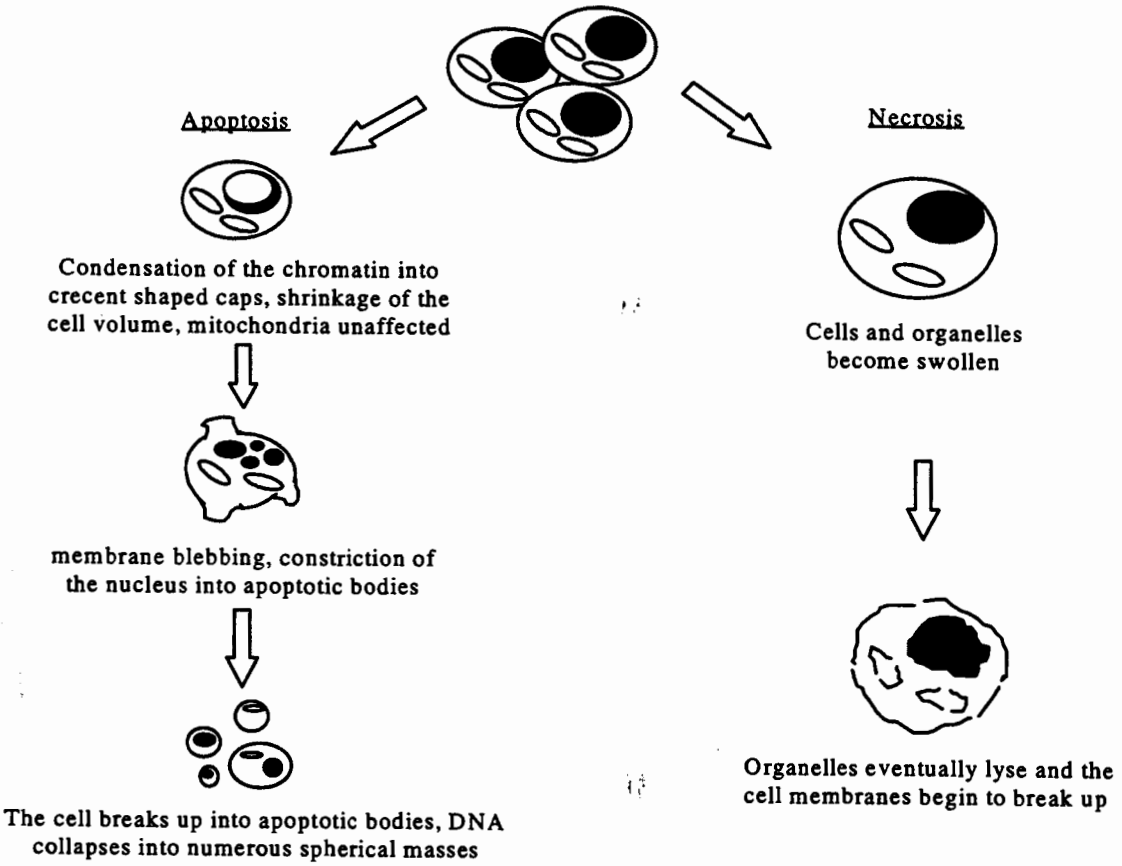

Figure 1. Comparison between morphological changes that occur in apoptosis and necrosis.

It has been determined that hybridoma cells grown in various culture conditions are susceptible to apoptosis (Franek et al., 1992; Singh et al., 1994; Al-Rubeai et al., 1995). De la Broise et al. (1991) observed that cells in perfusion culture at low cell bleed rates enter an arrested state and die quickly. It is now believed that this arrested state may lead to cell death by apoptosis. Even with substrate availability and without toxic concentrations of metabolites, hybridomas

continue to die in perfusion culture (Banik and Heath, 1995). In addition, hybridomas whose growth was inhibited by thymidine treatment quickly died as the result of apoptosis (Perreault and Lemieux, 1993; Simpson et al., 1997). It seems likely that cells in the low growth states normally found in perfusion culture may be susceptible to apoptosis. These results suggest that higher viable cell densities can be achieved at very low growth rates in perfusion culture by minimizing cell death from apoptosis.

The overexpression of the proto-oncogene bcl-2 can block apoptosis in many cell lines, including hybridomas (Itoh et al., 1995; Simpson et al., 1997). Itoh et al. (1995) found that the overexpression of bcl-2 increased the maximum viable cell density by 45%, delayed the start of apoptosis by 2 days, and prolonged the viable culture period by 4 days in batch culture. This suggests that it may be possible to increase the viable cell density of perfusion reactors by culturing hybridomas that overexpress bcl-2.

MATERIALS AND METHODS

A murine B cell hybridoma (H166) donated by Abbott Laboratories and producing an IgM antibody was used in this study. Cells taken from frozen stocks were grown in 75 cm^2 tissue culture flasks at 37°C in a humidified incubator with 5% CO_2. Cells were initially grown in Iscove's Modified Dulbeco's Medium (IMDM, Gibco BRL, Grand Island, NY), supplemented with 15% fetal bovine serum (FBS). These cells were slowly transferred to hybridoma serum-free media (HSFM, Gibco BRL), which contains a very low level of protein, as insulin and transferrin. Culture medium was adjusted to pH 7.2 with sodium bicarbonate and supplemented with 10^5 units/l penicillin-streptomycin.

The H166 hybridomas were grown batchwise in 250-ml spinner flasks to determine the susceptibility of this cell line to apoptosis. Cells were grown in the tissue culture flasks in batch mode for approximately ten passages and were then seeded in 250-ml spinner flasks at a cell density of 3×10^5 viable cells/ml. Cell density and viability were determined with a hemocytometer after staining with erythrosin B dye. The extent of apoptosis was determined by staining the cells with acridine orange and ethidium bromide. Stained cells were placed on a hemocytometer, and cell morphology was analyzed by fluorescence microscopy. Normal/live cells contain bright green chromatin with an organized structure, while early apoptotic cells have bright green, highly condensed chromatin. Late apoptotic cells contain bright orange, highly condensed chromatin, while necrotic cells have bright orange chromatin with a highly organized structure.

Cells were also grown in perfusion culture at high cell retention in order to determine whether cells grown in perfusion die primarily as the result of apoptosis or necrosis. The perfusion reactors consist of jacketed glass vessels with working volumes of 650 ml. The temperature was maintained to 37°C by pumping water through the heating jackets. The dissolved oxygen concentration was maintained at 40-50% of saturation by varying the air to oxygen ratio flowing into the reactor through a microporous sparger. Reactors were well mixed with a magnetic stirrer at 70-80 rpm. The reactor pH was controlled between 7.0 and 7.1 by supplying 5% CO_2 along with the air, and by adding 0.5 M $NaHCO_3$ as needed. The pH and dissolved oxygen were both monitored by an Applikon control system.

The reactors were inoculated with 3.3×10^5 cells/ml from an exponentially growing batch

culture (250-ml spinner flasks). They were operated in batch mode until the density increased to more than 10^6 cells/ml, after which continuous operation was initiated. The liquid level was maintained at 650 ± 10 ml with a chemostat tube. During perfusion operation, medium was removed from the reactors in two ways. A permeate stream consisting of a cell-free bleed was removed through a hollow membrane cartridge (A/G Technology Corporation, Needham, MA), while a second stream was removed directly from the reactor, determining the cell bleed rate. Masterflex peristaltic pumps (Cole-Parmer, Vernon Hills, IL) were used for media feed and removal, as well as for recirculation through an external loop. Figure 2 shows a diagram of the setup of the perfusion reactor used in this study.

For the perfusion experiments, an ApopTag Direct in situ apoptosis detection kit (Oncor, Gaithersburg, MD) was used to detect apoptosis by testing for DNA strand breaks. Residues of a fluorescein nucleotide were added to the 3'-OH ends of DNA strand breaks by the action of terminal deoxynucleotidyl transferase (TdT). Apoptotic cells, which are known to break down into 180 bp fragments (Wyllie, 1980), have many more DNA strand breaks than non-apoptotic cells. Cells were counter stained with 5 μg/ml propidium iodide, which is used to determine total DNA content. The percentage of apoptotic cells was determined by flow cytometry (EPICS 752, Coulter Corp.) at the Iowa State University Cell and Hybridoma Facility. A sample incubated in camptothecin for 4 h was used a positive control for apoptosis.

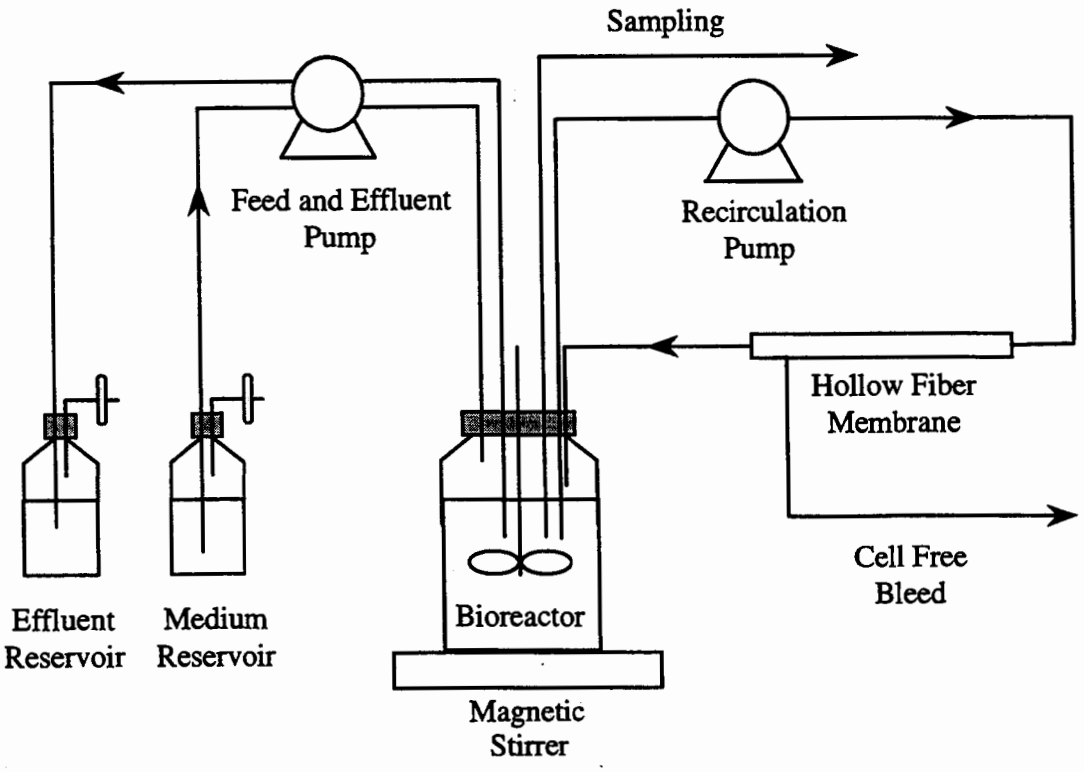

Figure 2. Diagram of the perfusion reactor used in these experiments. The system also has dissolved oxygen control, by aeration through a microporous sparger, and pH control, by the addition of 0.5 M $NaHCO_3$.

After batch and perfusion experiments were performed, the H166 hybridoma cells were transfected with various plasmids in order to obtain inducible expression of bcl-2. The cells were seeded in HSFM with 15% FBS at a viable cell density of 2-3 x 10^5. The cells were allowed to grow in a humidified incubator at 37°C with 5% CO_2 until the viable cell density reached 1x 10^6, with a 90% viability. Cells were resuspended at 1 x 10^7 viable cells/ml in HSFM with 30-50 µg/ml total plasmid. For the co-transfection with PTRE-bcl2 (or pTRE) and pTK-Hyg, the concentration of pTK-Hyg was 2 µg/ml, while the concentration of pTRE-bcl2 (or pTRE) was 40 µg/ml. Electroporation cuvettes (BTX-2mm gap) were filled with 400 µl of the cell suspension and stored on ice for 10 min. The cells were then electroporated in a BTX 600 electrocell manipulator at a charging voltage of 200 V, a resistance of 129 Ω, and a capacitance of 1200 µF. Cells were then placed on ice for 10 min, and were then resuspended in 1.2 ml HSFM with 15% FBS in a 12-well culture plate. After growing the cells for two days, the cells were transferred to media containing selection antibiotic in order to select for positive clones.

RESULTS AND DISCUSSION

Growth of hybridomas in batch culture

Previous investigators have determined that hybridoma cells are susceptible to apoptosis during normal culture conditions, and that apoptosis is significant during the decline phase of batch culture (Al-Rubeai et al., 1990; Franek et al., 1993: Singh et al., 1994). In order to determine the susceptibility of H166 hybridomas to apoptosis, cells were grown in batch culture, and the cell density, viability and extent of apoptosis were monitored. A 250-ml spinner flask was seeded at a cell density of 3.0 x 10^5 viable cells/ml and was monitored until a majority of the cells had died. The hybridomas reached a maximum viable cell density of 2.26 x 10^6 cell/ml after 105 h, at

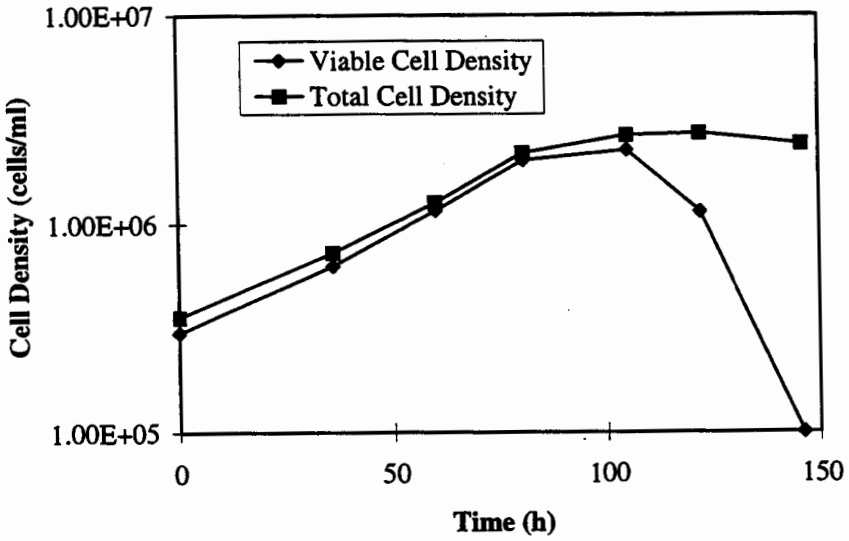

Figure 3. Total and viable cell densities of H166 hybridoma cells growing in batch culture.

which point the viable cell density and the viability began to drop off (Figure 3).

The cells were analyzed for the extent of apoptosis by observing cell morphology using

flourescence microscopy. The total percent of apoptotic cells correlated closely with the percent of non-viable cells (Figure 4a). This confirms that apoptosis is the primary mode of cell death for H166 hybridoma cells during the decline phase of batch culture. Greater than 80% of the cells died as the result of apoptosis, which is similar to the results of Singh et al. (1994). They determined that 60-90% of hybridoma cells die in batch culture as the result of apoptosis.

By analyzing cell morphology, the viable/apoptotic and non-viable/apoptotic cells can also be distinguished. At 122 h, the viable/apoptotic cells make up 5.6% of the total cell population, while this value is 1-2% during normal culture conditions (Figure 4b). Since viable/apoptotic cells last for only a few hours in culture, this suggests that the cells are rapidly dying due to apoptosis. It may be possible to control hybridoma cultures by monitoring the extent of apoptosis. After 146 h, all the cells are non-viable cells, while the percent of apoptotic cells reaches 83%. The remaining 17% of the cells are either necrotic or secondary apoptotic cells. Secondary apoptotic cells are cells that have already begun to form apoptotic bodies and the remainder of the nucleus is beginning to break down. These results show that H166 hybridomas are extremely sensitive to apoptosis, especially during the decline phase of batch culture.

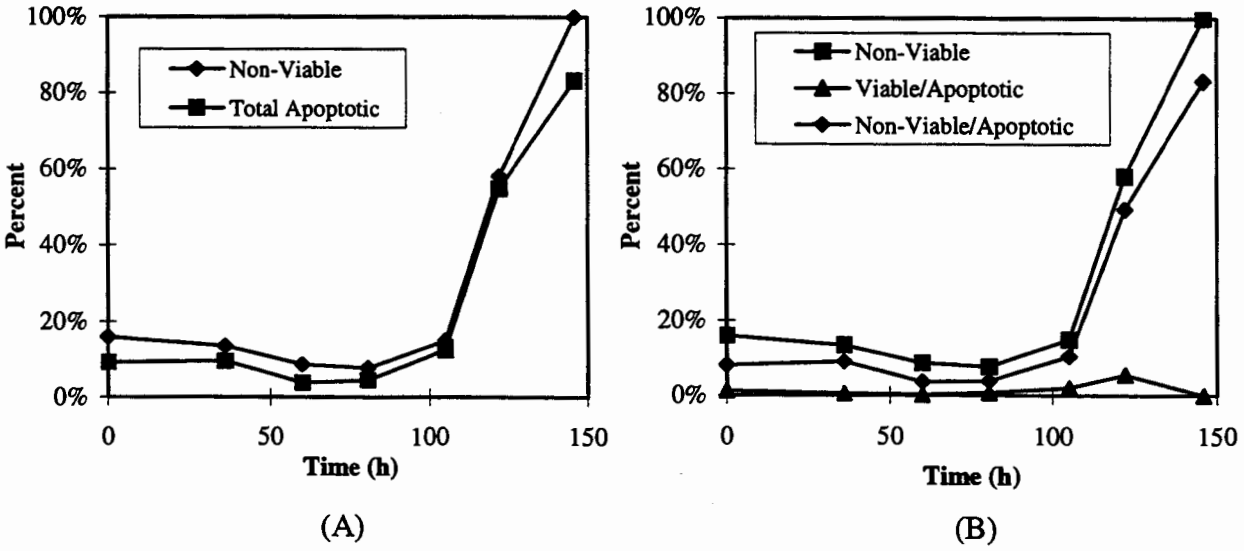

Figure 4. (A) Percentage of non-viable and total apoptotic cells in batch culture. (B) Percentage of non-viable, viable/apoptotic and non-viable/apoptotic cells in batch culture.

Apoptosis in hybridoma perfusion culture with high cell retention

The previous experiment shows that H166 hybridoma cells are susceptible to apoptosis during batch culture. The next step was to determine the role that apoptosis plays in limiting the maximum viable cell density that can be achieved in perfusion culture. It is likely that the H166 hybridomas will also die in perfusion culture as the result of apoptosis, but there are numerous additional stresses on the cells in perfusion culture that could lead to cell death via necrosis. These include stresses due to oxygenation and recirculation through the hollow fiber membrane. This experiment was designed to determine if apoptosis is the primary mode of cell death in perfusion culture.

In order to investigate the cause of cell death, cells were grown in perfusion culture at very high cell retention, which is known to lead to low viabilities and eventually the shutdown of the system. Each of three reactors was seeded with 3.3×10^5 viable cell/ml in a 650-ml working reactor volume, at a viability of 87%. Reactors were started in perfusion mode after running for 70 h in batch, when the viable cell densities grew to greater than 2×10^6 cells/ml, with viabilities greater than 88%. The Masterflex pumps were set to provide average dilution rates of 0.35, 0.58 and 1.05 vol/day, respectively. These dilution rates remained relatively stable throughout the culture period. The cell-free bleed or permeate from each reactor was set to 90% of the dilution rate. This provided a high enough level of cell retention such that dead cells began to build up in the system. Steady state was not achieved and the cells eventually died.

Cell densities and viabilities were determined by staining the cells with Erythrosin B and counting on a hemocytometer, while the extent of apoptosis was determined by labeling the cells using an Apoptag Direct Kit (Oncor) and analyzing by flow cytometry. The viabilities remained high for the first 100-150 h of culture, and then began to drop off quickly (after about 50 h in perfusion culture) (Figure 5a). The viable cell densities grew to 4.48×10^6, 4.63×10^6, and 7.14×10^6 cells/ml, for each of the three reactors. They leveled off after about 200 h in culture and then began to drop off quickly. The low maximum viable cell densities were due to the relatively low dilution rates that were used in this experiment. Also, since the cells were initially grown at high cell retentions, there was not enough time for viable cell densities to build up. In later experiments, viable cell densities as great as 1.2×10^7 cells/ml were obtained, similar to that achieved by previous investigators (Banik and Heath, 1995). Reactors were continued in perfusion mode until the viabilities dropped to below 40%.

The percent of apoptotic cells correlates very closely to the percent of non-viable cells (Figure 5b-d), indicating that apoptosis is the primary mode of cell death in high cell retention perfusion cultures. In two of the reactors, the percentage of apoptotic cells is actually greater than the percent of non-viable cells. While experimental error may contribute, the discrepancy could be a result of the fact that DNA fragmentation begins before the cell membrane becomes permeable. Cells that exclude Erythrosin B dye, and thus appear viable, could actually be apoptotic.

This experiment shows that H166 hybridomas grown in high cell retention perfusion culture die primarily as the result of apoptosis. It is likely that the cells in a perfusion culture operated at steady state also die primarily as the result of apoptosis. The important issue is that apoptosis appears to necessitate a higher cell bleed. In general, in order to increase the cell density, the cell retention at steady state must be reduced. It seems likely that the steady state cell density in a perfusion reactor can be increased by limiting cell death due to apoptosis.

Development of h166 hybridoma cells that express bcl-2

In order to decrease the extent of apoptosis in perfusion culture, hybridomas that express bcl-2 are being obtained. Bcl-2 has an anti-apoptotic effect on hybridoma cells (Itoh et al., 1995; Simpson et al. 1997). The Clontech Et-off gene expression system was used to obtain hybridomas that express bcl-2. This expression system allows for the inducible control of bcl-2 expression in the presence of tetracycline. Four different plasmids are used in order to obtain inducible bcl-2 production in the hybridoma cells. The plasmids pTet-off, pTRE and pTK-Hyg were obtained from Clontech, while pTRE-bcl2 was obtained from Dr. Dong X. Yin. This system was

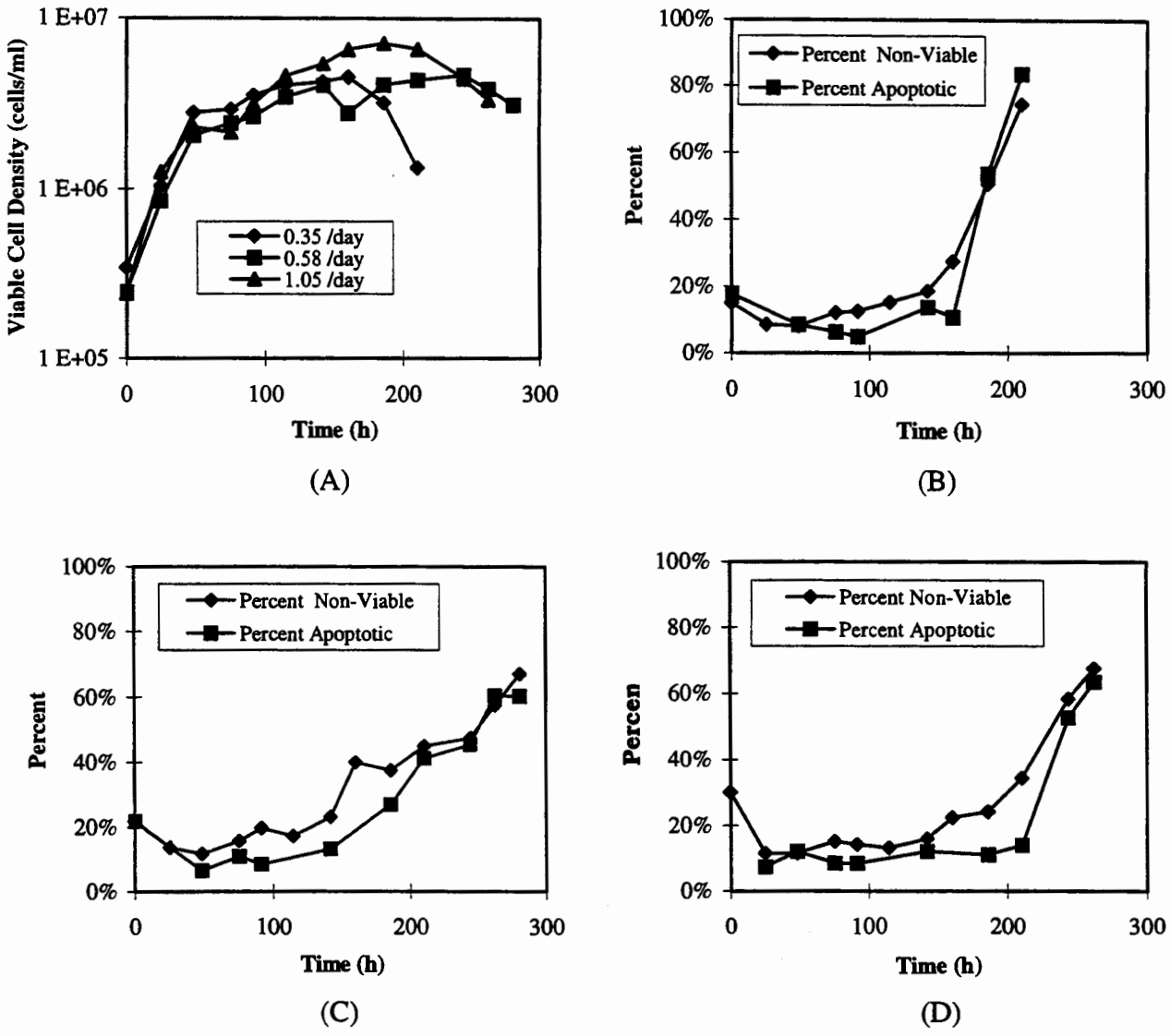

Figure 5. Viable cell density (A) of hybridomas in perfusion culture with high cell retention. Percentage of apoptotic and nonviable cells for perfusion rates of (B) 0.35, (C) 0.58, (D) 1.05 reactor volumes per day.

previously used by Yin and Schimke (1995) to obtain inducible bcl-2 expression in HeLa cells.

The hybridoma cells were initially transfected with the pTet-off plasmid, which produces a hybrid protein known as the tetracycline response transcriptional activator (tTA). This protein contains portions of both the Tet repressor (TetR) and the VP16 protein of herpes simplex virus, and acts as a transcriptional activator in the absence of tetracycline. Positive clones were selected for in the presence of 600 μg/ml G418 selective antibiotic.

Next, the hybridomas were co-transfected with either pTRE or pTRE-bcl2, and pTK-Hyg plasmids. The pTRE-bcl2 plasmid contains the cDNA for bcl-2 and is used in order to generate hybridomas with bcl-2 expression. This plasmid contains seven copies of the 42-bp tet operator

sequence located just upstream of a minimal CMV promoter. This plasmid lacks the strong enhancer normally associated with the CMV promoter. In the absence of tetracycline, the tet repressor binds to the tet operator sequence and thereby activates transcription. The pTRE plasmid is similar to the pTRE-bcl2 plasmid, but lacks the bcl-2 cDNA insert and is used as a negative control. The pTK-Hyg plasmid allows for positively transfected cells to be selected for in the presence of 400 μg/ml hygromycin B. An overview of the Clontech tet-off gene expression system is shown in Figure 6.

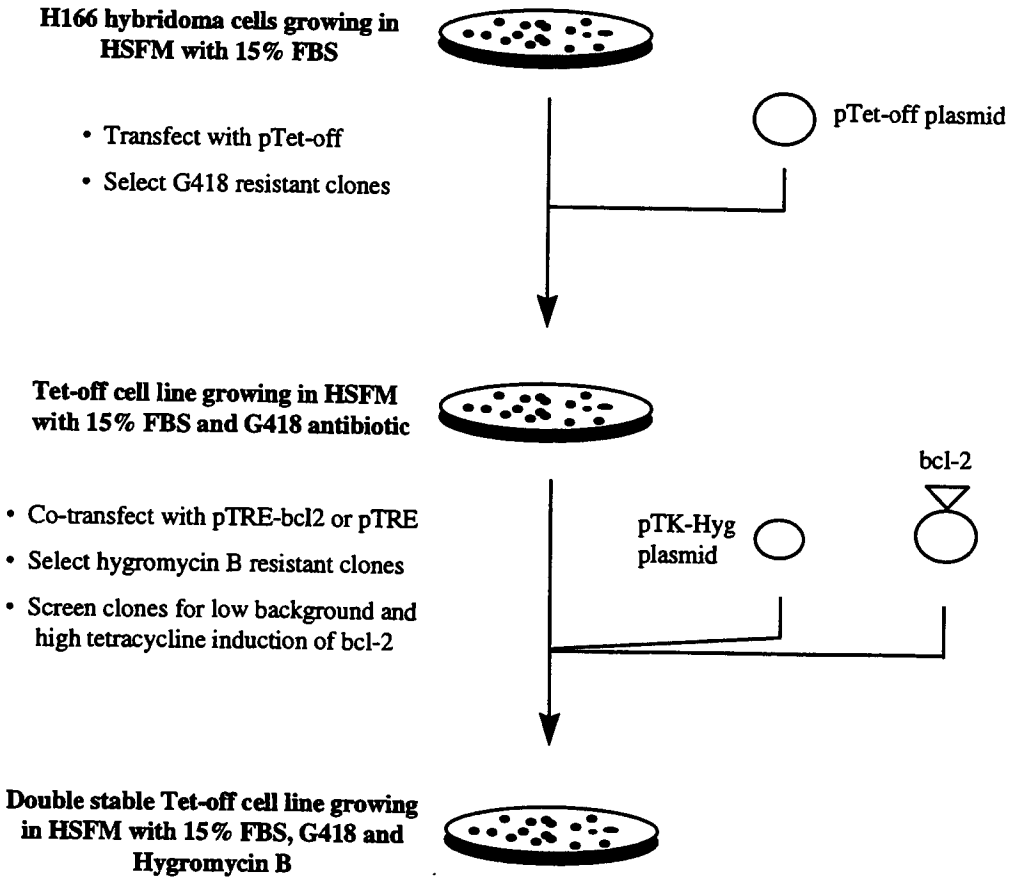

Figure 6. Overview of developing a double stable tet-off H166 hybridoma cell line.

To date, double stable clones have been obtained that contain both G418 and hygromycin B resistance. The next step is to confirm bcl-2 expression by western blotting. Clones with low background and high tetracycline induction of bcl-2 will then be isolated. Once these clones are obtained, cells will be grown in perfusion culture at various concentrations of tetracycline, which determines the level of bcl-2 expression. The cell density, viability, extent of apoptosis, and antibody productivity will be monitored in order to determine the effect of the level of bcl-2 expression on productivity in perfusion culture.

CONCLUSIONS

Apoptosis appears to be the primary mode of cell death in H166 hybridoma cells grown in

both batch and perfusion cultures. In a batch culture of H166 hybridoma cells, it was determined that greater than 80% of the cells died as the result of apoptosis, while in perfusion cultures grown at high cell retention, the percent of apoptotic cells correlated closely with the percent of non-viable cells. Since cell death via apoptosis is significant during perfusion culture, it seems likely that apoptosis may cause a decrease in the maximum steady-state viable cell density that can be achieved. In order to prevent cell death and possibly increase the steady state viable cell density that can be achieved in perfusion culture, the H166 hybridoma cells have been transfected with various plasmids in order to induce expression of bcl-2. Bcl-2 has an anti-apoptotic effect in hybridoma cells (Itoh et al., 1995; Simpson et al., 1997). It is hoped that increased expression of bcl-2 will lead to a decrease in cell death due to apoptosis and lead to higher viable cell densities and antibody productivities in perfusion culture.

ACKNOWLEDGMENTS

This work was supported by funding from the National Science Foundation, Abbott Laboratories, and the Iowa State University Office of Biotechnology. We would also like to thank Abbott Laboratories for the donation of the H166 hybridoma cell line and Dr. Dong X. Yin (Stanford University) for donating the pTRE modified plasmid containing the cDNA for bcl-2.

REFERENCES

Al-Rubeai, M., R.P. Singh, M.H. Goldman, and A.N. Emery, Death Mechanisms of Animal Cells in Conditions of Intensive Agitation. *Biotechnol. Bioeng.*, 1995. **45**: 463-472.

Banik, G.G. and C.A. Heath, Hybridoma Growth and Antibody Production as a Function of Cell Density and Specific Growth Rate in Perfusion Culture. *Biotechnol. Bioeng.*, 1995. **48**:289-300.

De la Broise, D., M. Noiseux, B. Massie, R. Lemieux, Long-Term Perfusion Culture of Hybridoma: A "Grow or Die" Cell Cycle System. *Biotechnol. Bioeng.*, 1991. **38**:781-787.

Franek, F. and T. Vomastek, Fragmented DNA and Apoptotic Bodies Document the Programmed Way of Cell Death in Hybridoma Cultures. *Cytotechnol.*, 1992. **9**:117-123.

Itoh, Y., H. Ueda, and E. Suzuki, Overexpression of bcl-2, Apoptosis Suppressing Gene: Prolonged Viable Culture Period of Hybridoma and Enhanced Antibody Production. *Biotechnol. Bioeng.*, 1995. **48**:118-122.

Kohler, G. and C. Milstein, Continuous Cultures of Fused Cells Secreting Antibody of Predefined Specificity. *Nature*, 1975. **256**:495-497.

Perreault, J. and R. Lemieux, Rapid Apoptotic Cell Death of B-Cell Hybridomas in Absence of Gene Expression. *J. Cell. Physiol.*, 1993. **156**:286-293.

Simpson, N.H., A.E. Milner, and M. Al-Rubeai, Enhancement of Survivability of Mammalian Cells During Suboptimal Culture Conditions. *Biotechnol. Bioeng.*, 1997. **54**:1-16.

Singh, R.P., M. Al-Rubeai, C.D. Gregory, and A.N. Emery, Cell Death in Bioreactors: A Role for Apoptosis. *Biotechnol. Bioeng.*, 1994. **44**:720-726.

Wyllie, A.H., Glucocorticoid-Induced Thymocyte Apoptosis is Associated with Endogenous Endonuclease Activation. *Nature*, 1980. **284**:555-556.

Yin, D.X. and R.T. Schimke, Bcl-2 Expression Delays Drug-Induced Apoptosis but Does Not Increase Clonogenic Survival after Drug Treatment in HeLa Cells. *Cancer Res.*, 1995. **55**:4922-4928.

Mathematical Modeling of Fluid Dynamics in the Eye

Jeffrey Heys and Victor H. Barocas, Department of Chemical Engineering,
University of Colorado, Boulder, CO 80309

Introduction

Aqueous humor (AH) is a transparent fluid that provides nutrition for avascular ocular tissues in the eye. The AH is actively secreted by the ciliary processes into the posterior chamber (between the lens and iris, Fig. 1), passes through the pupil, enters the anterior chamber, and eventually exits through the trabecular meshwork. A second outflow passage for AH is the uveoscleral route. This route is near the trabecular meshwork and accounts for <10% of the total outflow (Van Buskirk, 1997). The third and least significant (< 5% in normal eyes) route for AH to flow out of the eye is anteriorly through the vitreous gel (Bill, 1993), which comprises most of the volume of the eye posterior to the lens. AH is secreted at a rate of approximately 2 μL/min, which results in a turnover of fluid approximately every 100 min (Caprioli, 1992).

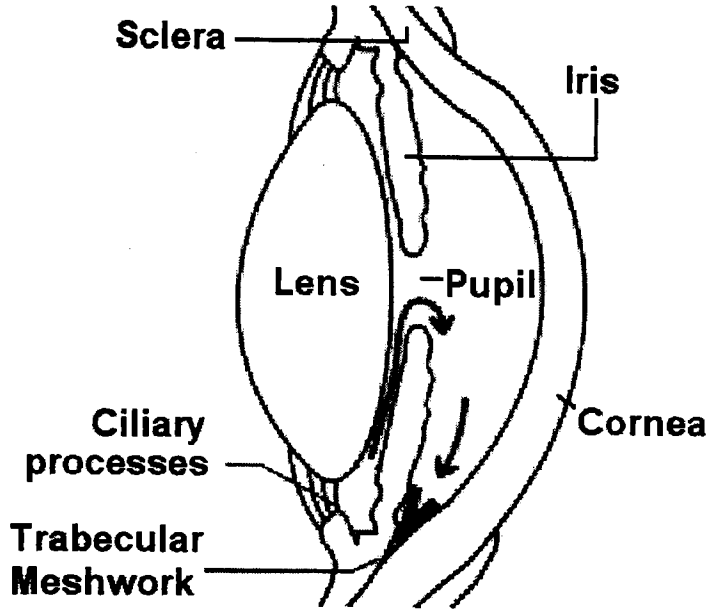

Fig. 1. Cross-section of the anterior segment of the eye showing the path of aqueous humor. The aqueous humor is secreted by the ciliary body and exits the eye through the trabecular meshwork. The posterior chamber is between the iris and lens, and the anterior chamber is between the cornea and iris.

The contour of the iris and its position in relation to other structures in the anterior chamber (i.e., the cornea and the lens) are consequential in many forms of glaucoma (Liebmann and Ritch, 1996). \ We propose that the interaction of the AH with the iris significantly influences the contour and position of the iris based on clinical observations of the iris contour dramatically changing after the iris is dilated (Taravella, 1998). This interaction and the flow pattern of the AH is described in this paper using a mathematical model of the anterior segment of the eye.

The coupling between the AH flow and the iris displacement may be especially important in pigmentary glaucoma, a form of glaucoma in which pigment particles from the iris are deposited in the trabecular meshwork, increasing outflow resistance. The iris is bowed posteriorly in these patients bring it in close proximity to the lens and zonules (the fibers connecting the lens to the

ciliary body) (Pavlin, *et al.*, 1996). It is not yet understood how the iris could be bowed posteriorly, indicating a higher pressure in the anterior chamber compared to the posterior chamber, while the pigment from the posterior iris surface is deposited in the trabecular meshwork, indicating a lower anterior chamber pressure.

The small size, difficult accessibility, and low flow rate cause difficulty when experimentally measuring the flow of AH in the eye. Tracer substances have been used by researchers to measure the rate of aqueous humor flow (Smith, 1991). These measurements are difficult for two reasons. First, the rate of aqueous humor production by the ciliary processes varies by as much as 50% depending on the time of day (Smith, 1991). Second, diffusion contributes significantly to the total tracer flux in the anterior chamber. Tracer methods are effective in measuring the total rate of aqueous humor flow, but are not valuable in determining the flow pattern of AH in the anterior segment.

Limited theoretical work has been performed on the eye, especially with regard to the interaction between the AH and iris. Tiedeman (1991) attempted to solve for the contour of the iris by modeling it as a pressure relief valve. In this model, the edges of the iris are fixed, there is a tension placed on the iris at the inner radius, and there is a uniform pressure acting on the lower surface. The model assumes the iris is infinitely thin, and it ignores the flow of fluid in the eye. These and other simplifications greatly reduce the usefulness of the model. A mathematical model of the cornea in conjunction with inflation experiments on the cornea was used by Bryant and McDonnell (1996) to describe the mechanical properties of the cornea. The model used the finite element method to solve differential equations that are similar to those used in this work to describe the iris. A finite element model of vitreous gel has been developed by Friedrich *et al.* (1997) to describe the diffusion of drugs in the vitreous region. This model encompasses most of the posterior segment of the eye, which is not modeled in this work.

Materials and Methods

Aqueous humor has a density, ρ, of 1.05 g/cm^3 and a viscosity, μ, of 1.03 cP (Hart 1992). The fluid is modeled using the steady-state form of the Navier-Stokes equation:

$$\rho(\underline{v}\cdot\nabla\underline{v}) = -\nabla P + \mu\nabla\cdot(\nabla\underline{v} + (\nabla\underline{v})^T) \tag{1}$$

and the incompressibility relation:

$$\nabla\cdot\underline{v} = 0 \tag{2}$$

Experiments on the bovine iris have shown the tissue to be incompressible and linear elastic under small deformations with a modulus, G, of 1.6 kPa in the radial direction (Heys and Barocas, 1998). These measurements form the basis for modeling the human iris and support the use of the following equations to model the iris:

$$-\nabla P + G\nabla\cdot(\nabla\underline{u} + (\nabla\underline{u})^T) = 0 \tag{3}$$

$$\nabla\cdot\underline{u} = 0 \tag{4}$$

In equations 3 and 4, $\underline{u}$ is the displacement from the rest position.

The boundary conditions used for the model are summarized in Fig. 2:

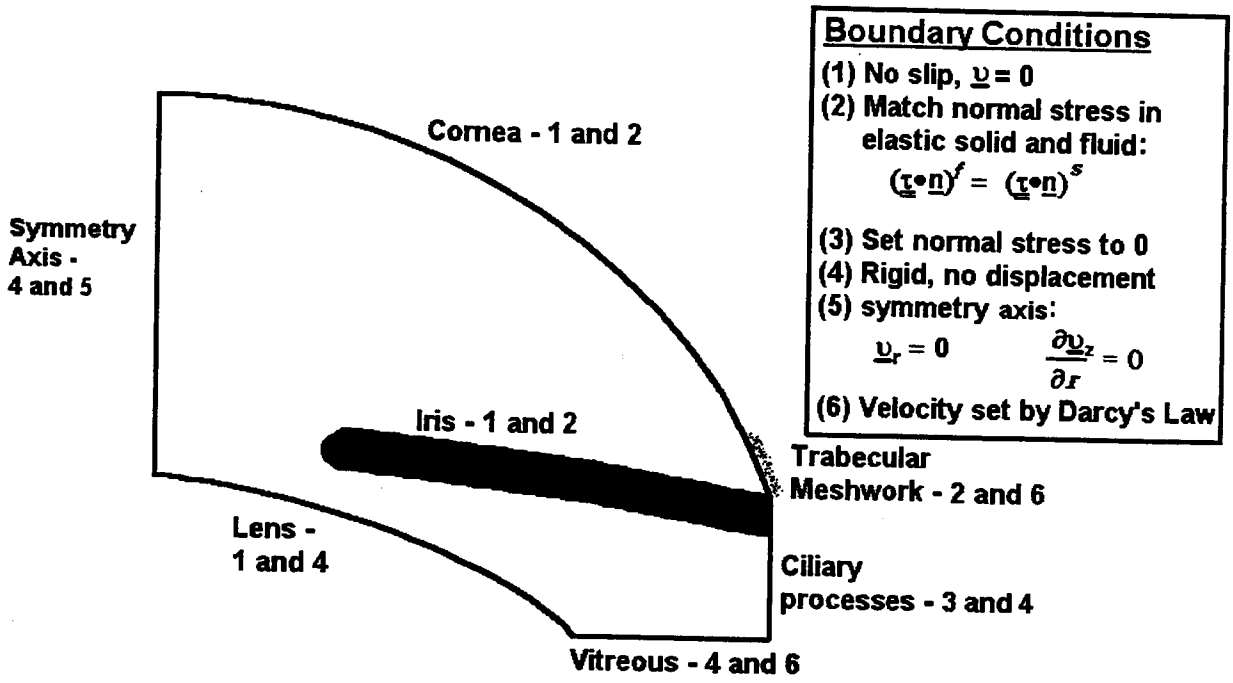

Fig. 2. A summary of the boundary conditions used in the model. The fluid domain is shown in white, and the elastic solid domain is shaded.

The velocity in the radial direction through the trabecular meshwork and the velocity in the axial direction along the vitreous gel are calculated using Darcy's law:

$$v_n = \left(\frac{k}{L}\right)(\sigma_{nn} - P_{Vein}) \tag{5}$$

The venous pressure, P_{vein}, is estimated to be 9 mm Hg (Johnson and Kamm, 1983). The permeability, k, has been measured in the vitreous of the bovine eye by Fatt (1977) to be 8.9×10^{-12} $m^4\ N^{-1}\ s^{-1}$. The distance throught the vitreous, L, is approximated as 1 cm (Friedrich, *et al.*, 1997). The quantity k/L has been measured for the human trabecular meshwork by Allingham *et al.* (1992) to be 1.7×10^{-9} $m^2\ s\ kg^{-1}$. The normal stress along the inlet is set to zero so that the pressure can be easily scaled in the problem. The axial displacement of the cornea is calculated using the following equation (based on Perktold *et al.* (1994)):

$$\sigma_{zz} = P_0 + \frac{E \cdot u_z}{L_{cornea}} \tag{6}$$

In this equation, the cornea modulus, E, is set to 1×10^3 kPa (Smolek, 1994) causing the axial displacement, u_z, to be small. The displacement of the iris is calculated by setting the traction in the fluid equal to the traction exerted by the iris.

The finite element mesh is generated using the commercial package FIGEN, which is a module of FIDAP (Fluent Incorporated; Lebanon, NH). FIGEN uses the paving technique to create a mesh for irregular domains, such as that used in this problem. The mesh in the aqueous region must be

moved to due to the movement of the iris. The mesh is moved based on the solution to the compressible elastic equation on that domain:

$$\lambda(\nabla(\nabla \cdot \underline{u})) + \nabla^2 \underline{u} = 0 \tag{7}$$

where λ is a Lame coefficient and is a function of Poisson's ratio in this equation. This is a technique developed by Sackinger *et al.* (1996) for free and moving boundary problems and is referred to henceforth as the pseudo-solid domain mapping technique.

The rest position of the iris is assumed to be planar (Taravella, 1998). Unfortunately, it is not possible to create a finite element mesh with the iris in the planar position because this would require the iris mesh to overlap the aqueous domain mesh. The model is therefore set up so that the mesh is generated with the iris in a guessed position. Then, the rest position of the iris in the model is set as if the iris were planar.

The finite element discritization of the model equations is accomplished by a mixed formulation. The velocity and displacement are described by peicewise biquadratic basis functions, and the pressure is described by peicewise linear basis functions. The linear problem associated with each Newton iteration is solved using the preconditioned GMRES (Generalized Minimum RESidual) iterative method (Saad and Schultz, 1986). An ILU preconditioner is used to improve the convergence of GMRES.

Results

Fig. 3 is a sample flow pattern produced using conditions found in the normal eye. We believe that this is the first flow pattern determined experimentally or theoretically for the flow of

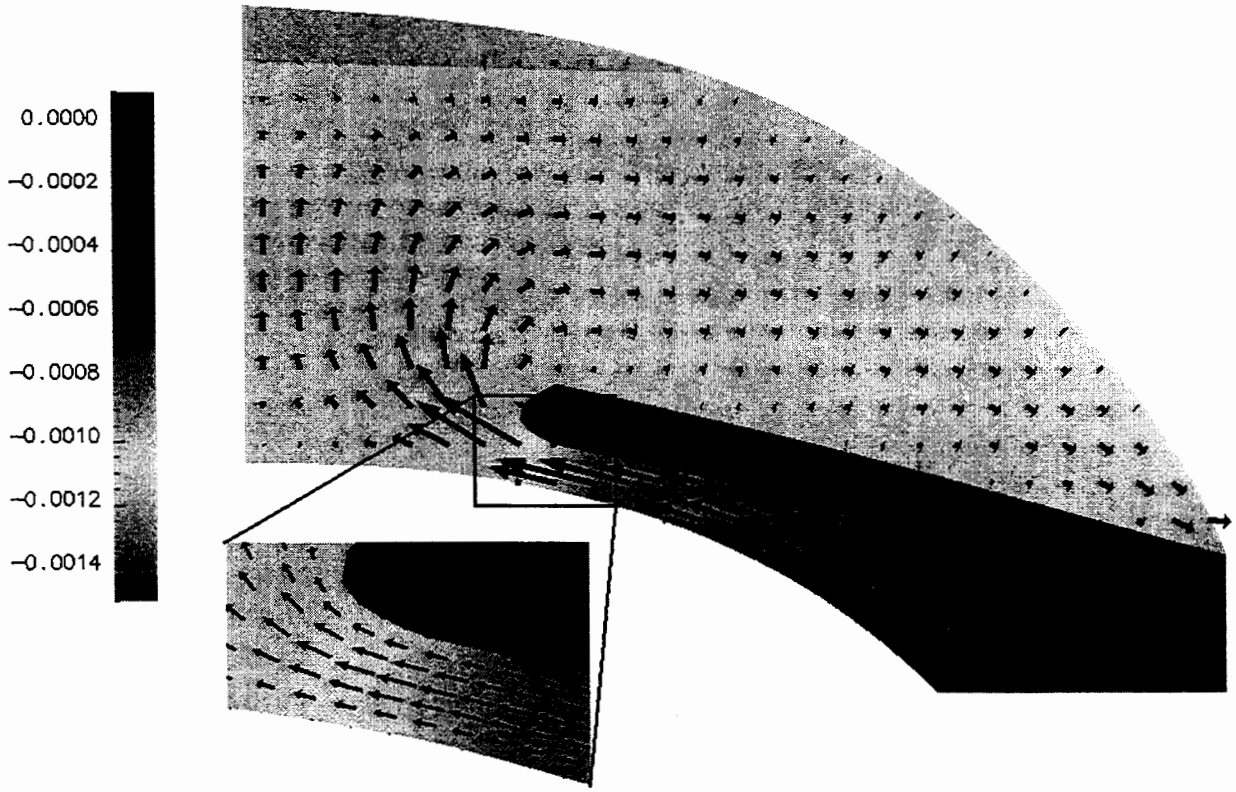

Fig. 3. A flow pattern for a normal eye with the pressure given in Pa. The velocity vectors in the main picture are interpolated from the complete solution for clarity. The vectors in the blown up image have not been interpolated and represent the actual solution.

aqueous in the anterior portion of the eye. The gauge pressure in the eye is approximately 2.0 kPa, and the venous pressure is set to 1.1 kPa (Johnson and Kamm, 1983). The flow rate of aqueous in the eye is 2 μL/min, and the modulus of the iris is set to 1.6 kPa, which is based on the modulus of the bovine eye in the radial direction (Heys and Barocas, 1998).

Many different parameters in the model have been examined for their influence on the flow pattern and iris displacement. One of the most promising results was obtained when the flow through the trabecular meshwork was reversed so that a small amount of fluid flowed back into the anterior chamber. This situation may occur during a blink (Campbell, 1994), or, equivalently, if there were flow from the anterior surface of the iris near the attachment as proposed by Epstein (1997). The result of this change is shown in Fig. 4. The contour of the iris is now concave, and the pressure in the anterior chamber is higher than the posterior chamber. These are both symptoms of pigmentary glaucoma.

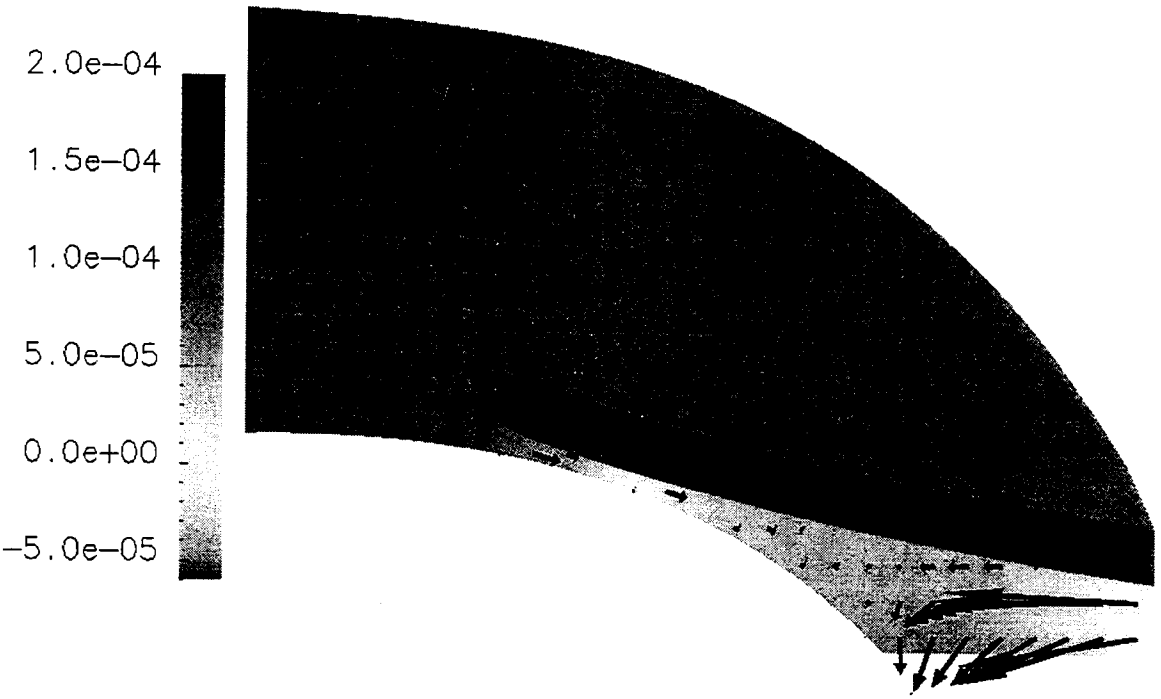

Fig. 4. A flow pattern for an eye that has flow into the anterior chamber from the trabecular meshwork. This condition may occur when the subject blinks. The concave shape of the iris and the higher pressure in the anterior chamber are common symptoms of pigmentary glaucoma.

Miotic drugs, which cause the pupil to constrict, are a common form of treatment for pigmentary glaucoma. Miotics also act by opening the pores in the trabecular meshwork and increasing the outflow facility. Clinicians observe the iris in pigmentary glaucoma patents moving away from the lens and zonules and losing the convex shape when miotics are used for treatment. The pupil diameter in the model of a normal eye was dilated from 4 mm (as in Fig. 3) to 2 mm (Fig. 5), while maintaining a constant iris volume. This numerical experiment was performed using the parameters of a normal eye based on the assumption that the miotic drugs increase the outflow facility in a PG eye until it is close to that of a normal eye. The model shows that the pressure in the posterior chamber is higher relative to the anterior chamber with the pupil constricted. This increased pressure difference results in the iris having a convex shape and having a larger displacement away from the lens and zonules.

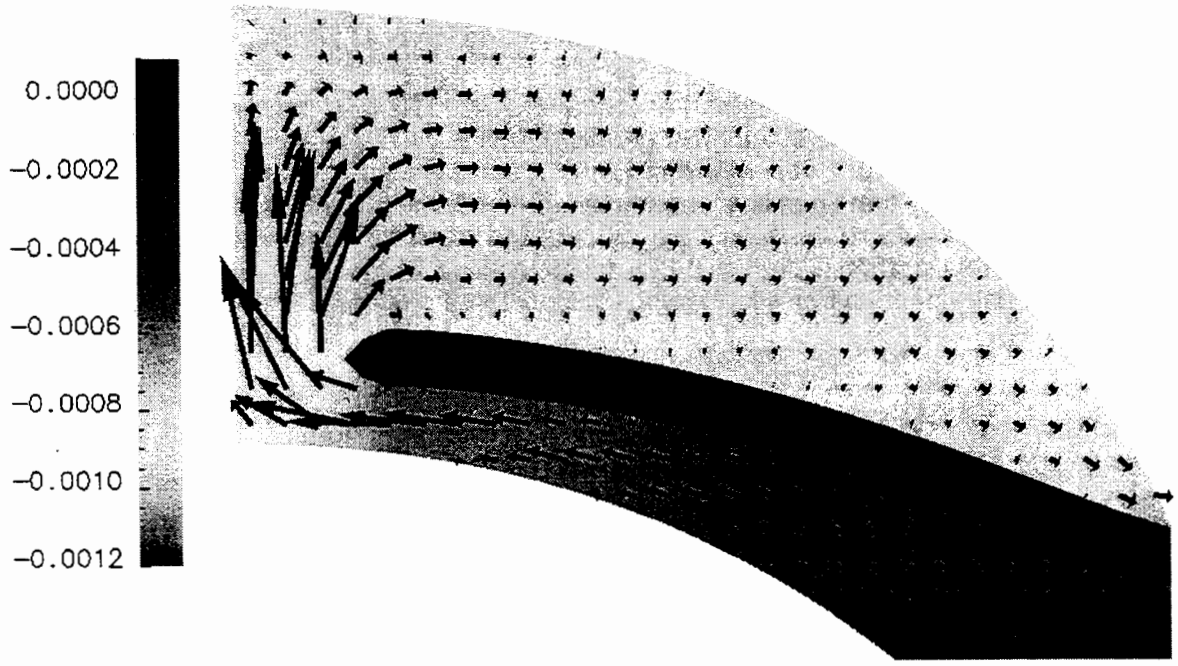

Fig. 5. Flow pattern for an eye with the pupil constricted to 2 mm. This is a smaller pupil diameter than the problem domain shown in Fig. 4, which has a pupil diameter of 4 mm. The iris has a convex contour and is displaced away from the lens. This illustrates one of the mechanisms by which miotic drugs treat pigmentary glaucoma.

Discussion

The difficulties associated with experimentally determining the flow pattern in the eye are well documented (e.g., Smith, 1991). We have developed a mathematical model of the anterior segment that enables theoretical investigation of the coupled fluid-elastic system. The finite element method in conjunction with the pseudo-solid domain mapping technique is used to model these complex systems. The model of a normal eye shows the iris being displaced by the AH as it circulated through the anterior segment. The iris displacement is a function of the aqueous flow rate, fluid viscosity, iris modulus, and other, less important, parameters.

There are two major assumptions made about the eye: steady-state and axisymmetry. The eye is a constantly changing system due to factors such as focusing and blinking. The magnitude of these changes is normally small making the assumption of a steady-state system valid. For example, The average displacement of the lens during focusing is 0.14 mm, which is only 4% of the total anterior chamber depth (Pavlin, *et al.*, 1996). Yet, many of the theories related to pigmentary glaucoma are based on transient phenomena. An important future modification to the model is the ability to model transient phenomena. The other major assumption made with the model is that of axisymmetry. Although the normal human eye has a slight asymmetry due to the location of the iris, this assumption is generally valid. One of the newest treatments for glaucoma is an iridotomy, which is a laser surgery in which small holes are burned in the iris. This treatment cannot be modeled until a three-dimensional model is developed.

The model predicted that miotic drugs would cause the displacement of the iris from the lens to be increased by increasing the resistance to flow between the anterior and posterior cham-

bers. In addition, the model predicted that the iris would achieve a convex shape in contrast to the normal flat or slightly concave shape. It is not possible to predict the change in trabecular meshwork permeability due to miotic drugs so the effects of miotic drugs on PG eyes can not be completely described at this time. It is promising that the predicted effects of miotic drugs on normal eyes are similar to the effects observed by clinicians for patients with PG.

References

Allingham, R. R., A. W. d. Kater, et al. (1992). "The Relationship Between Pore Density and Outflow Facility in Human Eyes." *Investig. Ophthalmol. Visual Sci.* **33**: 1661-1669.

Bill, A. (1993). "Some Aspects of Aqueous Humour Drainage." Eye **7**: 14-19.

Bryant, M. R. and P. J. McDonnell (1996). "Constitutive Laws for Biomechanical Modeling of Refractive Surgery." *J. Biomech. Eng.* **118**: 473-481.

Campbell, D. G. (1994). "Pigmentary Glaucoma: Mechanism and Role for Laser Iridotomy." *J. Glaucoma* **3**: 173-174.

Caprioli, J. (1992). The Ciliary Epithelia and Aqueous Humor. *Adler's Physiology of the Eye : Clinical Application*. W. M. Hart, ed.. St. Louis, Mosby Year Book: 228-247.

Epstein, D. L. (1997). Pigment Dispersion and Pigmentary Glaucoma. *Chandler and Grant's Glaucoma*. D.L. Epstein, ed. Baltimore, Williams & Wilkins: 220-231.

Fatt, I. (1977). "Hydraulic Flow Conductivity of the Vitreous Gel." *Invest. Ophthalmol. Visual Sci.* **16**: 565-568.

Friedrich, S., B. Saville, et al. (1997). "Drug Distribution in the Vitreous Humor of the Human Eye: The Effects of Aphakia and Changes in Retinal Permeability and Vitreous Diffusivity." *J. Ocular Pharmacol. Therapeut.* **13**: 445-459.

Hart, W. M., ed. (1992). *Adler's Physiology of the Eye*. St. Louis, Mosby Year Book.

Heys, J. and V. H. Barocas (1998). "Mechanical Characterization of the Bovine Iris." *J. Biomech.*, submitted.

Johnson, M. C. and R. D. Kamm (1983). "The Role of Schlemm's Canal in Aqueous Outflow from the Human Eye." *Invest. Ophthalmol. Vis. Sci.* **24**: 320-325.

Liebmann, J. M. and R. Ritch (1996). "Ultrasound Biomicroscopy of the Anterior Segment." *J. Am. Optomet. Assoc.* **67**: 469-479.

Pavlin, C. J., P. Macken, et al. (1996). "Accommodation and Iridotomy in the Pigment Dispersion Syndrome." *Ophthal. Surg. Lasers* **27**: 113-120.

Perktold, K., E. Thurner, et al. (1994). "Flow and Stress Characteristics in Rigid Walled and Compliant Carotid Artery Bifurcation Models." *Med. Biol. Eng. Comput.* **32**: 19-26.

Saad, Y. and M. H. Schultz (1986). "GMRES: A Generalized Minimum Residual Algorithm For Solving Nonsymmetric Linear Systems." *SIAM J. Sci. Stat. Comput.* **7**: 856-869.

Sackinger, P. A., P. R. Schunk, et al. (1996). "A Newton-Raphson-Solid Domain Mapping Technique for Free and Moving Boundary Problems: A Finite Element Implementation." *J. Comput. Phys.* **125**: 83-103.

Smith, S. D. (1991). "Measurement of the Rate of Aqueous Humor Flow." *Yale J. Biol. Med.* **64**: 89-102.

Smolek, M. K. (1994). "Holographic Interferometry of Intact and Radially Incised Human Eye-bank Corneas." *J. Cataract Refract. Surg.* **20**: 277-286.

Taravella, M. (1998). Personal communication.

Tiedeman, J. S. (1991). "A Physical Analysis of the Factors That Determine the Contour of the Iris." *Am. J. Ophthalmol.* **111**: 338-343.

Van Buskirk, E. M. (1997). Anatomy. *Chandler and Grant's Glaucoma*. D. L. Epstein, ed.. Baltimore, Williams & Wilkins: 6-17.

The Influence of the Conduit on Regeneration in a Bioartificial Nerve Graft

Gregory E. Rutkowski and Carole A. Heath
Department of Chemical Engineering
Iowa State University
Ames, IA 50011-2230

ABSTRACT

Nerve injuries complicate successful rehabilitation more than any other form of trauma because of loss of protective sensibility and tactile discrimination, denervation atrophy of muscles, and pain syndromes. While achieving full function and organ reinnervation after peripheral nerve injury is a challenge, a promising method of improving the rate and success of regeneration is the bioartificial nerve graft (BNG). An BNG under development in our laboratory consists of a porous resorbable tube containing cultured Schwann cells that help to direct and support nerve regeneration when used to bridge the gap between the ends of the severed nerve.

To aid in the design of the BNG, a simple reaction and diffusion model has been developed to describe the transport and uptake of nutrients by cells in the graft. Implementation of the model has required experimental determination of several key parameters, including nutrient diffusivities as a function of polymer porosity with and without the presence of Schwann cells, nutrient consumption rates, and productivity of nerve growth factor, a potent stimulator of regeneration.

INTRODUCTION

The peripheral nervous system is comprised of two different cell types, neurons and Schwann cells. Neurons carry the electrical signal or action potential to all parts of the body. An electrical signal is initiated in the dendrites of the neuron and is propagated down the length of the axon. At the end of the axon, neurotransmitters are released into the synapse and detected by receptors located in the dendrites of another neuron thus continuing the transmission of the action potential. Schwann cells provide trophic support for the neurons during regeneration and enhance signaling by forming an insulating layer around the axons called the myelin sheath.

Injuries to the peripheral nervous system can be debilitating due to the loss of sensory and motor function. The alternatives for the repair of severed nerves are suturing the severed ends together, bridging the gap with an autograft or allograft, or regenerating the axons through an artificial nerve graft. Suturing the nerve ends is only effective over short distances. Autografts and allografts require the use of neural tissue from the patient or a donor. Because autografts lead to denervation and donors are needed for allografts, the artificial nerve graft is a better alternative. One major drawback of the artificial nerve graft is its inability to regenerate axons over gaps of 1 cm or more. A means to overcome this obstacle is to seed the artificial nerve graft with Schwann cells.

Schwann cells aid the regeneration of axons by secreting factors such as nerve growth factor, brain-derived neurotrophic factor, and neurotrophic factor-3, which enhance the growth of the axons. Besides secreted factors, Schwann cells also enhance nerve growth by contact [1]. Once

in contact with the axon, Schwann cells will wrap themselves around the axon to ensheath and remyelinate the neuron. Another advantage to using Schwann cells is their ability to aid the regeneration of central nervous system axons, although they are not normally found there. In the central nervous system, the glial cells, oligodendrocytes, actually inhibit the growth of axons [2].

Regeneration within the conduit occurs in a manner similar to normal regeneration. Following injury, fluid accumulates within the lumen of the conduit. The distal nerve stump undergoes Wallerian degeneration. Trophic factors are concentrated within the conduit. Fibroblasts migrate into the gap to form a fibrin bridge and will eventually form a new perineurium. The fibrin bridge acts a support structure for the regenerating axons. The axons migrate cocurrently with Schwann cells across the gap. Once the axons reach the distal stump, they enter the endoneurial tubes and will eventually form new synapses.

Four different mechanisms have been theorized to govern regeneration within an artificial nerve graft [3]. Operative alignment states that axon destination is determined by its physical alignment at the site of repair. Contact guidance describes axons recognizing a specific substrate along a particular path [4]. With neurotropism, the direction of axons is determined by a chemical gradient from agents diffusing from the distal stump [3]. In neurotrophism, axons grow along random paths but will receive support when the appropriate contact has been reached [5]. Although each of these mechanisms have been demonstrated in experiments, the extent to which each mechanism is important remains controversial and may depend on the type of neuron.

MATERIALS AND METHODS

Incorporation of Schwann cells into the bioartificial nerve graft can greatly enhance regeneration. The initial design consists of Schwann cells seeded along the inner lumen surface of the conduit (Figure 1). The physical properties of the conduit affect the transfer of nutrients and growth factors within the bioartificial nerve graft. Nutrients, oxygen, and glucose diffuse from the bulk fluid through the conduit wall and into the lumen. Both neurons and Schwann cells consume the nutrients. Nerve growth factor (NGF) is produced by Schwann cells and is consumed by the neurons. Mass transfer within the conduit can be described by the equation

$$0 = D_{ij}\left[\frac{1}{r}\frac{d}{dr}\left(r\frac{dC_{ij}}{dr}\right)\right] + R_{ij}$$

The equation assumes mass transfer only in the radial direction. Diffusion and kinetic values were reported previously [6]. The values are summarized in Table 1.

Although the model can describe the transfer of nutrients and nerve growth factor, a relationship between these factors and the growth of axons needs to be evaluated. Neurons were grown in the cultured in tissue culture dishes containing Schwann cells, fibrin or neither (control). Neurons were isolated from the dorsal root ganglia of four-day-old rats, dissociated and then seeded in the dishes at a concentration of 8×10^4 cells/cm^2. Schwann cells were isolated from 16-20 day-old rats and purified using Anti-Thy 1.1 to remove any fibroblasts [7]. Cultures were fed Dulbecco's Modified Eagles Medium with 10% Fetal Bovine Serum. Gentamycin was included to prevent infection. Cultures were fed media with varying nerve growth factor concentrations and the media was replaced every two days.

Table 1: Parameters used in computer model of BNG

	Schwann cells (mg /cell•s)	Axons (mg/axon•s)	D_{bulk} (cm^2/s)	D_{tissue} (cm^2/s)
Oxygen	1.3×10^{-12}	1.27×10^{-9}	3.0×10^{-5}	1.32×10^{-5}
Glucose	7.8×10^{-12}	5.6×10^{-9}	9.1×10^{-6}	3.6×10^{-6}
NGF	2.0×10^{-17}	$k_p = 1 \times 10^{-3}$	5.3×10^{-7}	2.4×10^{-7}

Cultures were removed daily and stained using immunocytochemistry. Briefly, cultures were fixed in 4% paraformaldehyde solution in buffer. Neurons were stained using an antibody to filament protein. Images were obtained for several neurons in each culture. Image analysis was used to evaluate axon length. For the fibrin and control cultures, care was taken to ensure that the axons being measured did not contact other axons or any remaining Schwann cells. Axon length data were collected for each culture condition over an eight-day period. Simple linear regression was performed to determine the extension rate for various NGF and substrate conditions.

RESULTS

The computer model can be used to evaluate the amount of nutrients and nerve growth factor available to the Schwann cells and neurons. Figure 2 shows the effect of conduit wall thickness and porosity on the concentration of NGF and oxygen in the lumen. As expected, low porosity and greater wall thickness increases the resistance to mass transfer and leads to lower oxygen and higher NGF concentrations. From the oxygen uptake rate experiments, oxygen limiting when levels dropped below 2 μg/ml. This limitation leads to a maximum attainable NGF concentration of approximately 4 ng/ml. Glucose was not a limiting nutrient.

The effect of NGF concentration on the axon extension rate is shown in Figure 3. Variations in the measurements of the axons led to large standard error. As a result, NGF concentration does not have a statistically significant effect on the axon extension rate. Sample images used in determining the axon extension rate are shown in Figure 4. No differences were seen in neurons grown on fibrin compared to the control group. Although axons cultured on a layer of Schwann cells grew significantly faster than those cultured on fibrin and the control group, severe branching was noted in all cases.

DISCUSSION

The loss of sensory and motor function due to neural injury warrants the need for a simple treatment that does not require donor tissue. The proposed design of the bioartificial nerve graft can solve some of the problems inherent to recovery from such injuries. The conduit provides physical support and protection for the regenerating axons. The limiting factor in the process of

regeneration is the formation of the neovasculature [8]. A porous conduit can allow the diffusion of essential nutrients, such as oxygen, until new blood vessels have invaded the conduit. The porosity and wall thickness can be optimized to allow the diffusion of nutrients while still retaining in the lumen trophic factors produced by Schwann cells. Ideally, Schwann cells can be isolated from the injury site of the patient and expanded in culture. The cells can be placed into the conduit before it is connected to the severed nerve.

The axon extension rate experiments reveal the importance of using Schwann cells to enhance regeneration. Schwann cells greatly enhance axon growth when compared to cultures fed nerve growth factor alone. The only major drawback appears to be the severe branching as well as undirected growth of axons in random directions. The original design shown in Figure 1 only considered the operative alignment mechanism. The conduit would affect nerve growth by directing the regenerating axons down the lumen. Nerve growth factor produced by the Schwann cells was considered to influence growth by contact with receptors on the axons' cell membrane.

Schwann cells in contact with the neurons enhance growth by other means. p75 receptors, which bind to NGF, BDNF, and NT-3, are found in Schwann cells and may be used to directly hand off the growth factors to the axons [9]. Also, Schwann cells have a basal lamina, a protein membrane that surrounds the cell membrane. Laminin found in the basal lamina enhances the growth of regenerating axons [10].

In the axon extension rate experiments, the fibrin and control cultures still contained some Schwann cells from the dissociation of the dorsal root ganglia. Figure 4 show axons that came in contact with these Schwann cells. These images were not used in the determination of the axon extension rate. Axons appear to be guided toward the Schwann cells by a neurotrophic mechanism. A new design, shown in Figure 5, was developed to take into account these different mechanisms. Instead of being seeded on the inner surface of the conduit, Schwann cells are injected directly into the lumen and suspended in a fibrin matrix. The computer model can be altered to describe the mass transport in the new design. Comparison of the effect of cell density on the two designs is shown in Figure 6. Equivalent amounts of NGF can be obtained in the new design with approximately half the cell density. Also, having a lower Schwann cell density may be more advantageous since the neurotrophic mechanism may enhance regeneration by directing growth to Schwann cells further down the length of the conduit. Schwann cells that come in contact with the axons will change phenotype from the NGF-producing form to the myelin one. This will prevent axons from turning back towards the proximal segment.

Although more studies need to be done to determine which mechanism is most important in the regeneration of peripheral nerves, the current design allows all four mechanisms to be possible. The conduit is used to properly align the proximal and distal segments. Schwann cells produce neurotrophic factors that enhance the growth of axons as well as directing the axons by means of a concentration gradient. In contact with the Schwann cells, axon growth is further enhanced. Although Schwann cells are a promising addition to the enhancement of nerve regeneration, the bioartificial nerve graft needs to be properly designed to allow sufficient nutrients to reach the cells while providing adequate support and protection.

FUTURE WORK

The current design needs to be tested to determine its effectiveness. Conduits have been formed by rods of polyvinyl alcohol that were dipped into a suspension of NaCl in poly-D,L-lactide dissolved in chloroform. The chloroform was allowed to evaporate. The conduit was cut to size and placed in water to dissolve the salt and PVA. Dissolving the PVA rods in water can alter the rod diameter, and thus the conduit inner diameter. The rods can be dipped repeatedly to obtain the desired outer diameter. The porosity is determined from the amount of salt in the suspension. Conduits have been formed with various porosities and wall thicknesses.

Schwann cells will isolated and purified. The cells will be suspended in fibrinogen and injected into the lumen. Thrombin will also be injected to polymerize the fibrinogen into a fibrin matrix. Dorsal root ganglia will be used as a neuron source and placed into one end of the conduit. The other end will be sealed off with silicone to prevent the escape of neurotrophic factors.

Conduits will be cultured over a period of four weeks before being analyzed. The conduits will be fixed and stained for neurons as well as myelin. Cross-sections of the conduit will be taken and examined for axon number, diameter, and degree of myelination. The final results will be compared to conclusions drawn from the model of mass transport.

REFERENCES

1. Gunderson, R.W. and J.N. Barrett, Neuronal chemotaxis: Chick dorsal root axons turn toward high concentrations of nerve growth factor. *Science*, 1979. **206**: 1079-1080.
2. Caroni, P. and M.E. Schwab, Antibody against myelin-associated inhibitor or neurite growth neutralizes nonpermissive substrate properties of CNS white matter. *Neuron*, 1988. **1**: 85-96.
3. Doolabh, V., M. Hertl, and S. Mackinnon, The role of conduits in nerve repair: A review. *Rev. Neurosci.*, 1996. **7**: 47-84.
4. Cajal, S.R.Y., *The Neuron and the Glial Cell*. 1984, Springfield, Ill.: Charles C. Thomas. p. 355.
5. Brushart, T.M.E., The mechanical and humoral control of specificity in nerve repair, in *Operative Nerve Repair and Reconstruction*, R.H. Gelberman, Ed.. 1991, Lippincott: Philadelphia. p. 215-230.
6. Heath, C. and G. Rutkowski. Design of a bioartificial nerve graft. American Institutue of Chemical Engineers Annual Meeting. 1997. Los Angeles, Cal.
7. Brockes, J.P., K.L. Fields, and M.C. Raff, Studies on cultured rat Schwann cells. I. Establishment of purified populations from cultures of peripheral nerve. *Brain Res.*, 1979. **165**: 105-118.
8. Podhajsky, R.J. and R.R. Myers, A diffusion-reaction model of nerve regeneration. *J. Neurosci. Meth.*, 1995. **60**: 79-88.
9. Canossa, M. et al., p75(Ngfr) and Trka receptors collaborate to rapidly activate a p75(Ngfr)-associated protein kinase. *EMBO J.*, 1996. **15**: 3369-3376.
10. Buettner, H. and R. Pittman, Quantitative effects of laminin concentration on neurite outgrowth *in vitro*. Dev. Biol., 1991. **145**: 266-276.

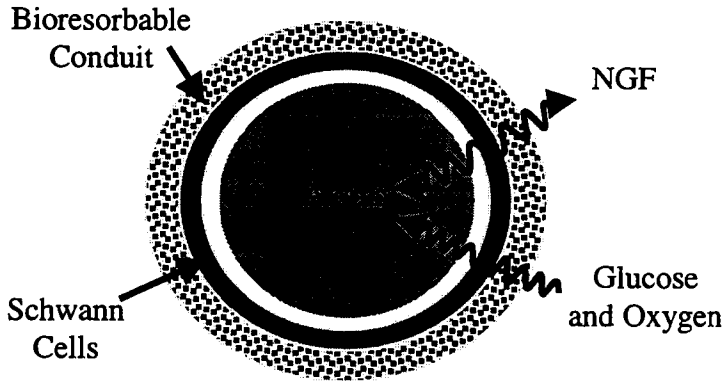

Figure 1: Schematic of bioartificial nerve graft.

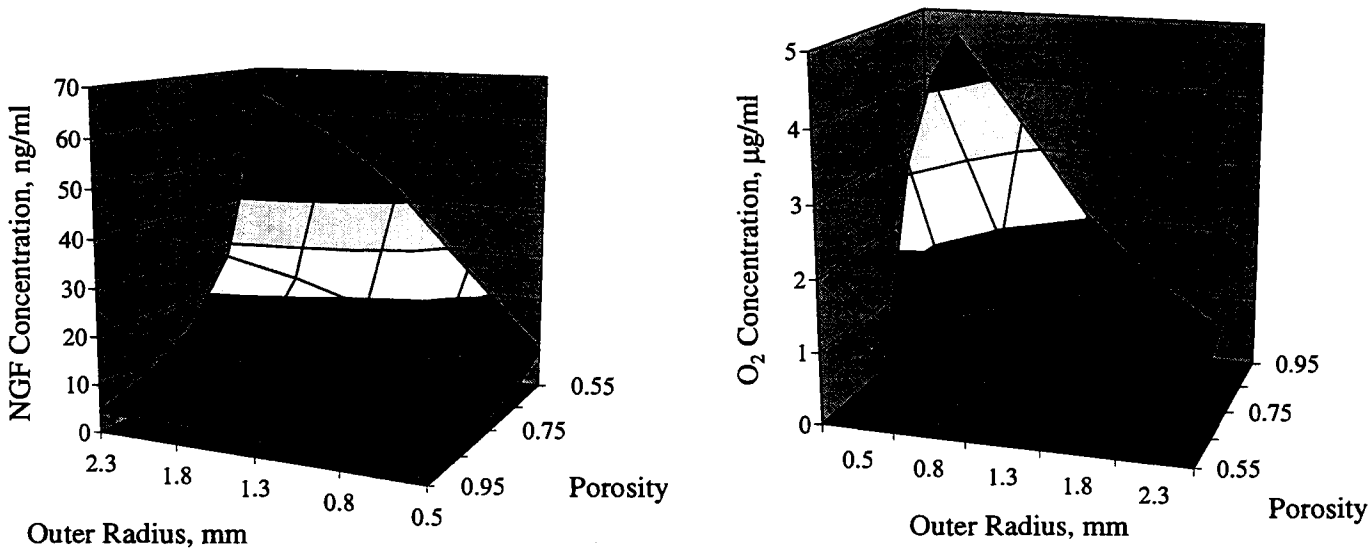

Figure 2: Model predictions of oxygen and NGF concentrations in lumen center.

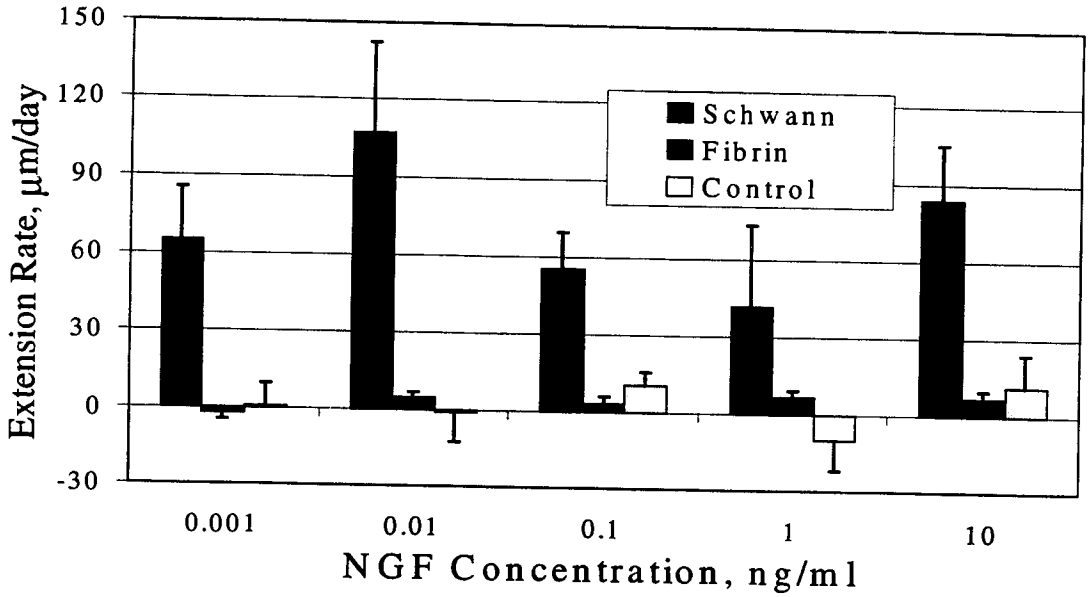

Figure 3 : Effect of NGF concentration on axon extension rate.

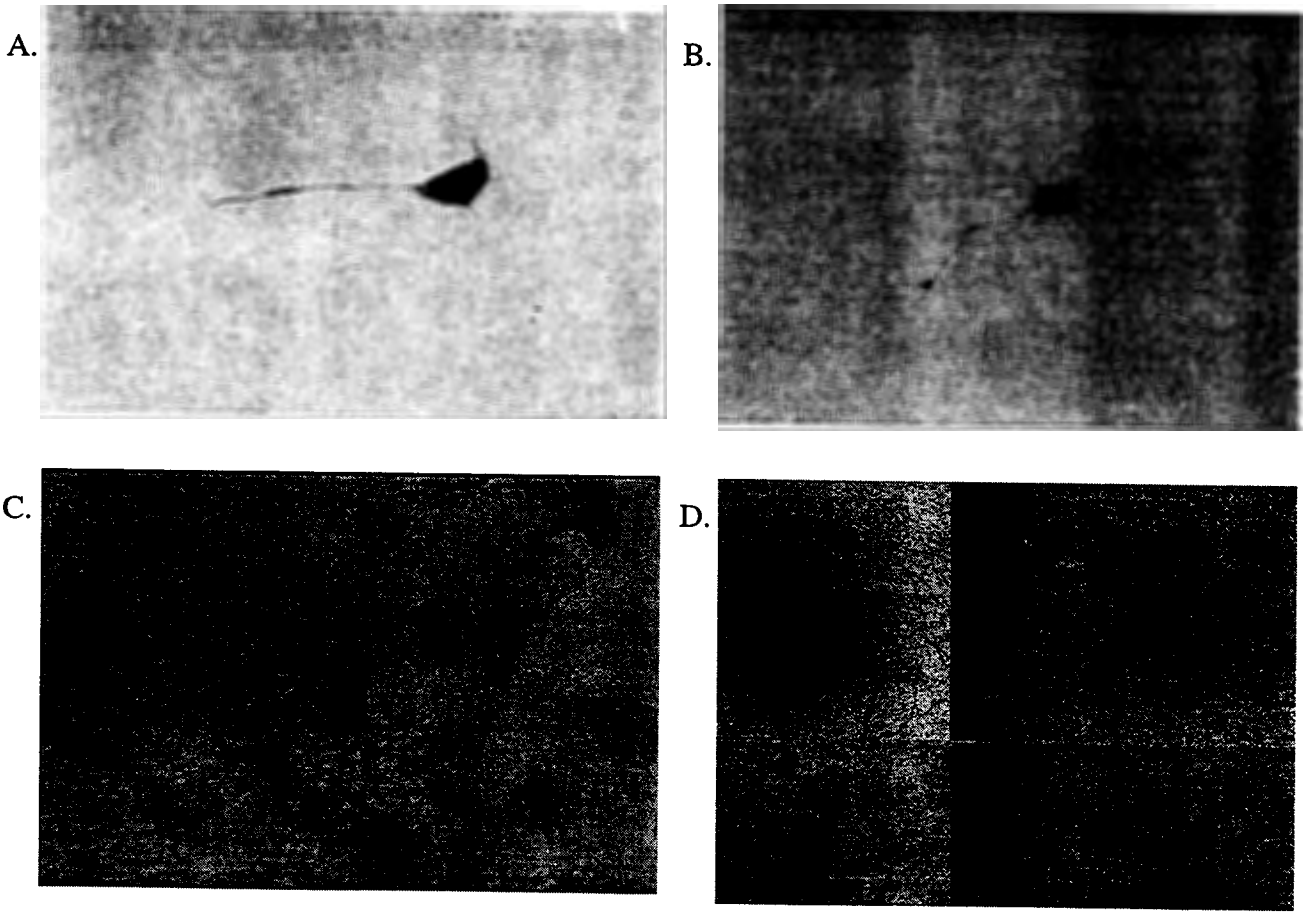

Figure 4: Sample images of neurons grown on various substrata. A) Fibrin substrate. Day 0. 400x. B) Fibrin substrate. Day 6. 200x. C) Schwann cell substrate. Day 3. 100x. D) Schwann cell substrate. Day 7. 40x.

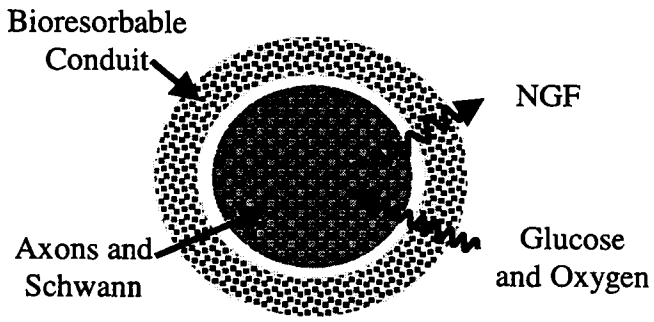

Figure 5 : Modified design for bioartificial nerve graft.

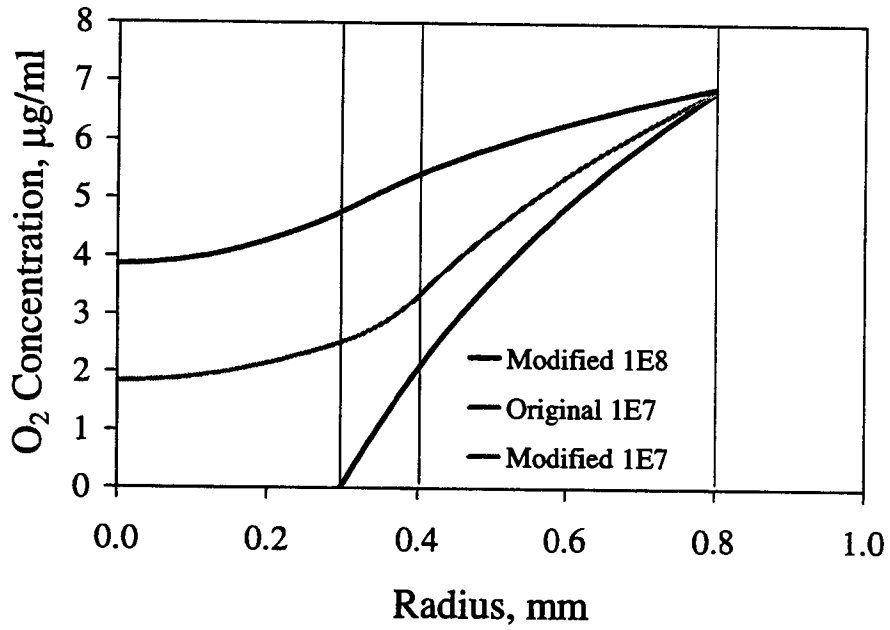

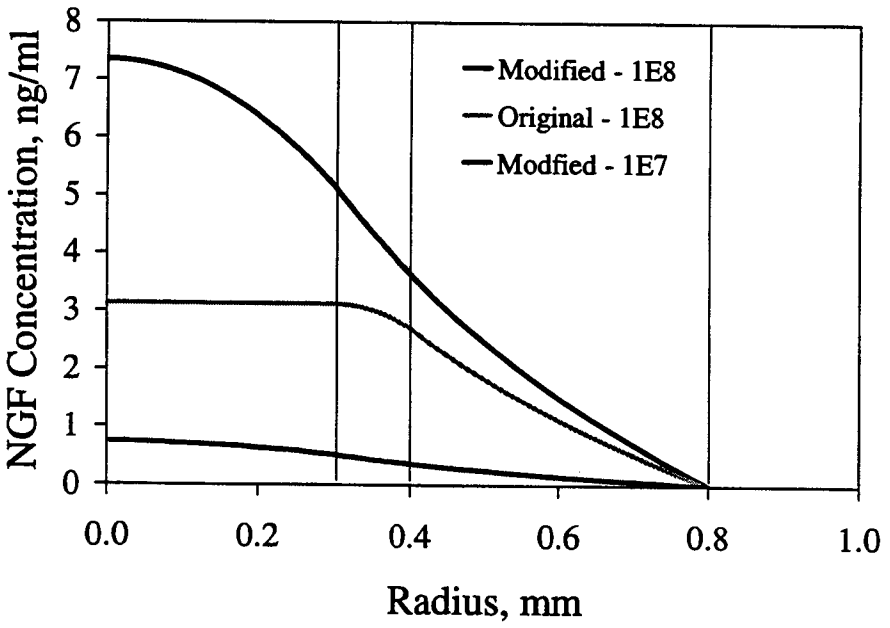

Figure 6: Model results for modified design and comparison to original design.

Effect of processing on the recovery of recombinant β-glucuronidase from transgenic canola

Y. Bai[1] and Z.L. Nikolov[1,2]
Departments of [1]Chemical Engineering and [2]Food Science and Human Nutrition
Iowa State University, Ames, IA 50011

Abstract

The feasibility of utilizing transgenic seed for production of foreign proteins was investigated by using β-glucuronidase (rGUS) synthesized in transgenic canola. The goal of this project is to set up a feasible, efficient and easy to scale-up bioprocess for recovering recombinant proteins from canola, and to further apply this method to other transgenic oilseeds.

Two kinds of seed processing methods (wet grinding and dry grinding) followed by protein extraction were compared. No significant difference of extractable enzyme activity between the two methods was observed as long as the final particle size was small enough. After centrifugation, the aqueous phase contained about 6% of the initial canola oil, the remaining oil being almost equally distributed between the insoluble solids and the cream phase. The thermostability experiments indicated that the transgenic canola seed containing rGUS could be stored at an ambient temperature for two weeks and for at least two months at 10°C without significant loss of enzyme activity. There about 30% of initial rGUS activity was lost after four days incubation of canola seed at 38°C, and 70% activity loss was detected after heating canola seed at 70°C for 2 h. Canola oil extraction with hexane at 66°C did not significantly affect the recovery of rGUS activity and total extractable protein.

Introduction

Transgenic plants are attracting attention as one of the most economical systems for large-scale production of proteins of potential pharmaceutical and industrial interest (Austin et al., 1994; Krebbers et al., 1992; Pen et al., 1993; Whitelam et al., 1993). Transgenic plants offer several unique advantages, such as low cost of growing plants on large acreage, the ease in scale-up, the availability of natural protein storage organs, and well-established practices for their efficient harvesting, transporting, storing, and processing. More than 20 different recombinant proteins have been expressed successfully in plant hosts, like tobacco, corn, and canola (Kusnadi et al., 1997). However, the current disadvantages of plants as "biofactories" are the low accumulation levels of recombinant proteins and insufficient data on downstream processing. For more general use of plants as recombinant protein production hosts, improvements in processing and purification strategies, which will allow economical separation of the recombinant proteins from endogenous plant proteins, will be required (Van Rooijen et al., 1995; Kusnadi et al., 1997).

Although plant transformation and protein expression have been extensively studied in recent years, most of the work focused on factors affecting protein expression and accumulation (Brown et al., 1995; Sullivan et al., 1993; Utsumi et al., 1993, 1994; Whitelam et al., 1993). Only a few publications that have addressed the processing of transgenic material and the recovery of expressed proteins (Hood et al., 1997; Kusnadi et al., 1998a,b). Our goal is to develop a feasible, efficient, and easy method to scale up downstream process for transgenic canola seed that could

be applied to a wide variety of recombinant protein products.

The traditional canola processing method is well established and consists of seed conditioning, cooking, flaking, oil pressing, and hexane extraction of pressed cake (Norris et al., 1982; Ward et al., 1984; Shahidi, 1990). To minimize the effect of temperature and shear on recombinant protein activity during cooking and oil pressing, we are investigating alternative processing routes (Figure 1). In this study, rGUS expressed in transgenic canola seed was used as a model protein to determine how processing conditions during seed drying, storing, conditioning, grinding, and oil extraction affect recombinant protein activity.

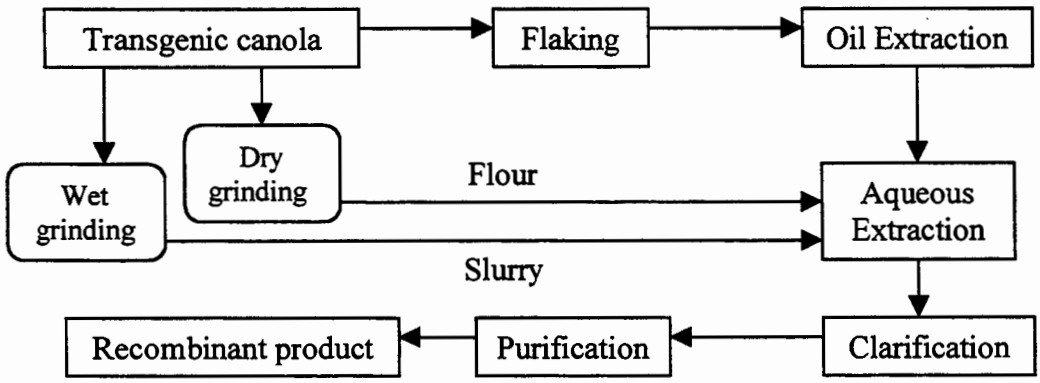

Fig. 1: Proposed process flow diagram for processing of canola

Materials and Methods

Processing and extraction methods

Dry grinding and extraction. Full-fat canola flour was prepared by grinding the whole seed with a high-speed flour mill (Magic Mill, Salt Lake City, Utah). One gram of canola flour was extracted with 10 ml of 50 mM NaP_i buffer of pH 7.5 (1:10 solid-to-liquid ratio). The suspension was shaken at room temperature in a Orbital Shaker (Labline, Melrose Park, Ill.) for 30 min at 250 rpm before centrifugation.

Wet grinding and extraction. Whole canola seed (1 g) was mixed with 10 ml of 50 mM NaP_i buffer of pH 7.5 and wet-ground with a laboratory homogenizer (Janke & Kunkel, Germany) at 17,000 rpm and 15°C for less than 1 min. The slurry was incubated at room temperature for 10 min without shaking before centrifugation.

The slurry prepared by either wet or dry-grinding process was first centrifuged (Beckman Model JA2-21 centrifuge, 11,000 rpm, 23°C) to remove insoluble solids. The supernatant was then filtered through a filter paper (Whatman No. 4) to remove the light oil-rich fraction (cream).

rGUS activity (Jefferson et al. 1991) and total soluble protein (Bio-Rad Coomassie Plus Protein Assay) in the clarified aqueous extract was determined according to the cited standard protocols. All experiments were performed in duplicate.

Oil distribution in the aqueous extracts

Canola seed with determined initial moisture (MC) and oil contents (Method 14-084 and 14-085, AOAC 1984) was processed and extracted as before. After centrifugation, the aqueous slurry was fractionated into spent solids, clarified aqueous, and cream phase. The cream phase consisted of a thin layer floating on the top of the liquid phase. The clarified aqueous phase was obtained by filtering the solids and the cream through a Whatman No. 4 filter paper. In a parallel experiment, the cream was removed carefully by a spatula, and then the solids were separated by filtration. The oil content of the whole seed, spent solids, and the mixture of spent solids and the cream were measured and labeled as O, Os, and Om, respectively. The amount of oil in the aqueous phase, labeled as O_{aq}, was calculated from the oil balance (O_{aq} = O - Om) because of the lack of an accurate method to determine the oil content in the liquid phase. The oil content of the cream phase (Oc) was also estimated from the oil balance (Oc = Om - Os).

Storage and heat stability

Two grams of whole canola seed (12% MC) were weighed into 10-ml scintillation vials with foil-lined caps. Closed vials were incubated at five different temperatures (10, 23, 38, 70 and 100°C) for up to 60 days. Three 2-g samples for each incubation temperature were taken out at a specified time and extracted with 20 ml of 50 mM NaP_i (pH 7.5) buffer. The extraction was performed as before (homogenization at 17,000 rpm), and rGUS activity and total soluble protein in the extracts were determined.

To determine the effect of the seed MC on storage and heat stability of rGUS, the initial MC of canola seed was reduced by desiccation in a drykeeper (Santo Co., Japan). After 2 h incubation in the drykeeper, the MC was decreased from 12% to 9%. Thermostability of canola flake was also studied following the same procedures except that heating was performed only at 70°C.

Hexane extraction studies

Transgenic canola (12% MC) preconditioned at 38°C for 30 min was flaked through a 0.012-in gap flaking rolls (Model K, Roskamp Inc., Waterloo, Ia.) and then aspirated (Model CFZ1, Carter-Day Co., Minneapolis, Minn.) to remove the hull. A portion of canola flakes was saved to determine MC, oil content, extractable rGUS activity, and total protein. The rest of the flakes were divided into 150-g batches and extracted with hexane at room temperature and 66°C in a laboratory batch extractor. The hexane extraction with 1:3 solids-to-solvent ratio was performed in six stages, mimicking industrial cross-current operation. Each extraction stage lasted 6 min with 3 min drainage between the stages. The defatted canola flakes (meal) were air-dried overnight to remove the residual hexane. The moisture and oil content of the defatted meal was measured and expressed on a wet basis. rGUS activity and total protein concentration in the aqueous extracts prepared by the wet-grinding were calculated on a fat-free dry solids base.

Results and Discussion

Comparison of processing and extraction methods

The rGUS and total protein extraction yields of dry and wet-ground transgenic canola are

compared in Table 1.

Table 1: Effect of processing and extraction on rGUS and protein extraction

Sample	Processing method	Extraction method	rGUS activity (U/g)*	Total protein (mg/g)*
Full-fat	Dry grinding	Rotary shaker	1129	106
Full-fat	Wet grinding	Not shaken	1078	102
Defatted	Dry grinding	Rotary shaker	983	94
Defatted	Wet grinding	Not shaken	957	93

*Based on fat-free dry solids

The data suggest that neither the processing method nor the sample oil content substantially affected protein extraction. The high-oil content of the initial material (40%) did not interfere with the rGUS and protein extraction. The lower protein and activity yields obtained by using defatted canola are within the range of experimental error (±5%). There is no obvious advantage of either processing method. Dry grinding of full-fat canola on a large scale may be difficult due to high oil content. The wet grinding is a shorter procedure because it combines grinding and aqueous extraction steps. Most of the protein extraction occurred during the grinding step. The resting time, ranging from 5 to 25 min, did not make any difference on the extraction efficiency (data not shown). To compare and standardize the extraction parameters, we used 10 min incubation (resting) in all the experiments. Oil emulsification (formation of a cream phase) and subsequent recovery of the oil from the cream phase is a potential disadvantage of the wet-grinding method. Both processing methods need further investigation.

Oil distribution after aqueous extraction

Canola seed is notorious for its extremely high oil content (around 40%), and the oil remaining in the aqueous phase after centrifugation would be harmful to subsequent protein purification steps such as membrane filtration and chromatography. The oil content of spent solids, the cream, and clarified aqueous phase is summarized in Figure 2. The oil distribution in the samples proc-

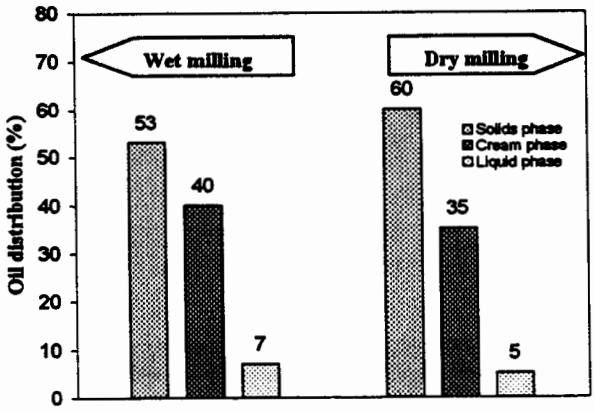

Fig. 2: Oil distribution in solids, cream and liquid phase after aqueous extraction

the initial seed oil, was distributed between spent solids (53 and 60%) and the cream phase (40 and 35%), respectively. Clarified extracts contained the remaining 5-7% oil, which amounted to an oil concentration of approximately 0.3% (w/v). Although we do not know what is the oil concentration in the aqueous phase that will cause fouling of membranes and chromatographic resins, the latter number is rather small and the possibility of loading clarified extract directly onto a chromatographic column is worth considering.

Storage and heat stability

Storage and heat stability of recombinant protein are important parameters because transgenic canola seeds may be subjected to different temperatures and incubation times during conditioning (38°C), solvent extraction (60-66°C), and meal desolventizing (103-107°C).

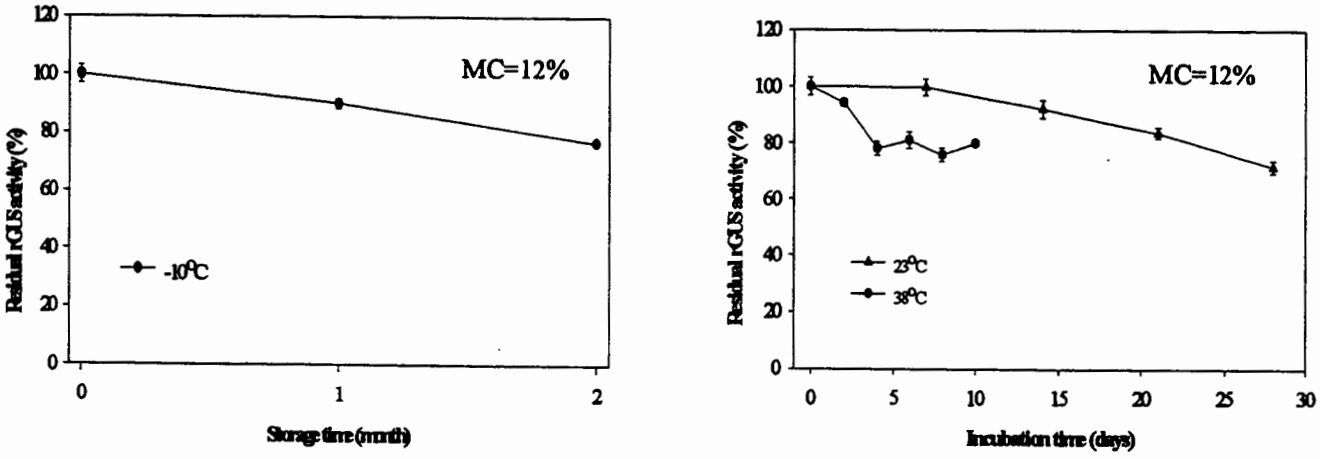

Fig. 3: Storage stability of rGUS in whole canola seed

Storage stability of rGUS activity at different temperatures is reported in Figure 3. The enzyme was fairly stable at 10°C during a two-month incubation. At room temperature, about 30% of the initial rGUS activity were lost after four weeks. At 38°C, about 20% rGUS activity was lost in the first four days; and after that, the activity remained constant. The stabilizing effect was ascribed to the loss of moisture during incubation. The seed MC dropped from 12% to 9 % after 10 days of incubation at 38°C. The data suggest that transgenic seed could be stored at 10°C for long time periods and at room temperature for about two weeks. Based on rGUS stability data in transgenic corn (Kusnadi et al., 1998a), rGUS seemed more stable in corn than in canola. The enzyme was very unstable when heated at 70°C and 100°C (Figure 4). About 30% of initial enzyme activity was lost after 2 h at 70°C. No residual activity was detected after 4 h at 70°C and after 5 min at 100°C. The final MC in both cases was 10%.

To determine the effect of initial moisture content on enzyme activity, whole canola seed and canola flakes were exposed to 70°C for up to 10 h (Figure 5). Decreasing the initial MC of the whole seed from 12 % to 9% improved the enzyme thermostability, but not as much as reducing the MC to 6%. After heating canola flakes (6% initial MC) for 2 and 4 h, more than 60% and 55% of residual rGUS was measured, respectively.

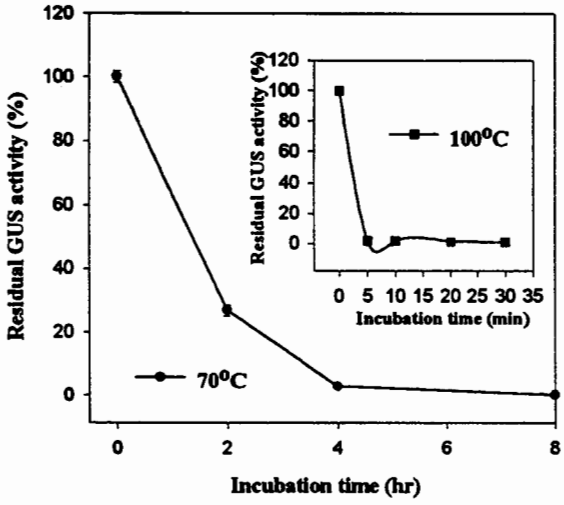

Fig. 4: Heat stability of rGUS in whole canola seed at initial MC of 12%

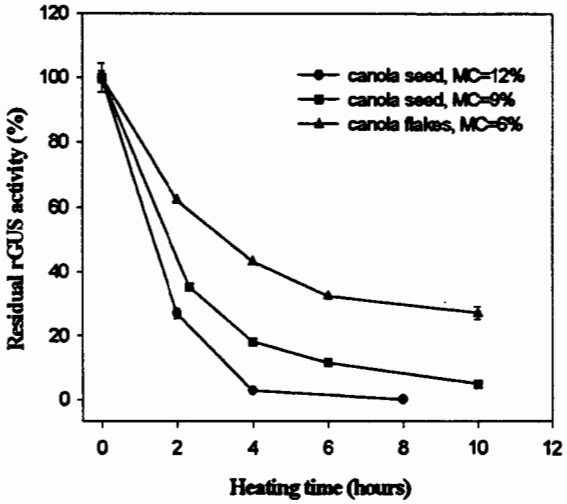

Fig. 5: Effect of initial MC on enzyme stability at 70°C

Hexane extraction

Several oil extraction methods are used in the oilseed industry. If the oil content is lower than 20%, usually direct solvent extraction is used. For greater than 20% oil content, a combination of screw pressing and solvent extraction usually gives best oil recoveries (Salunkhe et al., 1992; Shahidi, 1990). Because screw pressing generates temperatures above 100°C (Ward, 1982), in this study we used hexane extraction without prepressing. The objective was to determine the effect of direct hexane extraction on oil recovery and rGUS activity (Figure 6).

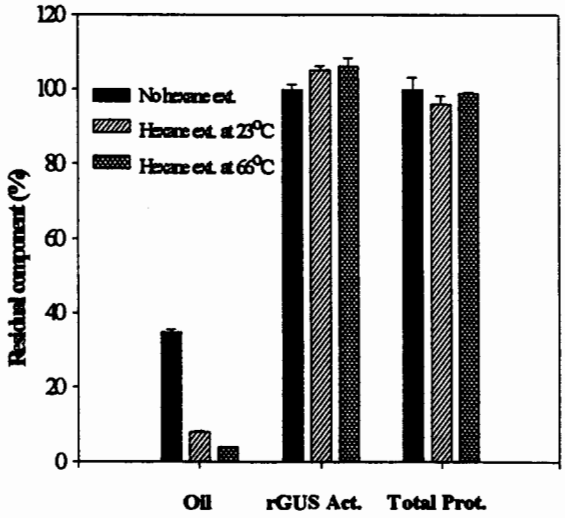

Fig. 6: Effect of hexane extraction and extraction temperature on residual oil, rGUS activity and total protein in canola flake

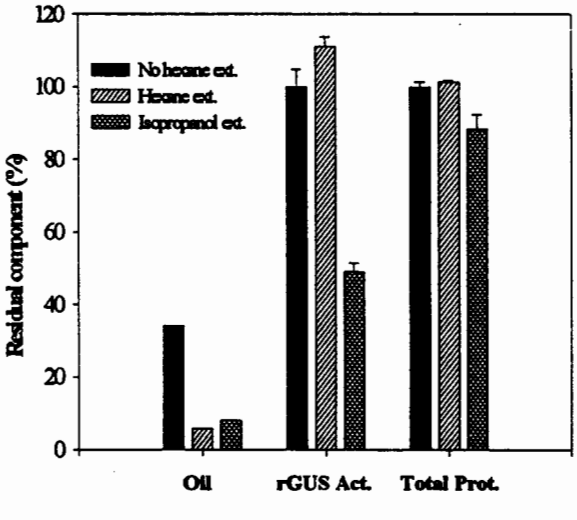

Fig. 7: Effect of polar, nonpolar solvent extraction on residual oil, rGUS activity and total protein in canola flake (all extractions were taken at 66°C)

The data in Figure 6 show that recombinant enzyme was stable in the presence of hexane at room temperature and 66°C. The extractability of canola proteins was not affected either. Compared with the 40% activity loss measured in the air-exposed samples for 1 h at 70°C (Figure 5), the presence of hexane presence stabilized the process. To confirm that hydrophobic hexane contributed to the increased thermostability of rGUS, we compared isopropanol (more polar solvent) and hexane extraction of canola flakes for 1 h at 66°C (Figure 7). There about 50% rGUS activity was lost after 1-h extraction with isopropanol and none with hexane. Total protein extractability with isopropanol decreased by 10%. The results suggest that a more hydrophobic solvent is a better choice for oil removal prior to recombinant protein extraction. The apparent thermostabilization effect of hydrophobic organic solvents has been observed and exploited in enzyme catalysis (Dordick, 1989; Klibanov, 1989; Lu et al., 1992).

The oil recovery by using direct hexane extraction was not as efficient as the commercial process (Salumkhe, 1991). There was 8% and 4% oil left in the meal at the end of extraction at room temperature and 66°C, respectively. Because our major goal is to maximize the recovery of recombinant enzyme activity, a 3-4% oil loss could be acceptable even on a commercial scale.

Acknowledgments

We want to thank ProdiGene Inc. and Pioneer Hi-Bred International Inc. for supplying the transgenic canola seed. We also thank Dr. Kusnadi for suggestions and help. This research was partly supported by grants from USDA/NRI and NSF.

References

Austin, S., Bingham, E.T., Koegel, R.G., Mathews, D.E., Shahan, M.N., Sranb, R.J., Burgess, R.R. 1994. An overview of a feasibility study for the production of industrial enzymes in transgenic alfalfa. Ann. N.Y. Acad. Sci. 721:235-244.

Brown, S.M., Santino, C.G. 1995. Enhanced expression in plants, U.S. Patent 5,424,412.

Dordick, J.S. 1989. Enzymatic catalysis in monophasic organic solvents. Enzyme Microb. Technol. 11:194-211.

Hood, E.E., Witcher, D.R. et al. 1997. Commercial production of avidin from transgenic maize: Characterization of transformant, production, processing, extraction and purification. Molec. Breeding. 3:291-296.

Jefferson, R.A., Wilson, K.J. 1991. The GUS gene fusion system, pp.1-33. In: S.B.Gelven, R.A. Schilperoort, and D.P.S. Verma (eds.), Plant Molecular Biology Manual, Vol. 1, B14. Kluwer, Dordrecht, Netherlands.

Klibanov, A.M. 1989. Enzymatic catalysis in anhydrous organic solvents. TIBS 14, April.

Kusnadi, A.R., Nikolov, Z.L., Howard, J.A. 1997. Production of recombinant proteins in transgenic plants: Practical considerations. Biotechnol. Bioeng. 56:473-484.

Kusnadi, A.R., Evangelista, R.L., Hood, E.E., Derrick, R.W., Howard, J.A., Nikolov, Z.L. 1998a. Processing of transgenic corn seed and its effect on the recovery of recombinant β-glucuronidase. Biotechnol. Bioeng. 60:44-52.

Kusnadi, A.R., Hood, E.E., Derrick, R.W., Howard, J.A., Nikolov, Z.L. 1998b. Production and purification of two recombinant proteins from transgenic corn. Biotechnol. Prog. 14:149-155.

Lu, A.S., Dordick, J.S. 1992. Organic solvents strip water off enzymes. Biotechnol. Bioeng. 39:392-397.

Norris, F.A. 1982. Extraction of fats and oils, In: Bailey's Industrial Oil and Fat Products, 4th ed., D. Swern, ed. New York: Wiley. 2:207-214.

Pen, J., Sijmons, P.C., van Ooijen, A.J.J., Hoekema, A. 1993. Protein production in transgenic crops: Analysis of plant molecular farming. pp.239-251. In: A. Hiatt (ed.), Transgenic Plants: Fundamentals and Applications. Marcel Dekker, New York.

Shahidi, F. 1990. Canola and Rapeseed: Production, Chemistry, Nutrition and Processing Technology. pp. 235-249. Van Nostrand Reinhold, New York.

Salunkhe, D.K., Chavan, J.K., Adsule, R.N., Kadam, S.S. 1991. World Oil Seeds: Chemistry, Technology, and Utilization. pp. 81-83. Van Nostrand Reinhold, New York.

Sullivan, M.L., Green, P.J. 1993. Post-transcriptional regulation of nuclear-encoded genes in higher plants: The roles of mRNA stability and translation. Plant Mol. Biol. 23:1091-1104.

Utsumi, S., Kitagama, S., Katsube, T., Higasa, T., Kito, M., Takaiwa, F., Ishige, T. 1994. Expression and accumulation of normal and modified soybean glycinins in potato tubers. Plant Sci. 102:181-188.

Utsumi, S., Kitagama, S., Katsube, T., Kang, I.J., Gidamis, A.B.,T., Takaiwa, F., Kito, M.1993. Synthesis, processing and accumulation of modified glycinins of soybean in the seeds, leaves and stems of transgenic tobacco. Plant Sci. 92:191-202.

Van Rooijen, G.J.H., Moloney, M.M. 1995. Plant seed oil-bodies as carriers for foreign proteins. Bio/Technology 13:72-77.

Ward, J.A. 1984. Pre-pressing of oil from rapeseed and sunflower. J. Am. Oil Chem. Soc. 61:1358-1361.

Whitelam, G.C., Cockburn, B., Gandecha, A.R., Owen, M.R.L. 1993. Heterologous protein production in transgenic plants. Biotechnol. Genet. Eng. Rev. 11:1-29.

Size Classification of an Iron-Carbon Magnetic Particulate for a Localized Drug Delivery System

Ryan P. Cooper, Melinda Roskos, John F. Doyle, Teresa Longin, Kelly Rakes, and Paul Todd, Department of Chemical Engineering, University of Colorado, Boulder, CO 80303

Abstract

An iron-carbon magnetic particulate will be used to investigate delivery of chemotherapeutic drugs to tumor sites. The complex will be administered intra-arterially upstream near the tumor site. It will flow through the arteries until it is drawn by a magnet situated to capture the drug complex and keep the complex within or near the tumor. The particles should be small enough to flow freely through a capillary bed, yet have sufficient magnetophoretic mobility to be captured by the magnet. Analytical and preparative methods are therefore needed to produce and characterize particle populations meeting these requirements. The purpose of this work is to explore experimental techniques for size classification of these particles. An inclined settler is employed to fractionate the particles according to size. The magnetophoretic mobility of the particulate is characterized by graded magnetic capture of the particles. The two methods, inclined sedimentation and graded magnetic capture, have been explored to produce uniform particles.

1. Introduction

1.1 Background

FeRx, Inc. is developing an iron-carbon composite particle, Magnetically Targeted Carrier (MTC), for drug delivery. The size distribution of the MTC particles is 1-5 μm in diameter. The MTC/drug complex will be administered intra-arterially upstream near the tumor site. It will flow through the arteries until it is drawn by a magnet, which is situated to capture the drug complex, into the capillary bed near the tumor site, where the complex will be kept to allow the drug to be desorbed from the MTC. Therefore, the particles should be small enough to flow freely into a capillary bed, yet have sufficient magnetophoretic mobility to be captured by the magnet. The USP allows less than 600 particles per dose larger than 25 μm, and less than 6000 particles per dose larger than 10 μm, a specification for parenteral drugs. The lower limit on the small particulate is based on the condition that it must have a large enough magnetophoretic mobility to be drawn to a magnet *in vivo*.

1.2 Objectives

The two main objectives of this project were

1. To perform graded magnetic capture experiments to separate particles based on magnetophoretic mobility.
2. To perform inclined sedimentation experiments to enrich for particles greater than 10 μm.

2. Graded Magnetic Capture

2.1 Experimental design and theory

The experimental design focuses on applications of the concept of *magnetophoretic mobility.* Other research groups have studied the levitation of magnetically labeled biological cells in a magnetic field (Winoto-Morbach 1994, Zborowski 1995, Yiacoumi 1996). The force balance on a single particle or complex in a levitating magnetic field, in one dimension, is

$$m\frac{d^2z}{dt^2} = -F_m - F_d + F_g - F_b \qquad 1)$$

where F_m is the magnetic force imparted on the particle by an applied magnetic field, F_d is the drag force of the fluid on the particle, assuming Stokes' flow, F_g is the gravitational force on the particle, and F_b is the buoyant force of the fluid acting on the particle. Assuming steady state in the force balance above, the velocity of a spherical particle due to a levitating magnetic field becomes

$$v_m = \frac{d^2\Delta\chi}{18\eta\mu_0} B\frac{dB}{dz} \qquad 2)$$

where d is the diameter, $\Delta\chi$ is the volumetric magnetic susceptibility relative to the surrounding medium, η is the viscosity of the solvent, μ_0 is the magnetic permeability of free space, and B is the magnetic field strength. The definition of a mobility is a velocity divided by the driving force. For a particle being levitated in a magnetic field, the magnetophoretic mobility (μ_m) is defined as

$$\mu_m \equiv \frac{v_m}{B \bullet \frac{dB}{dz}} \qquad 3)$$

From Equations 2 and 3, magnetophoretic mobility may also be represented by

$$\mu_m = \frac{d^2\Delta\chi}{18\eta\mu_0} \qquad 4)$$

With Equation 4, it can be seen that for a given particle, the magnetophoretic mobility is a function of particle and media properties. In the case of ferromagnetic particles, magnetophoretic mobility is also a function of B, because $\Delta\chi$ is a function of the applied magnetic field strength.

2.2 Magnetic separation experiments

For experiments involving μ_m to be consistent for each stage, all the particles must start from a common point, some distance from a permanent magnet. In the design of the experiments, particles in the sample cuvette have a common starting position, some known distance from the inter-

face of the collection cuvettes. A permanent magnet is placed above the suspension of particles and allowed to capture particles for a specified amount of time (30 s, 1, 2, 3 ...min). After the dwell time has been reached, the collection cuvette is displaced from the sample cuvette, and another stage is started. At first, low magnetic field strengths are used to capture particles with large magnetophoretic mobilities. Each subsequent magnet has a higher magnetic field strength to allow for progressively smaller magnetophoretic-mobility particles to be captured. The freedom to vary both magnetic field strength and dwell time for each capture magnet facilitates separation.

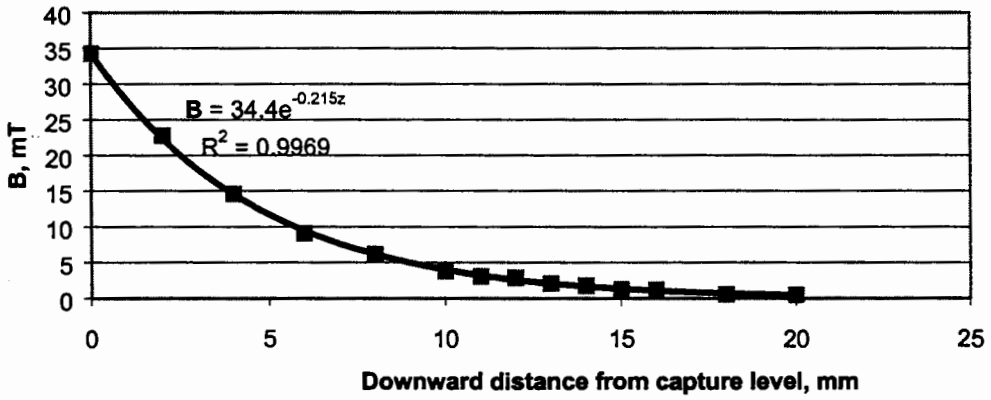

Figure 1: Magnetic field map for an 85-mT magnet.

To calculate magnetophoretic mobility for a desired step using Equation 3, the magnetic field and its gradient must be found; therefore, the field map for each magnet must be determined. In the case of an 85-mT magnet, the field map is shown in Figure 1. The fitted empirical equation, found by using the trendline command in Excel, for magnetic field strength, B, is

$$B = 34.4e^{-0.215z} \qquad 5)$$

where z is the distance from the top of the cavity. The velocity is a function of B, and will not be constant over the distance the particles travel. Therefore, $(B \bullet dB/dz)^{-1}$ must be integrated over the distance the particles traveled, and the time it took them to travel, the dwell time. The magnetophoretic mobility for the 85-mT case, using a dwell time of 60 s, can now be determined. The particles starting position was at z = 10.5 mm, and the level at which they are captured is z = 3.5 mm; therefore these become the distance integaration limits. Therefore, the magnetophoretic mobility becomes

$$\mu_m = 39.6 \text{ mm}^2/\text{mT}^2\text{-s}$$

A graded series of magnetic captures was performed using polyethylene glycol (PEG-400), with a viscosity of 106.9 cP, as the solvent, and the capture magnet field strengths were seq-

uenced for characterization of MTC is as follows:

Stage	Capture magnet field strength (mT)	Dwell time (s)
1	57	180
2	85	60
3	89	180
4	89	60
5	90	60
6	91	180
7	93	60
8	102	60
9	107	180

The resulting particle counts for each stage are given in Figure 2. The first capture step had very few particles, and the size distribution of the particles was very similar to that of the starting material. Therefore, it was determined that the magnet was too weak to capture particles. Step 4 was chosen to show that particles with a magnetophoretic mobility above this cut-off were actually all captured at step 3. The results in Figure 2 do in fact show that step 4 captured very few particles. Another result, also seen in Figure 2, is the high number of particles found in the residual, which did not get captured at any field strength. This group of particles, at least 40 % of the total, did not get classified, and were the smallest.

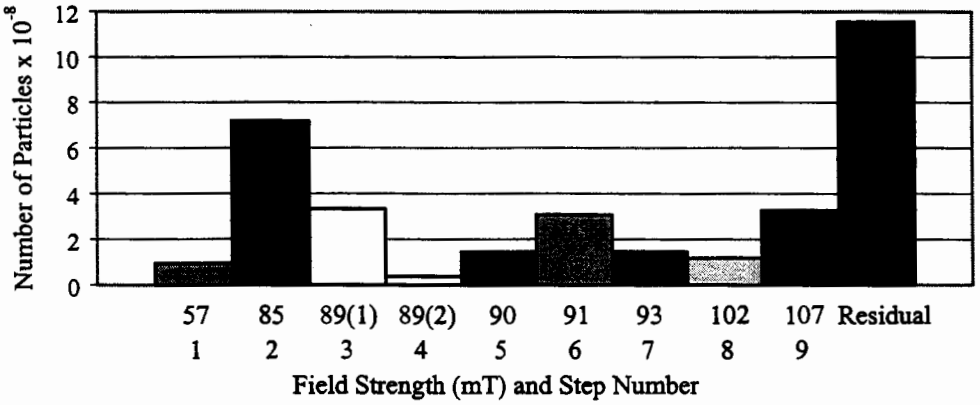

Figure 2: Number of particles found in each stage by counting particles in a hemacytometer.

As can be seen in Equation 4, magnetophoretic mobility can be used to classify particles based on diameter, especially if $\Delta\chi$ is the same for all particles. Particle sizes from each collection were determined at FeRx, using a Model 770 AccuSizer from Particle Sizing Systems, Inc. Figure 3 shows the diameter at which 95% of the particles in the collection have a smaller diameter for selected fractions. It can be seen that low magnetic field strengths captured large particles, whereas high magnetic field strengths capture the smaller particles. This is in concurrence with Equation 4 for magnetophoretic mobility.

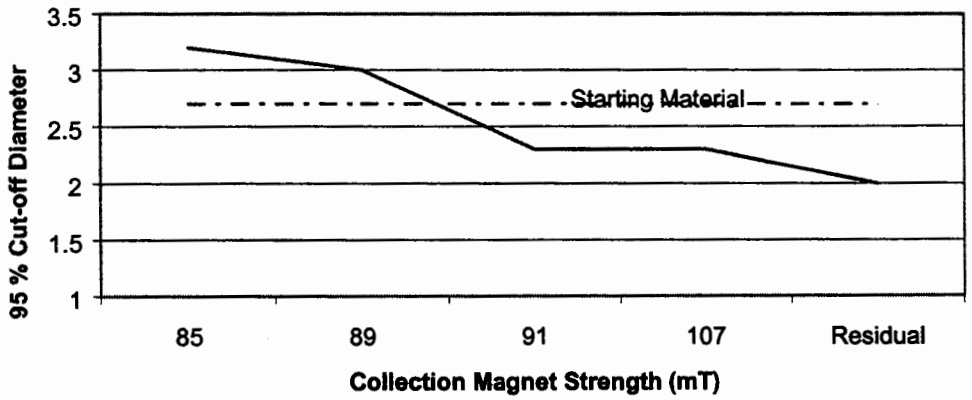

Figure 3: Cut-off diameter for which 95% of the MTC particles have a smaller diameter.

From graded magnetic capture experiments, it has been determined that MTC particles can be classified by magnetophoretic mobility. This classification can be done with graded magnetic capture as a validation technique, but could not be easily scaled up to become a down-stream separation technique because the use of magnets causes significant aggregation in the particles and leaves them with undesired remaining magnetization.

3. Inclined Sedimentation

3.1 Inclined settler design and theory

Inclined sedimentation is governed by three equations: a sedimentation rate, a velocity equation derived from Stokes' Law, and a mass balance. The sedimentation rate of particles in an inclined setter is (Davis 1989)

$$S(v) = vw(L\sin\Theta + b\cos\Theta) \qquad 6)$$

where $S(v)$ is the volume of the suspension cleared of particles with velocity v per unit time, v is the particle sedimentation velocity, w is the width of the channel in the settler, L is the length of the channel, b is the thickness of the settler, and Θ is the angle of inclination from the vertical. The sedimentation velocity, for spherical particles, is related to the size distribution of the particles using Stokes' Law

$$v = \frac{d^2(\rho_p - \rho_s)g}{18\eta} \qquad 7)$$

where d is the diameter of the particle, ρ_p is the density of the particle, ρ_s is the density of the solvent, and η is the viscosity of the solvent. The mass balance on the flow rates is

$$Q_f = Q_o + Q_u \qquad 8)$$

where Q_f is the flow rate of the feed; Q_o, of the overflow; and Q_u, of the underflow. The sedi-

mentation rate is related to the mass balance in the following equation:

$$S(v) = Q_o \qquad 9)$$

An inclined settler was constructed to apply the above relation to separating particles according to diameter size. Experimentation focused extensively on separating particles of 10 μm in diameter and greater from an initial feed. The apparatus, shown in Figure 4, and procedures evolved as better techniques were discovered and developed.

The particles obtained from FeRx are a composite of iron and carbon (75 weight % iron and 25 weight % carbon). The closed vial containing the particles was stored in ambient open air, but eventually particle aggregation was observed. The vial is now stored in a desiccant jar to prevent aggregation.

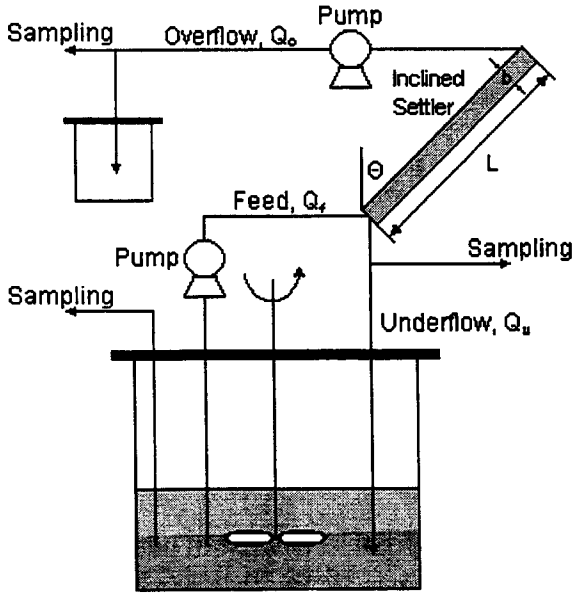

Figure 4: Schematic diagram of the inclined settler showing variables used in Equations 5-8.

In earlier experiments, the density of the particles was assumed to be 4.41 g/cm^3. This value is from a mass balance. Assuming a basis of 100 g, 75 g are iron and 25 g are carbon. From the known densities of iron and carbon, the total volume is determined. (The density of iron is 7.86 g/cm^3 and the density of amorphous carbon is between 1.8 and 2.1 g/cm^3—assume an average value of 1.9 g/cm^3.) The density is the quotient of the basis divided by the total volume. Later, other FeRx particles with a known measured average density of 4.198 g/cm^3 were used.

The solvent is a combination of polyethylene glycol-400 (PEG-400) and ethanol. The PEG-400 enhances particle suspension and hinders particle aggregation. In earlier experiments, the ratio of PEG-400 to ethanol was three to one. Later, the ratio changed to one to one.

The initial feed consists of 500 mL solvent and approximately 1 g of FeRx particles. The concentration of the feed was experimentally determined to be 7.6×10^7 particles/mL. The total number of particles in the initial feed is thus typically 3.8×10^{10}.

The flow rates were measured with a graduated cylinder and a stopwatch. An Excel spreadsheet was developed for calculating the overflow rate Q_o, typically 0.4 mL/s for this settler, from the sedimentation rate, v. The overflow pump was set at the desired Q_o volumetric flow rate. The underflow pump was then set at a flow rate one-tenth that of the overflow. Due to the slow flow rates, the accuracy of the pumps is limited. The actual ratio between the overflow and the underflow ranges from 2 to 10.

The experiments were run with the underflow recycled to the feed until the overflow became clear. It is important to note that the overflow still contains fine carbon particles, preventing the fluid from ever being truly clear. As the feed was being depleted by the overflow, solvent was added to the feed—"diasedimentation."

Six samples are taken throughout the experiment: an initial feed, initial overflow, and initial underflow at the beginning of steady state and a final feed, final overflow, and final underflow at the end of separation. Thus, after mixing the feed and the FeRx particles, the feed is sampled using a pipette. Once the overflow and underflow ratio at steady state is established, samples of both are taken. The tubing is placed in the sample vial. The last three samples are taken at the end of the experiment in the same manner as described above.

Particle sizes were determined using the PSS AccuSizer. The AccuSizer measures about 200,000 particles per sample and does not measure sizes below 0.5 μm. Samples were collected from the inclined settler and analyzed at FeRx the same day.

3.2 Inclined sedimentation experiments

Data from each experiment are presented in three graphs: one comparing the cumulative volume distributions of particles in the initial feed, initial overflow and initial underflow (Figure 5); another comparing the initial feed, final overflow, and final underflow (Figure 6); and a third comparing the initial feed and final feed (Figure 7). The relationship among the curves of the initial feed, initial overflow, and initial underflow agrees with theory. The overflow is more enriched in smaller particles than the feed. The underflow is more enriched in larger particles than the feed. The overflow contains practically no particles greater than 10 μm, consistent with the choice of Θ and Q_o.

In Figure 6, the overflow and underflow are more enriched in smaller and larger particles, respectively. Comparing the maximum particle size in the initial overflow to that in the final overflow, a shift from approximately 10 μm to 11 μm is observed. The purpose of the inclined sedimentation is to separate particles greater than 10 μm in diameter from particles less than 10 μm in diameter.

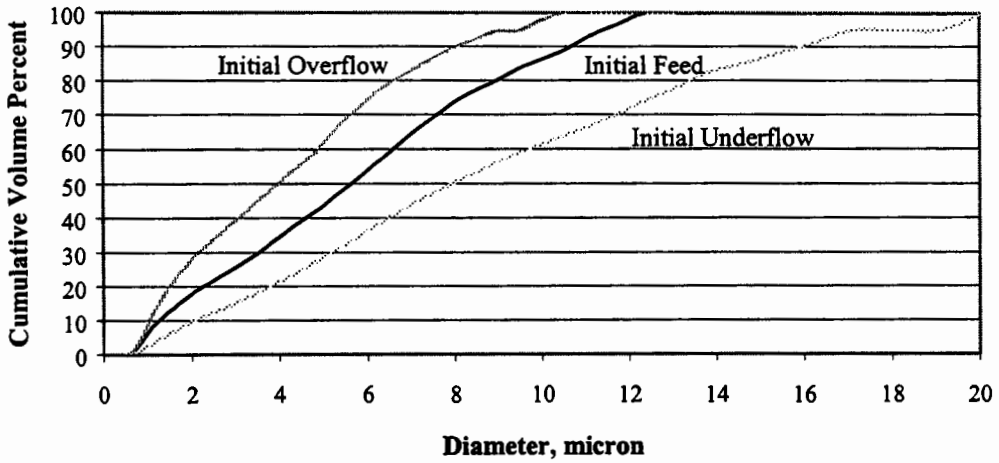

Figure 5: Cumulative volume distributions of particles in the initial feed, initial overflow, and initial underflow.

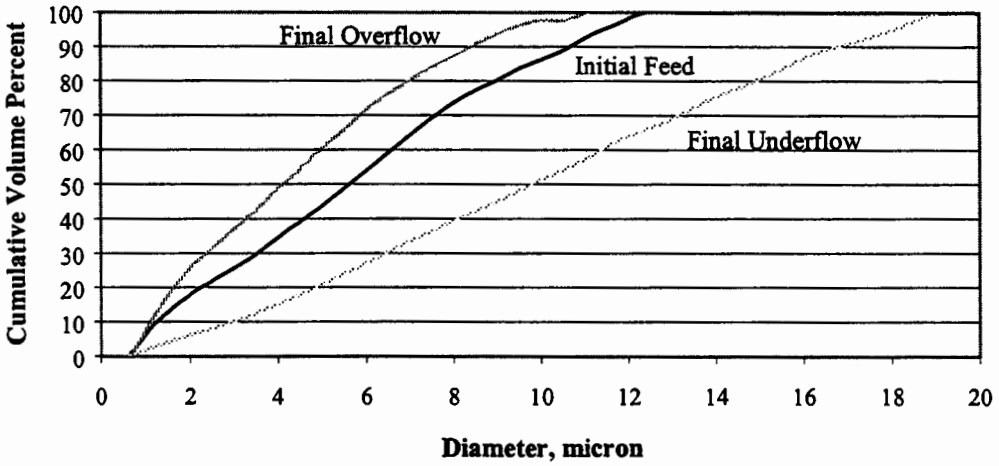

Figure 6: Cumulative volume distributions of particles in the initial feed, final overflow, and final underflow.

In Figure 7, the size distribution of the initial feed particles is compared to that of the final feed. The final feed is more enriched in larger particles than the initial feed. As the experiment progresses, the smaller particles are collected in the overflow while the larger particles are recycled to the feed container.

In summary, the final feed in the settler operations to date contains, typically, a 5-to 10-fold enrichment in particles greater than 10 μm, with the final number percent lying in the range 0.1 to 0.2%. This is a large percentage, and it implies that the original suspension contained around 0.01 to 0.02% particles greater than 10 μm.

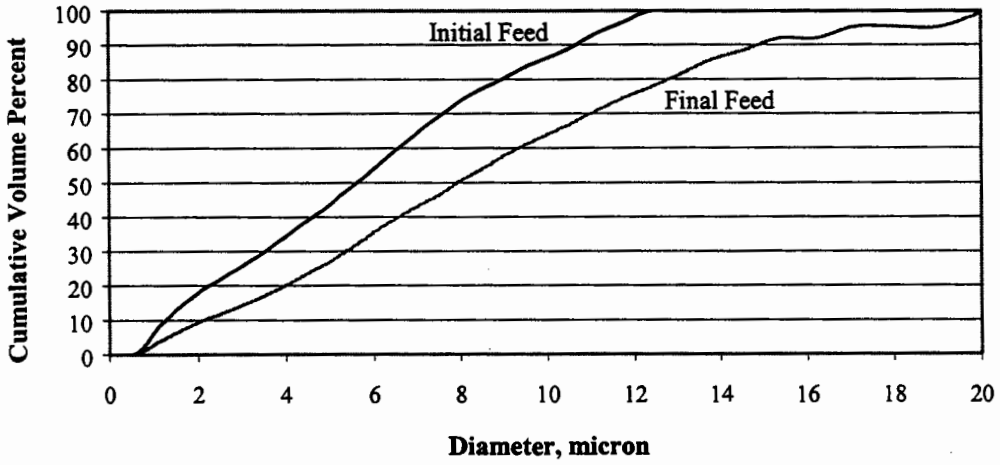

Figure 7: Cumulative volume distribution of particles in the initial feed and final feed.

In conclusion it has been demonstrated that inclined sedimentation can be used successfully to enrich MTC particle suspensions in particles exceeding 10 μm in diameter. Using this tool it can be determined whether or not higher levels of such particles than permitted by USP standards are present in MTC suspensions.

Literature Cited

Batchelor, G.K., Wen, C.-S. (1982) J. Fluid Mech. **119**: 379-408.
Davis, R.H., Zhang, X., Agarwala, J.P. (1989) Ind. Eng. Chem. Res. **28**: 785-793.
Mason, D.W. (1976) Biophys. J. **16**: 407-416.
Winoto-Morbach, S., Tchikov, V., Muller-Ruchholtz, W. (1994) J. Clin. Lab. Anal. **8**: 400-406.
Yiacoumi, S., Roundtree, D.A., Tsouris, C. (1996) J. Colliod Interface Sci. **184**: 477-488.
Zborowski, M. (1997) *Scientific and Clinical Applications of Magnetic Carriers*. Eds. Hafeli, U., Schutt, W., Teller, J., Zborowski, M. Plenum Press, New York, p. 205.

A Coupled Model of the Cardiorespiratory and Thermoregulatory Effects: Dehydration Effects

Dawn Downey and Richard C. Seagrave
Department of Chemical Engineering and Biomedical Engineering Program
Iowa State University, Ames, Iowa 50011

ABSTRACT

In this work, we have developed a coupled dynamic model of the cardiorespiratory and thermoregulatory systems of the human body. This model integrates energy balances for a compartmentalized system representing the core, muscles, and skin of the body with mass balances for oxygen and carbon dioxide. The resulting differential equations are coupled by equilibrium relationships including dissociation curves and expressions for a respiratory quotient and calorific oxygen equivalence. Control relations are used to calculate blood flows, ventilation rate, and evaporative heat loss. In the case of skin blood flow, the relationship is also a function of metabolic rate and environmental temperature.

The environment has a significant effect on these balances, as does the activity level of the subject. We first developed this model to describe the competitive interactions between skin and muscle in their need for blood flow during exercise and/or heat stress. More recently, we have studied the effects of training and acclimation upon the functioning of the body during exercise in the heat and have revised the control relationships to account for the resulting changes. In addition, we have modified the model to account for some of the diverse situations that are often encountered by the body. Examples considered include water immersion, swimming, and dehydration.

This paper will highlight the case of dehydration where water lost mainly through the process of sweating is not replaced. It is a particularly interesting example since serious complications can result when the body is deprived of water. Decreases in evaporative heat loss, skin blood flow, and body weight are all observed and the energy balances that we are examining do not approach a steady-state value as they do with complete water replacement. Temperatures, thus, increase more quickly in the body and any exercise which is taking place becomes limited.

INTRODUCTION

Dehydration effects, which are most important in the functioning of the cardiovascular system, have been studied as well as other possible hydration states and their various influences on maintaining blood volume. Water is lost from the blood stream during exercise, traveling from the intravascular to the interstitial space and decreasing stroke volume. Water is lost from the body through the respiratory system, as well as through evaporation from the skin surface. This results in a decreased body weight, which can become significant (1).

Due to this hypovolemia that often occurs during exercise, cardiac output can be lowered, muscle blood flow may be lowered, and, consequently, muscle tissue perfusion may then be lowered. Cutaneous blood flow is also lowered at any given internal temperature. Typically, the heart rate increases in an attempt to preserve these blood flows in the face of the lowered stroke volume. Greenleaf and Castle (2), who compared hypohydrated and hyperhydrated states, also found that oxygen uptake was slightly increased by hypohydration.

There may also be a higher circulation level of lactic acid in the blood (3). As has been previously discussed (4, 5), a competition for blood flow develops during exercise in the heat, which is enhanced by these factors. It is well documented that maintenance of central circulation blood volume has precedence over temperature control when both are limited, but hyperthermia is also an important concern. Either way, endurance time can be limited by dehydration.

During dehydration, core temperatures are higher, and the sweating mechanism is inhibited (6). In fact, the storage of body heat increases by more than a factor of two during dehydration (7). Nadel, Fortney, and Wenger (8) found that the core temperature threshold for cutaneous vasodilation was elevated slightly during hypohydration, but after the threshold was reached, the arm blood flow to core temperature relationship was unchanged from control values. They also found that maximum arm blood flow was reduced by nearly one-half, to maintain an already compromised venous return. Therefore, less heat was transferred through the skin, so the core temperature was raised to almost 39°C, much higher than when body fluids were replaced.

Euhydrated states, in which the lost fluid is replaced, have also been studied extensively. During euhydration, no significant changes are seen in blood volume or plasma volume and evaporative rates can be maintained at higher levels.

Thermoregulatory adjustments may be very different during dehydration. Even early results demonstrated this. Pitts et al. in 1944 showed that water restriction during prolonged exercise in a warm environment caused a continuous increase in core temperature, but replacement of fluid allowed for steady state to be reached after 2 h (8).

SOURCES OF WATER

In addition to the water ingested by drinking, some water is contained in the foods that are eaten. Metabolic water is also produced in the digestive system when the food is broken down to produce energy and carbon dioxide. McArdle, Katch, and Katch (9) assert that metabolic water accounts for approximately 25% of the daily water requirement for sedentary individuals.

We do not account for this metabolic water in any versions of our model, since we are primarily concerned with relatively short periods of time during exercise or heat stress. Consumption of food and its digestion is, therefore, not a major factor. In the model for dehydration, we do allow for direct input of water into the water balance on the core compartment.

During exercise, some water is liberated from the glycogen being utilized to produce energy. This amount of water should be insignificant, compared to the water loss from increased sweating that also results from exercise.

The transport of carbon dioxide in the blood has been discussed briefly (5), but its reaction with water becomes more important when we study dehydration. As ventilation increases, more carbon dioxide is removed through the lungs. This shifts the reaction with bicarbonate towards the formation of more carbon dioxide and water in the cells. However, if more carbon dioxide is being produced during exercise and the excess is not all removed by ventilation, more of the carbon dioxide will react with water to form bicarbonate.

PLASMA VOLUME DURING DEHYDRATION

One important consequence of dehydration studied extensively in literature is the decrease in plasma volume. It has previously been shown that blood volume is reduced when sweating causes a fluid loss of 2-3% of the body weight (9). This can have a significant effect, as pressures in the vascular system are compromised with the reduced volumes. In our model, we have not taken this into account since we have not studied total pressure changes. Blood volume changes are only included in the dynamics of the model, and it was previously determined that changes in these volumes are insignificant to the model results (5).

MODIFICATIONS TO THE MODEL

Some of the numerous effects of dehydration reviewed in the first section of this paper can be

applied in our model. Since we are mainly concerned with blood flows throughout the body, we have focused on the effects of water loss on the flow relationships developed in this work. Specifically, control relations for skin blood flow and evaporative heat loss were modified to agree with temperature changes in the core.

When water lost through sweating reaches the estimated minimal level necessary to trigger water conservation, skin blood flow and evaporative heat loss begin to decrease at constant rates. Presumably, at some later time after more water is lost, muscle blood flow will also start to decrease. This has not been taken into account, however, and we have not attempted to study the limits of dehydration. Understandably, most experiments involving hypohydration do not look at extreme levels of dehydration.

During hypohydration, temperatures do not reach a new steady-state level during exercise and/or heat stress, as occurs during water replacement. This is also shown in our model, as the energy balances do not reach steady-state when blood flows are changing with water loss.

MODEL RESULTS

The graphs included here compare the model results to the data in ref. 8. Figure 1 shows the model for trained subjects compared to the measurements of Nadel, Fortney, and Wenger for esophageal temperatures in the euhydrated state. Euhydration is commonly defined as the hydration state in which water lost through sweat is replaced. In this case, it is referring to the control group of subjects who were not pretreated with drugs to induce hypohydration or hyperhydration.

Figure 2 compares the same model with data for hypohydration, where diuretics were administered to the subjects prior to the experiments in order to increase body water loss through the kidneys without excessive potassium loss. Esophageal temperatures are generally underestimated in this case because complete water replacement is assumed in the model. In Figure 3, the same data are compared with the model modified for dehydration. These data were used to set the gain for the decreases in skin blood flow and evaporative heat loss accompanying dehydration.

REFERENCES

1. B. Saltin. Circulatory response to submaximal and maximal exercise after thermal dehydration. *J. Appl. Physiol.*, 19:1125-1132, 1964.
2. J. E. Greenleaf and B. L. Castle. Exercise temperature regulation in man during hypohydration and hyperhydration. *J. Appl. Physiol.*, 30:847-853, 1971.
3. E. R. Nadel. Body fluid and electrolyte balance during exercise: Competing demands with temperature regulation, in *Thermal Physiology*, ed. J. R. S. Hales, pp. 365-376. New York: Raven Press, 1984.
4. D. Downey. Development of a coupled model of the cardiorespiratory and thermoregulatory systems. Ph.D. Dissertation, Iowa State University, Ames, Iowa, 1998.
5. D. Downey. A coupled model of the cardiorespiratory and thermoregulatory systems. M.S. Thesis, Iowa State University, Ames, Iowa, 1996.
6. M. H. Harrison, R. J. Edwards, and P. A. Fennessy. Intravascular volume and tonicity as factors in the regulation of body temperatures. *J. Appl. Physiol.*, 44:69-75, 1978.
7. D. H. Hortsman and S. M. Horvath. Cardiovascular and temperature regulatory changes during progressive dehydration and euhydration. *J. Appl. Physiol.*, 33:446-450, 1972.
8. E. R. Nadel, S. Fortney, and C. B. Wenger. Effect of hydration state on circulatory and thermal regulations. *J. Appl. Physiol.*, 49:715-721, 1980.
9. W. D. McArdle, F. I. Katch, and V. L. Katch. *Exercise Physiology: Energy, Nutrition, and Human Performance*. Second Edition. Philadelphia: Lea and Febiger, 1986.

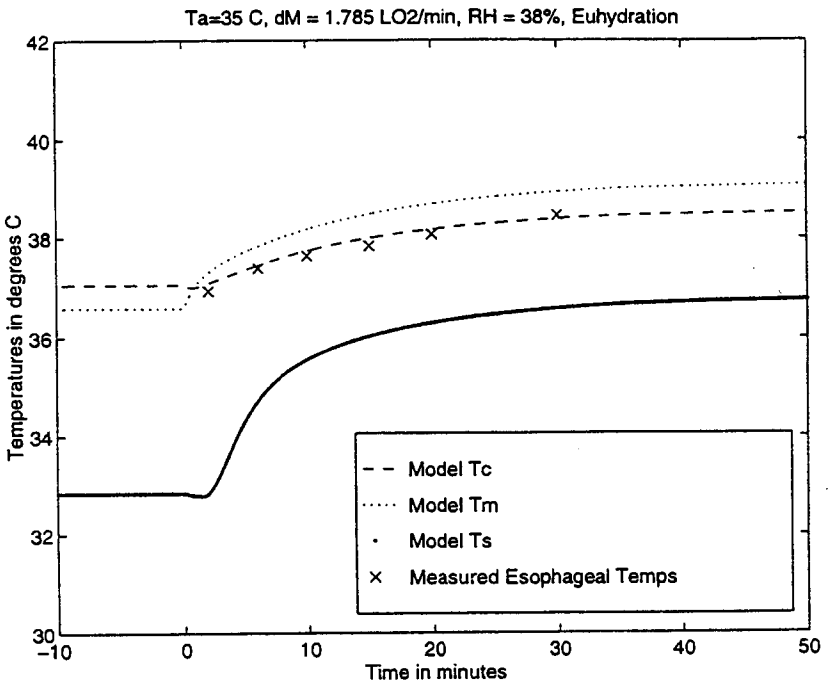

Figure 1. Data of euhydrated subjects in a control experiment where dehydration was not induced are compared to the original model predictions for the case of complete water replacement. Exercise at 55% of the maximum oxygen uptake begins at time zero in a 35°C and 38% relative humidity environment. Simulation results of our model are represented by the three lines. Data for average esophageal temperatures are taken from ref. 8. Esophageal temperature is a common representation of core temperature.

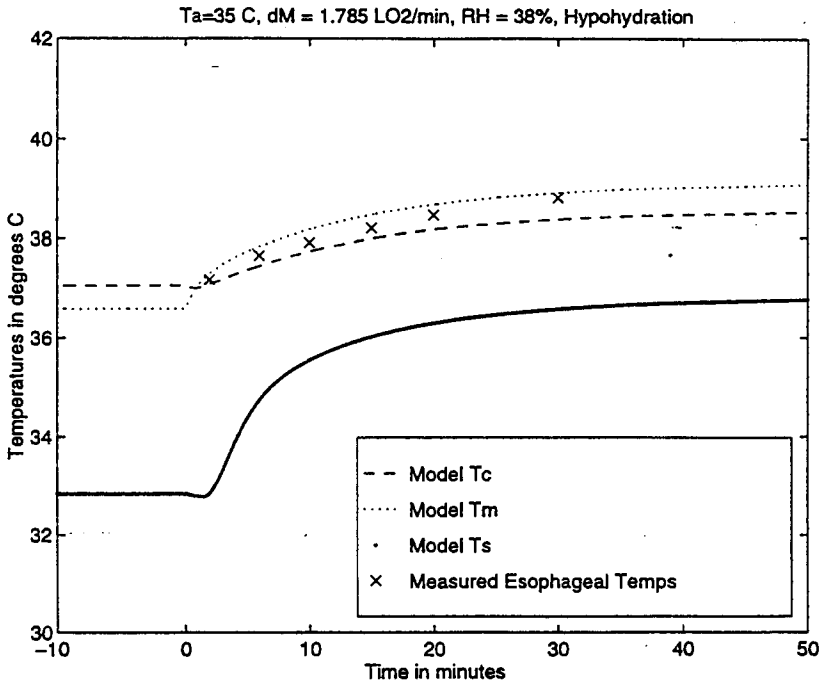

Figure 2. Data of dehydrated subjects are compared to the original model predictions. These data are underestimated by the model which assumes complete water replacement. Exercise at 55% of the maximum oxygen uptake begins at time zero in a 35°C and 38% relative humidity environment. Simulation results of our model are represented by the three lines. Data for average esophageal temperatures are taken from ref. 8. Esophageal temperature is a common representation of core temperature.

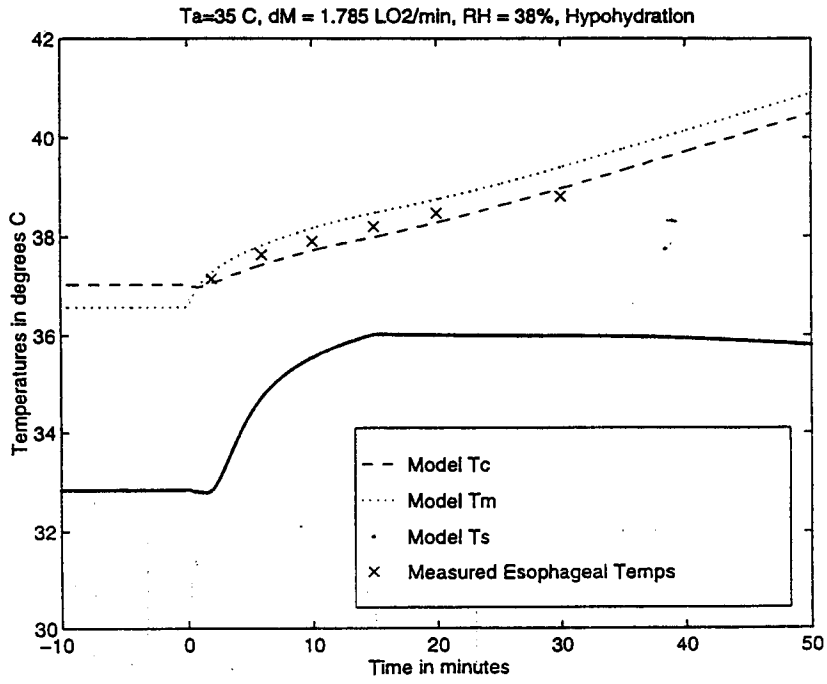

Figure 3. Data of dehydrated subjects are compared with the model modified to include the effects of dehydration. Notes as in Figure 2.

Uptake of Trichloroethylene by Plants

Jiang Hu[1], L. C. Davis[2], and L. E. Erickson[1], Departments of [1]Chemical Engineering and [2]Biochemistry, Kansas State University, Manhattan, KS 66506

Abstract

To study the uptake of trichloroethylene (TCE) by plants, single-bottle experiments were conducted with willow and poplar trees. Uncontaminated plants were grown hydroponically for several weeks before being transferred to bottles, with contaminated water occupying 50% to 70% of the bottle volume. Plants were grown in contaminated water for 1 to 2 days. Total bottle weights were measured twice each day. The average water usage was about 4.3 mL/h for willow and 10.7 mL/h for poplar. TCE concentration in the aqueous phase was measured once each day. From 14% to 69% of TCE was lost from the bottle during the growing period. Plants were then cut into pieces and sealed in small bottles. Equilibrium TCE concentrations were measured in the gas phase of the small bottles. The measured concentrations of TCE in the plant segments were larger at the lower positions along the stem and smaller as the branches decreased in size. Accordingly, we can conclude that plants such as willow and poplar have the ability to transpire TCE and to release it into the atmosphere.

Introduction

Phytoremediation, the use of vegetation for the *in situ* treatment of contaminated soils and sediments, is a novel technology that promises effective and inexpensive cleanup of certain hazardous waste sites (Schnoor et al., 1995; Burken and Schnoor, 1997). This technology has already been shown to be effective in a number of experiments. A previous study by Wang and Jones (1994) reported the uptake of chlorobenzenes (CBs) by carrots. Recent work by Newman et al. (1997) demonstrated that hybrid poplars have the capability to take up and degrade the chlorinated solvent TCE. Studies by our group also show that alfalfa and hybrid poplar have the capability to take up and transpire organic contaminants (Davis et al., 1998). In order to study the uptake of TCE by plants, single-bottle experiments were conducted with willow and poplar trees to investigate the fate of contaminant transport in plants.

Experimental Materials and Methods

Plant Growth Conditions

Willow and hybrid poplar trees transferred from the soil were grown hydroponically for several weeks before being transferred to the experimental conditions. Figures 1 and 2 show the experimental setup in which TCE was added to give approximately 10 μM aqueous-phase concentrations. In experiments 1 and 2, the total liquid volume was about 800 mL in a 1500-mL bottle; for experiments 3 and 4, it was about 3 L in a 4 L bottle. Plants were set under lights for 24 to 48 h in the laboratory before being cut for sampling of TCE concentrations. The room temperature was 25°C; TCE concentration within the bottle was sampled once a day. Decrease of O_2 and increase of CO_2 in the gas phase was also monitored to assure that root systems did not become anaerobic.

TCE Analysis

After growing for 24 to 48 h, plants were cut into pieces of about 1 g fresh weight and sealed in numbered 65-mL bottles sealed with Pierce Reacti-Vial caps. After 7 to 8 h, the TCE concentration was sampled from the gas space of each bottle. After TCE analysis, the length, diameter, fresh weight and dry weight of plant pieces were measured. In the first experiment it was shown that gas-phase TCE did not change appreciably between 6 and 18 h.

TCE Mass Balance Calculations

Initial mass of TCE in the liquid phase in the bottle is calculated by $C_{init}V_{init}$, where C_{init} is initial TCE concentration in the bottle liquid phase and V_{init} is initial amount of liquid added in the bottle. Mass of TCE uptake was calculated by V_{uptake} $(C_{init} + C_{final})/2$, where V_{uptake} is the volume of water usage and C_{final} is the final TCE concentration in the bottle liquid phase. Percentage of TCE leaked from the bottle was calculated by $[(M_{init} - M_{final} - M_{uptake})/M_{init}]$ 100%, where M_{init} is initial mass of TCE put into the bottle, M_{final} is final mass left in the bottle, and M_{uptake} is the mass of plant uptake. Percentage of TCE uptake is calculated by dividing mass of TCE uptake by total mass lost from the bottle. Percentage of TCE found in the plant is calculated by dividing recovered mass of TCE in plant by mass of TCE uptake.

Estimation of TCE in Plant Pieces

The measured TCE concentration in the gas phase of the sample bottle is assumed to be in equilibrium with that in the liquid and solid phases associated with cut plant pieces. The measured gas concentration, dimensionless Henry's law constant, and adsorption coefficient are used to estimate the mass of TCE in the plant piece. The values used are 0.4 for Henry's law constant and 30 for adsorption coefficient. The equation used to calculate the mass of TCE in plant pieces of a sample bottle is

$$M_{tot} = C_g V_g + (C_g V_{Ls} \theta_L + K C_g V_{Ls}(1 - \theta_L))/H$$

where

M_{tot} is the total mass in plant pieces in a sample bottle
C_g is the measured TCE concentration in the gas phase of the sample bottle
V_g is the volume of the sample bottle
V_{Ls} is the total volume of the stem pieces in the sample bottle
θ_L is the water content of the stem pieces
K is the adsorption coefficient; approximately equal to 30 based on a previous study (Hu et al., 1998)
H is the Henry's constant; equal to 0.4.

Results and Discussion

Diameter Change in Plants

Table 1 presents values of average stem diameter, plant fresh weight, plant dry weight, and dry weight of plant stem and branches/shoots. The water content estimated in experiments is in the range of 65% to 75% of plant total weight. Leaves and petioles, branchlets, and roots com-

prised a variable fraction of total dry weight and had a higher water content, about 80% to 90%, than stems.

TCE Distribution in Plants

Figures 3a to 3d present the experimental data for TCE distributions along plant main stem and branches/shoots. The measured concentrations of TCE in the plant segments are larger at the lower positions along the stem and smaller as the branches decrease in size. Some TCE appears to be lost to the atmosphere due to diffusion.

TCE Mass Balance

Table 2 contains values of plant water usage during each experiment, mass of TCE uptake by plants, initial mass of TCE in the bottle, mass of TCE recovered from the bottle and plant, and percentage of TCE leaked from the bottle, taken up by plants, and found in plant pieces. The results show there is about 4% to 57% of TCE leaked from the bottle; of the amount lost from the bottle, 18% to 72% went into plants, while 17% to 47% of the amount of TCE uptake was recovered from the plant pieces.

Summary

From the experiments, we found that plants such as willow and poplar have the ability to transpire TCE and to release it into the atmosphere. During the growing period, 14% to 69% of TCE was lost from the bottle; among this, 4% to 57% was lost because of the leakage of the bottle, 18% to 72% of it went into the plants, and 17% to 47% of the TCE uptake remained in the plants.

Acknowledgment

This research was partially supported by the U.S. EPA under assistance agreement R-819653 to the Great Plains-Rocky Mountain Hazardous Substance Research Center for regions 7 and 8 under project 94-27. It has not been submitted to the EPA for peer review and, therefore, may not necessarily reflect views of the agency and no official endorsement should be inferred.

References

J. G. Burken and J. L. Schnoor, 1997. "Uptake and Metabolism of Atrazine by Poplar Trees", Environ. Sci. Technol., 31, 1399-1506.

Davis, L. C., M. K. Banks, A. P. Schwab, M. Narayanan, L. E. Erickson, and J. C. Tracy, 1998. "Plant-Based Bioremediation," In Bioremediation, Principles and Practice, Vol. 2, S. K. Sikdar and R. L. Irvine, Eds., Technomic, Lancaster, Pa., pp. 183-217.

Davis, L. C., S. Vanderhoof, J. Dana, K. Selk, K. Smith, B. Goplen, and L. E. Erickson, 1998. "Chlorinated Solvent Movement Through Plants Monitored by Fourier Transform Infrared (FT-IR) Spectrometry," J. Haz. Substance Res., 1(4), 1-26.

Hu, J., M. Narayanan, L. C. Davis, and L. E. Erickson, 1998. "Modeling Root Uptake and Transport of Trichloroethylene", Proc. 27th Ann. Biochem. Eng. Symp., Colorado State University, Fort Collins, Colo., 113-119.

L. A. Newman, S. E. Strand, N. Choe, J. Duffy, G. Ekuan, M. Ruszaj, B. B. Shurtleef, J. Wil-

moth, P. Heilman, and M. P. Gordon, 1998. "Uptake and Biotransformation of Trichloroethylene by Hybrid Poplars", Environ. Sci. Technol., 31, 1062-1067.

J. L. Schnoor, L. A. Licht, S. C. McCutcheon, N. L. Wolfe, L. H. Carreira, 1995. "Phytoremediation of Organic and Nutrient Contaminants", Environ. Sci. Technol., 29, 318A-323A.

M.-J. Wang and K. C. Jones, 1994. "Uptake of Chlorobenzenes by Carrots from Spiked and Sewage Sludge-Amended Soil", Environ. Sci. Technol., 28, 1260-1267.

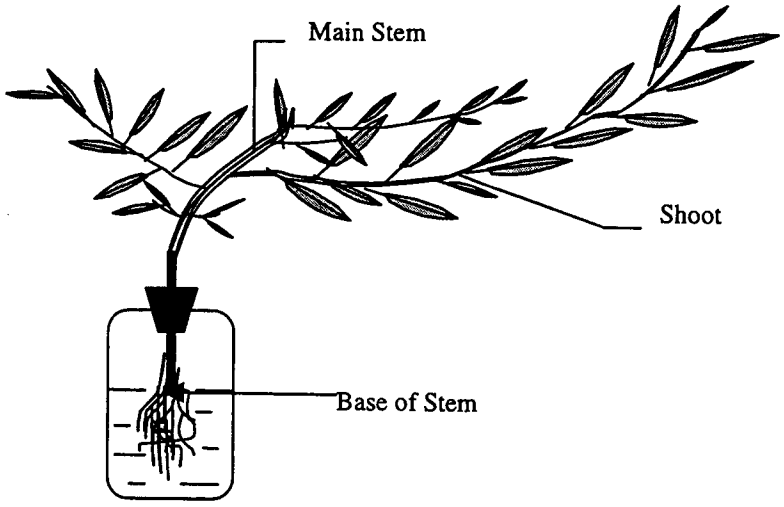

Figure 1. Willow plant 1 experimental schematic. The plant was grown hydroponically in contaminated water for 48 hours; plant roots were immersed in the water; plant stem went through the rubber stopper; the jar was sealed around stem with wax.

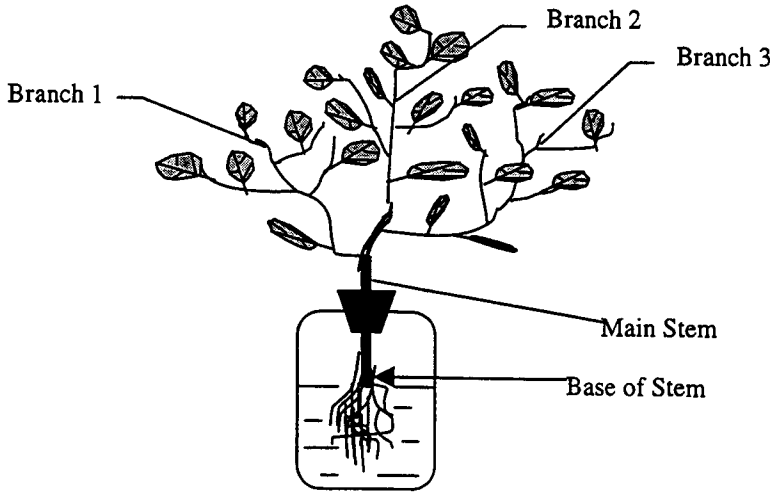

Figure 2. Poplar plant 1 experimental schematic. The plant was grown hydroponically in contaminated water for 25 hours; plant roots were immersed in the water; plant stem went through the rubber stopper; the jar was sealed around stem with wax.

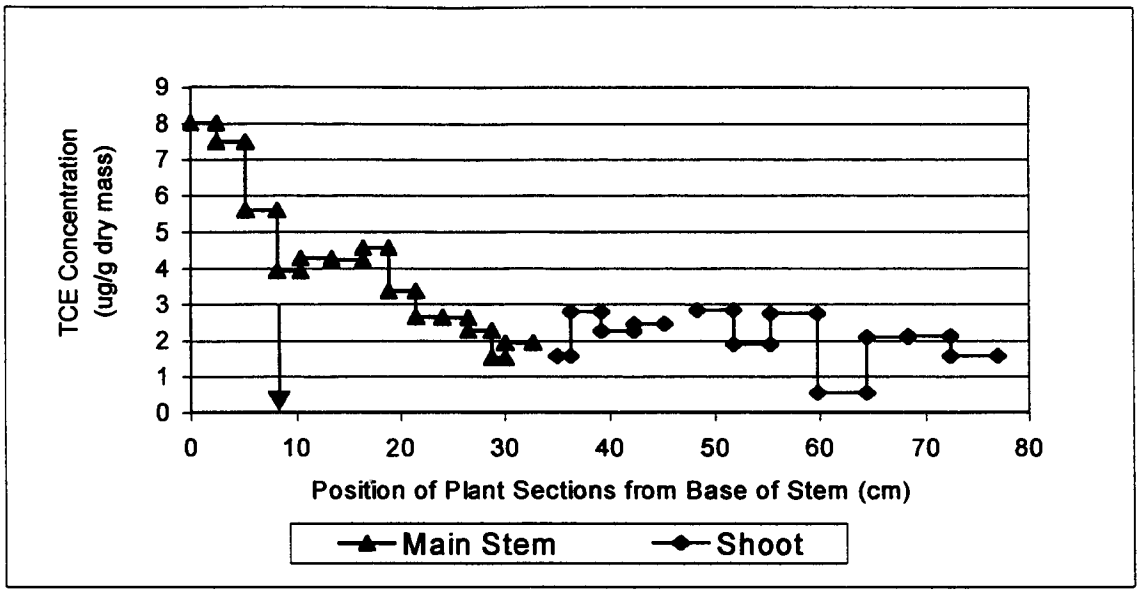

Figure 3A. TCE concentration in willow plant 1. Position 0 to arrow indicates sections inside the bottle. Initial concentration of TCE in the bottle was 0.94 μg/g water; final TCE concentration in the bottle liquid phase was 0.32 μg/g water; experimental time was 48 hours.

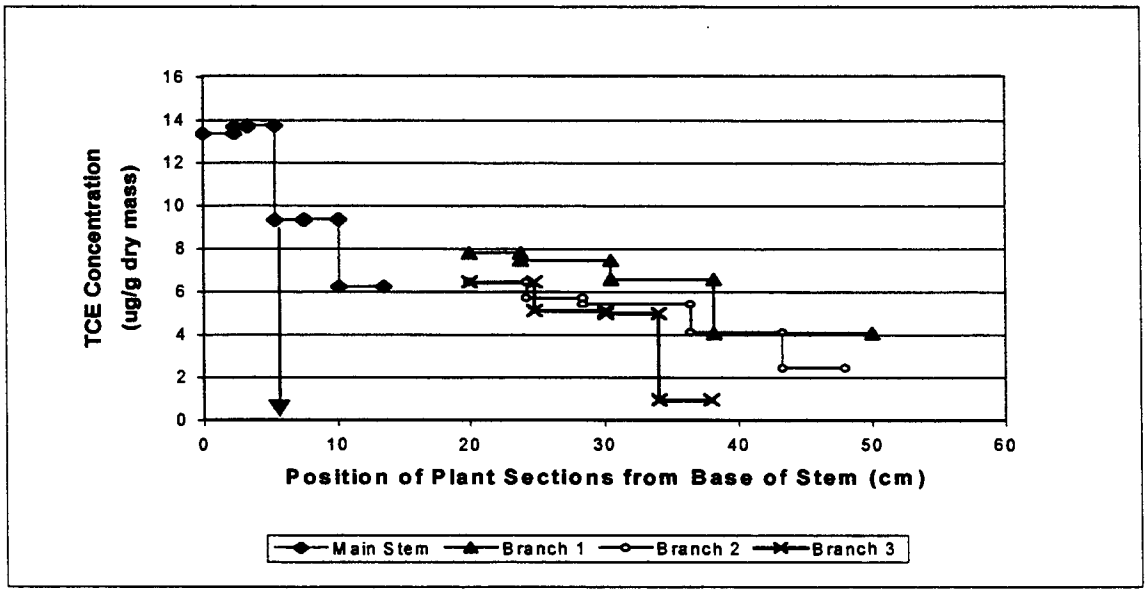

Figure 3B. TCE concentration in poplar plant 1. Position 0 to arrow indicates sections inside the bottle. Initial concentration of TCE in the bottle was 1.2 μg/g water; final TCE concentration in the bottle liquid phase was 0.5 μg/g water; experimental time was 25 hours.

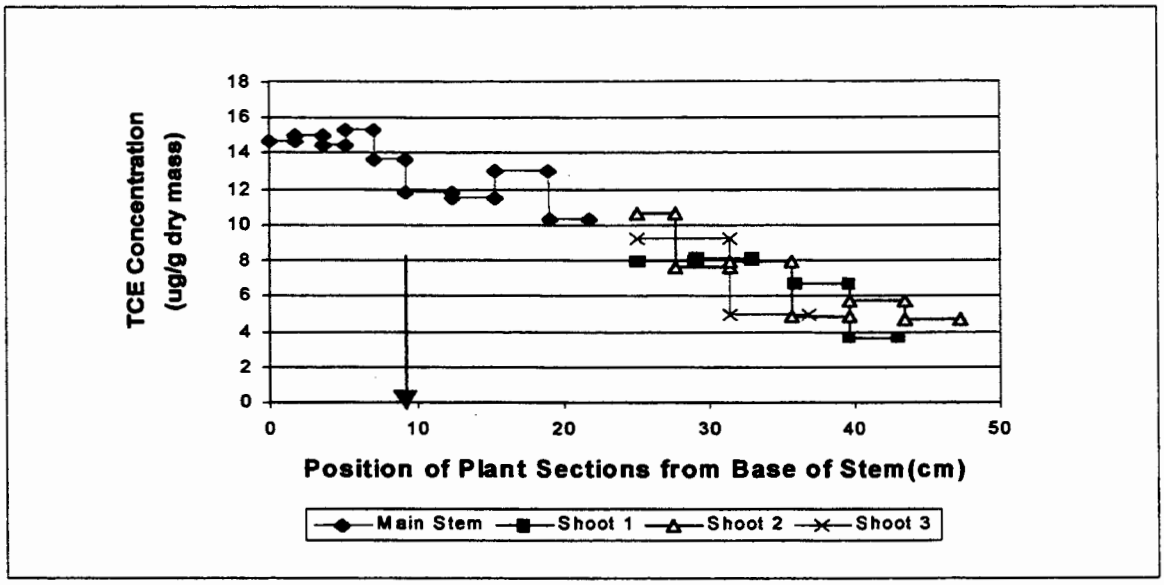

Figure 3C. TCE concentration in willow plant 2. Position 0 to arrow indicates sections inside the bottle. Initial concentration of TCE in the bottle was 1.15 μg/g water; final TCE concentration in the bottle liquid phase was 0.94 μg/g water; experimental time was 42 hours.

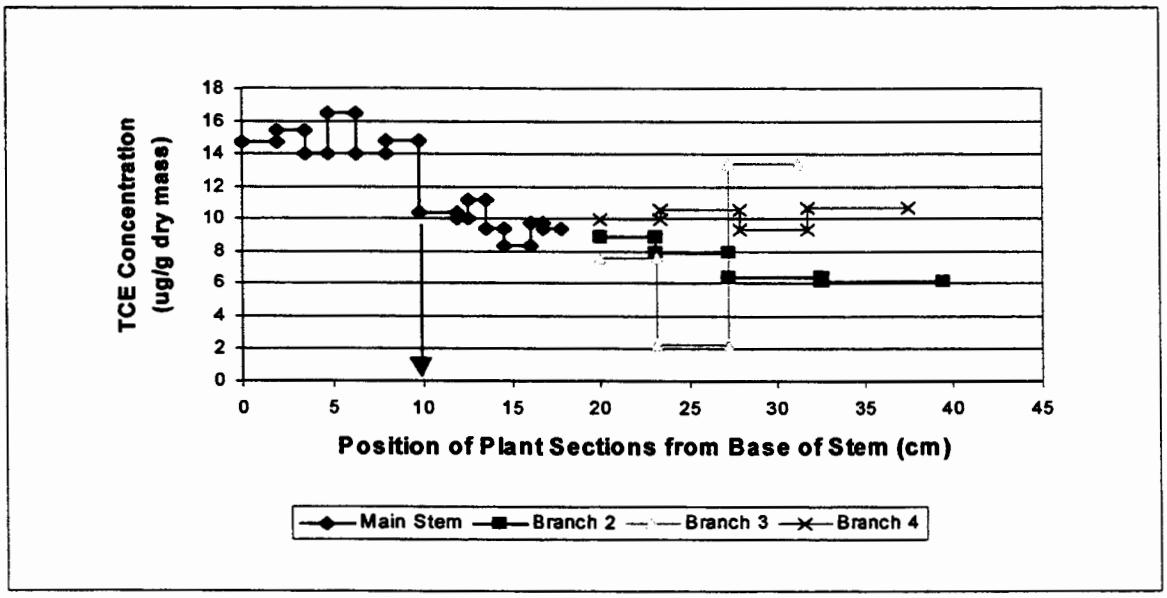

Figure 3D. TCE concentration in poplar plant 2. Position 0 to arrow indicates sections inside the bottle. Initial concentration of TCE in the bottle was 0.9 μg/g water; final TCE concentration in the bottle liquid phase was 0.83 μg/g water; experimental time was 42 hours.

Table 1. Values of Stem Diameters, Plant Total Mass, Dry Mass and Dry Mass of Stem and Branches/Shoots.

Experiment	Average Stem Diameter (mm)		Fresh Weight (g)	Total Dry Weight (g)	Stem and Branch/Shoot Dry Weight (g)
	Main Stem	Shoot/ Branch			
#1 Willow Plant 1	10	4	60	21.6	15.0
#2 Poplar Plant 1	7	3	40	10.6	4.7
#3 Poplar Plant 2	8	3	55	17.3	6.0
#4 Willow Plant 2	7	4	50	14.7	5.5

Table 2. Values of Plant Water Usage, TCE Uptake, Initial Mass of TCE in the Bottle, Mass of TCE Recovered, and Percentage of TCE Leaked from the Bottle, Taken up by Plants, and Found in Plant Pieces.

Experiment[1]	Plant Water Usage[2] (mL)	Mass of TCE Uptake[3] (µg)	Initial Mass of TCE[4] (µg)	Mass of TCE Recovered (µg)		Percentage of TCE %		
				In Plant[5]	In Bottle[6]	Leaked from the Bottle[7]	Taken up by Plants[8]	Found in Plant Pieces[9]
#1 Willow Plant 1	211 780	133	1049	63	320	57	18	47
#2 Poplar Plant 1	268 870	228	1346	38	481	47	26	17
#3 Poplar Plant 2	299 3155	312	4068	62	3156	15	34	20
#4 Willow Plant 2	383 3175	330	3194	58	2738	4	72	18

Notes:
1. Bottle volume is 1620 ml for experiment 1, 1500 ml for experiment 2 and 4110 ml for experiment 3 and 4.
2. Plant water usage (1st line) is the difference between the liquid phase volume in the bottle before and after the experiments. Starting liquid phase volume in the bottle is shown on 2nd line.
3. Mass of TCE Uptake is calculated by multiplying plant water usage by the average liquid phase concentration in the bottle during the experiment.
4. Initial Mass of TCE is total TCE amount added to the experimental bottle.
5. Mass of TCE recovered in plant is the sum of TCE in plant pieces which were sampled. The calculation method is shown in estimation of TCE in plant pieces.
6. Mass of TCE recovered in bottle is the sum of TCE in the bottle liquid phase and gas phase; the Henry's constant is used to calculate the liquid phase concentration.
7. Percentage of TCE leaked from the bottle is the ratio of the difference of column 4 and the sum of column 6 and column 3 to column 4.
8. Percentage of TCE taken up by plants is the ratio of column 3 to the total amount of TCE lost from the bottle.
9. Percentage of TCE found in plant pieces is the ratio of column 5 to column 3.

Phytoremediation of Washwater Sediments Contaminated with Petroleum Hydrocarbons

P. Kulakow[1], R. Karthikeyan[2], B. Leven[3], K. R. Mankin[2], and L. E. Erickson[4]
Departments of [1]Agronomy, [2]Biological and Agricultural Engineering, [3]Great Plains/Rocky Mountain Hazardous Substance Research Center, and [4]Chemical Engineering
Kansas State University, Manhattan, KS 66506

INTRODUCTION

Many army training reservations contain vehicle wash facilities where combat and other equipment are washed with high-pressure water hoses after field maneuvers. During this process, sediments containing significant concentrations of petroleum hydrocarbons accumulate in concrete sedimentation basins. Significant quantities of these sediments are generated at twelve army installations throughout United States, two of which are located in the Great Plains/Rocky Mountain region. Conventional treatment methods to decontaminate these sediments include landfill disposal or land application; however, vegetative remediation systems may offer a cost-effective alternative (Davis et al., 1996; Reilly et al., 1996; Schnoor et al., 1995).

The ultimate objective of this study was to develop an optimal phytoremediation design that rapidly reduces petroleum hydrocarbons to acceptable levels and is simple to implement and maintain. A vegetative treatment system consisting of tall fescue and western wheat grass, and tall fescue and legumes, was designed to treat approximately 136 m^3 of sediments contaminated with petroleum hydrocarbons, generated by Central Vehicle Wash Facility (CVWF), Fort Riley, Kansas. This report presents a brief outline of site characterization, vegetation treatment system design, and some preliminary results.

SITE CHARACTERIZATION

Washwater from the CVWF flows into an impoundment, where particulate matter settles and light petroleum products are removed. Approximately 765 m^3 of water-saturated sediments are removed from the washwater impoundment every six to nine months and spread across the ground surface in 50- to 100-cm thick layers near the crest of a nearby hill. To date, approximately 3440 m^3 of sediments exist at the land application site. Laboratory analysis of representative sediment samples from the impoundment and land application site indicate measurable Total Petroleum Hydrocarbon (TPH) concentrations between 482 and 3800 mg/kg. The Kansas Department of Health and Environment (KDHE) generally considers cleanup goals for TPHs in soils as 100 mg/kg, but grants variances depending on future uses of contaminated soils.

VEGETATIVE TREATMENT SYSTEM DESIGN

In the existing field trial, approximately 136 m^3 of sediments were spread on mowed native grassland in July 1997. The sediments were spread approximately 30 cm deep. On September 22, 1997, a vegetative treatment scheme was established with three vegetation treatments including

unvegetated plots, a grass mixture consisting of tall fescue and western wheatgrass, and a grass-legume mixture consisting of tall fescue with red clover, birdsfoot trefoil, and yellow sweetclover. The plots were arranged in a randomized complete block design with four replicates. Composite samples of the sediments and the underlying native soil were analyzed for chemical and physical properties (Table 1). The experimental plots were sampled three times (September 30, 1997, April 22, 1998 and August 28, 1998) to determine TPH concentration, aboveground biomass production, and plant rooting density.

PRELIMINARY RESULTS

Average initial TPH concentration in the sediments was 922 mg/kg (Table 2). Planting started on September 1997 and soil samples were collected on September 30, 1997. Mean TPH for all plots was 821 mg/kg (Table 2). Mean TPH concentrations in grass-legume and grass plots were 712 ± 142 and 904 ± 230 mg/kg, respectively. After six months, the mean TPH concentrations in grass-legume and grass plots were reduced to 294 ± 45 and 311 ± 29 mg/kg, respectively. Mean TPH for all plots was 310 mg/kg, with no significant differences in TPH concentrations among treatments (Table 2). The average reduction in TPH after six months was about 62% (Table 2).

Plant establishment and growth was excellent in all vegetated plots. The unvegetated plots were periodically weeded to keep them free of vegetation. Both vegetation treatments produced nearly equal amounts of above-ground biomass (Table 3). Estimates of plant rooting density are presented in Table 4. Although both vegetation treatments produced equal amounts of above-ground biomass, grass mixtures have higher rooting densities in the top 30 cm of soil than grass-legume mixtures. This reflects differences in rooting morphology between legumes and grasses.

Since vegetation reduces soil erosion due to wind and water, it has beneficial environmental effects. Based on the results obtained so far, there is no significant difference among treatments. It is reasonable not to see any significant differences between vegetated and unvegetated treatments during the first year when plant establishment takes place. Monitoring of the vegetation treatments will continue for two years to see the effectiveness of vegetation and the end-point TPH concentration.

REFERENCES

Davis, L. C., L. E. Erickson, E. Lee, J. F. Shimp, and J. C. Tracy. 1993. Modeling the effects of plants in the bioremediation of contaminated soil and groundwater, *Environ. Prog.*, 12: 67-75.

Reilly, K., M. K. Banks, and A. P. Schwab. 1996. Dissipation of polynuclear aromatic hydrocarbons in the rhizosphere, *J. Environ. Qual.*, 25: 212-219.

Schnoor, J. L., L. A. Licht, S. C. McCutcheon, N. A. Wolfe, and L. H. Carriera. 1995. Phytoremediation of organic and nutrient contaminants, *Environ. Sci. Technol.*, 29: 313-318.

Table 1. Physical and chemical properties of Central Vehicle Wash Facility (CVWF) sediments and native soil (where the sediments were land applied).

Characteristic	Unit	CVWF sediment	Native Soil
Texture			
Sand	%	40	20
Silt	%	44	62
Clay	%	16	18
pH		8	6.4
Organic Matter	%	2.8	3.8
NH_4^+	mg/kg	6.4	6.9
NO_3^-	mg/kg	5.1	1.8
Bray P	mg/kg	1	6
Total N	mg/kg	1027	703
Total P	mg/kg	255	173
Sulfate	mg/kg	28.2	3.2
Chloride	mg/kg	4	2
Exchangeable Cations			
K	mg/kg	209	301
Ca	mg/kg	4740	3350
Mg	mg/kg	370	605
Na	mg/kg	38.3	13.2
Cation Exchange Capacity (CEC)	mmole/kg	14.3	28.8
Soluble Salts	ds/m	NA	NA

Table 2. Total Petroleum Hydrocarbons (TPH) in different treatment plots.

Sampling/Date	Treatment	TPH (mg/kg)	
		Mean	Standard Deviation
Initial (Before Planting)/ 7/11/1997		922	246
Time 0 (During Planting)/ 9/30/1997	All Plots	821	199
	Unvegetated	846	214
	Grass-Legume	712	142
	Grass Mixture	904	230
	Native Soil	61	49
Time 1 (6 Months After Planting)			
4/22/1998	All Plots	310	44
	Unvegetated	326	60
	Grass-Legume	294	45
	Grass Mixture	311	29

Table 3. Above-ground biomass in different vegetation plots.

Vegetation Treatment	Sampling Time	Above-ground Biomass (g/m^2)	
		Mean	Standard Deviation
Grass Mixture	Time 1 (April 1998)	70.0	28.9
	Time 2 (July 1998)	393.3	79.8
Grass-Legume Mixture	Time 1 (April 1998)	72.7	22.8
	Time 2 (July 1998)	411.9	71.5

Table 4. Rooting density in different vegetation plots (Time 1: April 1998).

Vegetation Treatment	Depth of Sampling (cm)	Root Diameter (mm)		Root Length Density (mm/mL)		Root Surface Area Density (mm^2/mL)		Root Length (mm)	
		Mean	Std. Dev.	Mean	Std. Dev.	Mean	Std. Dev.	Mean	Std. Dev.
Grass Mixture	0-15	0.31	0.05	21.1	9.9	21.0	11.5	6239	2917
	15-30	0.42	0.12	5.8	4.8	6.5	3.6	1724	1422
Grass-Legume	0-15	0.36	0.06	15.7	12.3	16.8	12.4	4629	3618
	15-30	0.48	0.09	3.2	2.5	4.7	3.4	941	746

AUTOMATED DOCKING OF MALTOSE, 2-DEOXYMALTOSE, AND MALTOTETRAOSE INTO THE SOYBEAN β-AMYLASE ACTIVE SITE

Alain Laederach,[1] Michael K. Dowd,[2] Pedro M. Coutinho,[3] and Peter J. Reilly[1]
[1]Department of Chemical Engineering, Iowa State University, Ames, Iowa 50011; [2]Southern Regional Research Center, U.S. Department of Agriculture, New Orleans, Louisiana 70179; [3]Centre de Recherches sur les Macromolécules Végétales, CNRS, F-38041 Grenoble, France

ABSTRACT

β-Amylase hydrolyzes α-1,4-linked maltooligosaccharides to β-maltose and hydrates maltal to α- and β-2-deoxymaltose. In this study, products and substrates were docked into the active site of β-amylase using the simulated annealing algorithm AutoDock. Top energy conformers reproduced known crystallographic atom positions within 0.4-0.8 Å root mean square deviation. As β-amylase has a mobile flap that covers the active site during hydrolysis and extends into the solvent otherwise, docking studies were carried out with both configurations. In general, disaccharides dock preferentially into subsites -2,-1 when the flap is closed and +1,+2 when the flap is open. No substrate larger than two rings docked into the open-flap configuration, indicating that the flap accompanies the substrate into the cleft. The sum of the total binding energies of two maltose molecules docked to subsites -2,-1 and +1,+2 is more negative than that of a bound maltotetraose molecule by 67.5 kcal/mol, providing the driving force of the hydrolysis reaction. Maltotetraose hydrolysis allows the two product maltose molecules to adopt more favorable conformations, allowing greater interaction with the protein.

INTRODUCTION

β-Amylase [α-(1,4)-D-glucan maltohydrolase, EC 3.2.1.2] liberates β-maltose from the nonreducing ends of α-1,4-linked maltooligosaccharides.[1,2] It functions by multiple attack, several maltose molecules being produced before the maltooligosaccharide chain is released from the active site.[2,3] β-Amylase is unable to hydrolyze any bonds other than α-1,4 glycosidic bonds between adjacent glucosyl residues,[4] and therefore it leaves partially hydrolyzed fragments collectively known as β-limit dextrin from amylopectin, a highly branched maltooligosaccharide whose branches are initiated by α-1,6 glycosidic bonds. However, it promotes several other reactions, such as the condensation of β-maltose into maltotetraose[5] and the hydration of maltal [α-D-glucopyranosyl-(1→4)-2-deoxy-D-*arabino*-hex-1-enitol] to produce 2-deoxymaltose.[6,7]

Five high-resolution crystal structures of soybean β-amylase have been obtained, one with the SH-alkylated enzyme soaked with the competitive inhibitor α-cyclodextrin[8] (Brookhaven Protein Databank **1btc**) and four with the unmodified enzyme in various forms:[9] unliganded (**1bya**), soaked with 8 mM maltose (**1byb**), soaked with 200 mM maltose (**1byc**), and soaked with maltal (**1byd**). The enzyme is composed of a single domain containing the active site and forming an $(\alpha,\beta)_8$ barrel core (Figure 1). Four subsites labeled -2,-1,+1,+2, with the nonreducing end of the substrate being directed toward subsite -2 and the cleavage point being located between subsites -1 and +1, have been identified.[8,9]

When β-amylase was soaked with β-maltose, two β-maltose molecules were found in the active site by X-ray diffraction.[9] Soaking with maltal lead to one molecule of β-deoxymaltose in subsites -2,-1 and one molecule of α-deoxymaltose in subsites +1,+2.[9] The catalytic acid for hydrolysis is Glu186 (soybean β-amylase numbering), while the catalytic base is Glu380. For the

hydration of maltal to 2-deoxymaltose and the condensation of maltose to maltotetraose, on the other hand, Glu380 is the general acid. The nonreducing-end substrate glucosyl residue (Glc_A) is hydrogen-bonded by Asp53, His93, Asp101, and Arg420, with Glc_B being bound by Lys295, Asn381, and Ala382, Glc_C by Arg188, Tyr192, Gly298, Phe341, and Thr342, and Glc_D by His300;[9] all are totally conserved.[11]

A noteworthy structural feature of β-amylase is the flexible loop (or flap) segment comprising residues 96-103.[8,9] All are completely conserved except residues 102 and 103.[11] The straight-line distance traveled from the open to the closed position by the middle of the this flap, at Val99 and Gly100, is approximately 10 Å (Figure 1).[9] The flap covers the active site during hydrolysis and extends into the solvent during substrate capture and product release.[9] It is believed that flaps like the one in β-amylase act as solvent shields during hydrolysis, creating a convenient catalytic environment.[12]

In this study we used automated docking by simulated annealing to investigate ligand-protein interactions in the soybean β-amylase active site. This technique allows observation of interactions of substrates as well as products and inhibitors in the active site, whereas in most case enzyme crystal structures with bound substrates cannot be obtained. In addition, automated docking yields information on feasible bound structures other than the one found in the crystal structure. Automated docking of saccharides into the glucoamylase active site has been an efficient means to better understand subsite mechanisms in this closely related starch-hydrolyzing enzyme.[13-16] A similar simulation approach was used here. However, due to the more complex nature of β-amylase, with its flexible flap, both anomeric forms of maltose and 2-deoxymaltose were docked, along with α-maltotetraose, into both the closed- and open-flap forms of β-amylase.

COMPUTATIONAL METHODS

Automated docking simulations were conducted with AutoDock 2.4[17-19] (Scripps Research Institute, La Jolla, Cal.), using crystal structures **1bya** and **1byb**[9] to generate atomic energy grids. All water and maltose atoms were removed except for water number 501, as this led to better correlations with crystallographic data in preliminary tests. Hydrogen atoms were added to the crystal structure using the WHAT IF[20] server. Atomic partial charges were assigned to the protein atoms using the PIM[21,22] method. Disaccharide docking simulations were run on either SGI Indigo II Extreme or DEC Alpha Mips workstations. For maltotetraose, all simulations were run on a DEC AlphaServer 8400. Other computational techniques were the same as those used earlier.[13-16]

For each carbohydrate ligand, a population of starting structures was generated based on MM3 molecular mechanics studies of maltose.[23] For maltose, the population corresponded to the set of low-energy minima (< 8 kcal/mol) found within the ϕ,ψ maltose conformational space. Because the exo-cyclic hydroxyl groups had only a minor influence on the orientation of the disaccharide structures, 2-deoxymaltose structures were derived from the energy-minimized maltose structures with the 2-OH group replaced by hydrogen. α-Maltotetraose structures were generated using the set of disaccharide orientations for each glycosidic linkage. Energies of all structures were minimized with MM3(92) at $\varepsilon = 4.0$. For α-maltotetraose, the additional glucose units did not greatly affect the orientation of the rings about the glycosidic bonds, as the linkage conformations exhibited only minor changes with minimization.

At the start of each docking study, the nonreducing-end ring (Glc_A) of each substrate was placed in the active site. For disaccharides, it was placed near subsites -2, -1, and +1 in turn, while for maltotetraose it was placed near subsite -2. All disaccharide and tetrasaccharide dihedral

angles were allowed to rotate.

Docking simulations were run for each of the three α-disaccharide, four β-disaccharide, and 24 α-maltotetraose conformers having local minima within 8 kcal/mol of their respective global minima given by MM3(92).

RESULTS AND DISCUSSION

Due to the size of β-amylase (56 kDa), a complete description of the reaction including the dynamics of the enzyme would be too computationally intensive. Instead, simulations involved automated docking of α- and β-maltose, α- and β-2-deoxymaltose, and α-maltotetraose into closed-flap (Tables I-III) and open-flap crystal structures of β-amylase. The values shown are for the optimal cluster member, values in brackets being Boltzmann-weighted averages over all cluster members. Internal energies were calculated represent the contribution to total energy due to interactions between atoms of the ligand. Intermolecular energies are as computed by AutoDock, and represent the sum of all the interactions (Coulomb and Lennard-Jones) between the enzyme and the ligand.

In the case of the closed-flap simulations, lowest-energy conformers were generally within 0.4-0.8 Å RMSD of known crystallographic conformers (Tables I-III, Figure 2a,b). Docking these same structures into the open-flap configuration yielded conformers similar to those in the closed-flap configuration, except that α-maltotetraose was not accommodated in the open-flap configuration (Figure 2c).

In general, when the flap was closed, disaccharides preferentially docked in subsites -2,-1 over subsites +1,+2 by at least 2.5 kcal/mol. All top disaccharide conformers started near subsites -1,+1 docked into subsites -2,-1. No disaccharides docked in subsites -1,+1 or migrated during the simulation to subsites +1,+2, demonstrating why disaccharides are not hydrolyzed by β-amylase.

Total energy values are within 2 kcal/mol for all top disaccharide anomers. Total energy values of the top conformers of α-disaccharides are more negative than those of the corresponding β-disaccharides when docked into either subsites -2,-1 or +1,+2. As β-amylase produces only β-anomers, it is normal that these are not accommodated as well as α-anomers, since the former must be released for successive hydrolyses to occur. As Mikami et al.[9] suggest, it is likely that some α-maltose may have been present in the crystal structure due to the higher affinity of β-amylase for it.

Comparison of ligand internal energies shows that all disaccharides are more strained, with more positive values, when docked in subsites -2,-1 rather than in subsites +1,+2 (Tables I and II). On average, the difference between internal energies in the two docking positions is between 7 and 14 kcal/mol. In order to compensate, intermolecular energies are more negative for disaccharides docked to subsites -2,-1.

When the intermolecular energies of the top docked maltose conformers in subsites -2,-1 are assigned to different glucosyl rings, 59% and 55% of the contribution to the α- and β-maltose intermolecular energies, respectively, are due to interactions with Glc_A rather than Glc_B. Mikami et al.[9] suggest that since Glc_B is less ordered in electron density maps from x-ray diffraction, it is bound more loosely. The docking results confirm this finding. When maltose is docked in subsites +1,+2, 60% and 64% of the α- and β-maltose contribution to intermolecular energy, respectively,

is due to interactions with Glc_D, indicating that it docked at subsite +2 more strongly than Glc_C docked at subsite +1. Similar values are obtained for 2-deoxymaltose and maltotetraose anomers.

The total intermolecular binding energy is unevenly distributed over the entire maltotetraose molecule. When the flap comes down over the active site, it pushes Glc_B deeper into the cleft. This results in an increase of binding energy between all Glc_B carbons and the enzyme from 9.4% when the flap is open to 21.6% when it is closed.

When the flap was open, all top disaccharide conformers except that of α-2-deoxymaltose docked some distance from where the corresponding ligands were found in crystal structures with closed flaps. The position of these top conformers varied, but they were generally close to the crystallographic position of the β-amylase inhibitor α-cyclodextrin.[8] Disaccharides of higher energy that docked close to structures **1bya** when the flap was open preferentially docked into subsites +1,+2. These subsites are close to the top of the cleft, and some of the conformers started deeper (near subsite -2 or -1) migrated up during the docking simulations. These results indicate that the flap helps to hold ligands deeper in the cleft.

The total binding energy of the lowest-energy disaccharides docked to subsites +1,+2 in the open-flap configuration is 13-22 kcal/mol more positive than in the closed-flap configuration. The flap therefore adds to the binding energy when it is closed, as more favorable interactions can occur between the amino acids of the flap and the ligand.

Disaccharides docked in the open-flap configuration are less strained than those docked into the closed-flap configuration. When the flap closes, more favorable interactions occur between the enzyme and ligand, allowing more strain to be added to the ligand. As disaccharides can still bind to the active site with the flap open, even if they are not those of the lowest energy, the flap is not essential in binding, in agreement with Kunikata et al.[12]

Kunikata et al.[12] suggest that the flap acts as a shield to promote a convenient catalytic environment. As this simulation study does not incorporate solvent effects, it is difficult to demonstrate this. However, it is apparent that the flap does play a role in binding, especially to subsites -2,-1. When the flap closes it adds to the binding energy, which in turn permits greater strain on the ligand. This allows subsequent hydrolysis of maltotetraose and hydration of maltal.

Results from docking α-maltotetraose to the closed-flap configuration of β-amylase are given in Table III. RMSD values were obtained by comparing atomic positions of both β-maltose molecules bound to subsites -2,-1 and +1,+2 to the respective atomic positions in the docked α-maltotetraose conformers. The reason these RMSD values are larger (by 0.2-0.4 Å) than those obtained with disaccharides is that α-maltotetraose does not bind in the identical position as two maltose molecules. The fact that two maltose molecules are not bound to each other allows them to move apart, which favors further interactions with the protein.

The method AutoDock uses to calculate intermolecular energy implies that the computed value is directly proportional to the number of atoms in the ligand.[17-19] The top intermolecular docking energy of α-maltotetraose (-142.19 kcal/mol) is not equal to the sum (-209.65 kcal/mol) of top α-maltose conformers docked to subsites -2,-1 and +1,+2. The difference (-67.46 kcal/mol) is the driving force of the hydrolysis. As two maltose molecules have greater binding energies than a single α-maltotetraose molecule, the hydrolysis reaction is favored.

When the intermolecular energy of α-maltotetraose is allocated by ring, Glc_B and Glc_C con-

tributions increase from 22 and 25%, respectively, in cluster 1 to 27% with each ring in cluster 3, which has the most positive internal energy (8.54 kcal/mol) as well as the most negative intermolecular energy (-147.21 kcal/mol) (Table III). In general an increase in internal energy (increased strain) is accompanied by a more negative intermolecular contribution of Glc_B and Glc_C. As these rings move towards more favorable interactions with the enzyme, the substrate adopts a more strained conformation. Once a sufficiently high strain is achieved, hydrolysis can occur.

The distances between NH1 in Arg420 and O6A in α-maltotetraose in cluster 1 vary from 3.32 to 3.56 Å. This close distance and the perfect conservation of Arg420[11] indicate that it is important in substrate capture. In general, most HO6 atom intermolecular contributions are more negative with the flap open. It is apparent that hydrogen bonding between these atoms and β-amylase helps in the preliminary capture of the substrate.

The total energy of top conformers is 37.7 kcal/mol more negative for α-maltotetraose docked to the closed-flap than the open-flap configuration (Table III). This energy is part of the driving force for the closing of the flap. The release of the water molecules solvating maltotetraose also contributes to the closing free energy.

The sum of the total energies of clusters 1 and 2 in Table I (-110.33 - 107.66 = -217.99 kcal/mol) is the binding energy of two α-maltose molecules docked to the closed-flap conformation in subsites -2,-1 and +1,+2. Similarly the sum of the total energies (-88.19 - 84.77 = -172.96 kcal/mol) is the binding energy of the same α-maltose molecules docked in subsites -1,-2 and +1,+2 in the open-flap configuration. The difference (45.03 kcal/mol) represents the loss in total energy due to flap opening. Evidently other effects, such as the hydration of the two α-maltose molecules and of the hydrophilic amino acids of the flap, contribute to overcoming this barrier.

CONCLUSIONS

From these results one can suggest an action mechanism for β-amylase. In solution, the flap extends into the solvent due to its hydrophilic nature. Maltotetraose diffuses over the active site and is held in place by Arg420. The gain in binding and solvation energy drives the closing of the flap.

Hydrolysis is driven by the gain in binding energy, which is the difference in energies between the top bound α-maltotetraose molecule and two α-maltose molecules docked to subsites -2,-1 and +1,+2. Reopening of the flap and release of the captured substrate products is driven by hydration effects, which are not taken into account in this simulation study.

Automated docking of substrates and specifically sugars has proven to be an efficient technique for the understanding of complex enzymatic action mechanisms. Further studies with larger substrates such as maltopentaose will help identify other β-amylase subsites.

ACKNOWLEDGMENTS

The visit of A.L. to Iowa State University was part of an undergraduate exchange program between it and Ecole Polytechnique Fédérale de Lausanne, Switzerland. The authors thank Arthur Olson and David Goodsell of the Scripps Research Institute for providing AutoDock 2.4 and the Iowa State University Computation Center for providing computational time on its FARM server.

REFERENCES

1. Ohlsson, E. The two components of malt diastase, especially with reference to the mutarotation of the products formed in the hydrolysis of starch. Z. Physiol. Chem. 189:17-63, 1930.
2. Bailey, J.M., French, D. Significance of multiple reactions in enzyme-polymer systems. J. Biol. Chem. 226:1-14, 1957.
3. French, D., Youngquist, R.W. The mode of action of β-amylase on starch oligosaccharides. Stärke 15:425-431, 1963.
4. Summer, R., French, D. Action of β-amylase on branched oligosaccharides. J. Biol. Chem. 222:469-477, 1956.
5. Hehre, E.J., Okada, G., Genghof, D.S. Configurational specificity: Unappreciated key to understanding enzymic reversions and *de novo* glycosidic bond synthesis. I. Reversal of hydrolysis by α-, β-, and glucoamylases with donors of correct anomeric form. Arch. Biochem. Biophys. 135:75-89, 1969.
6. Hehre, E.J., Kitahata, S., Brewer, C.F. Catalytic flexibility of glycosylase. The hydration of maltal by β-amylase to form 2-deoxymaltose. J. Biol. Chem. 261:2147-2153, 1986.
7. Kitahata, S., Chiba, S., Brewer, C.F., Hehre, E.J. Mechanism of maltal hydration catalyzed by β-amylase. Role of protein structure in controlling the steric outcome of reactions catalyzed by a glycosylase. Biochemistry 30:6769-6775, 1991.
8. Mikami, B., Hehre, E.J., Sato, M., Katsube, Y., Hirose, M., Morita, Y., Sacchettini, J.C. The 2.0-Å resolution structure of soybean β-amylase complexed with α-cyclodextrin. Biochemistry 32:6836-6845, 1993.
9. Mikami, B., Degano, M., Hehre, E.J., Sacchettini, J.C. Crystal structures of soybean β-amylase and maltal: Active site components and their apparent roles in catalysis. Biochemistry 33:7779-7787, 1994.
10. Kraulis, P.J. MOLSCRIPT: A program to produce both detailed and schematic plots of protein structures. J. Appl. Crystallogr. 24:946-950, 1991.
11. Pujadas, G., Ramírez, F.M., Valero, R., Palau, J. Evolution of β-amylase: Patterns of variation and conservation in subfamily sequences in relation to parsimony mechanisms. Proteins 25:456-472, 1996.
12. Kunikata, T., Nishimura, S., Nitta, Y. Maltal binding mechanism and a role of the mobile loop of soybean β-amylase. Biosci. Biotechnol. Biochem. 60:1104-1108, 1996.
13. Coutinho, P.M., Dowd, M.K., Reilly, P.J. Automated docking of monosaccharide substrates and analogues and methyl α-acarviosinide in the glucoamylase active site. Proteins 27:235-248, 1997.
14. Coutinho, P.M., Dowd, M.K., Reilly, P.J. Automated docking of isomaltose analogues in the glucoamylase active site. Carbohydr. Res. 297:309-324, 1997.
15. Coutinho, P.M., Dowd, M.K., Reilly, P.J. Automated docking of glucosyl disaccharides in the glucoamylase active site. Proteins 28:162-173, 1997.
16. Coutinho, P.M., Dowd, M.K., Reilly, P.J. Automated docking of α-(1,4)- and α-(1,6)-linked glucosyl trisaccharides in the glucoamylase active site. Ind. Eng. Chem. Res. 37:2148-2157, 1998.
17. Goodsell, D.S., Olson, A.J. Automated docking of substrates to proteins by simulated annealing. Proteins 8:195-202, 1990.
18. Goodsell, D.S., Lauble, H., Stout, C.D., Olson, A.J. Automated docking in crystallography: Analysis of the substrates of aconitase. Proteins 17:1-10, 1993.
19. Goodsell, D.S., Morris, G.M., Olson, A.J. Docking of flexible ligands. Applications of AutoDock. J. Mol. Recog. 9:1-5, 1996.

20. Vriend, G., Hooft, R. W. W., van Aalten, T. WHAT IF manual. European Molecular Biology Laboratory, Heidelberg, Germany, 1997. http://www.swift.embl-heidelberg.de/whatif/.
21. Imberty, A., Hardman, K.D., Carver, J.P., Pérez, S. Molecular modelling of protein-carbohydrate interactions: Docking of monosaccharides in the binding site of concanavalin A. Glycobiology, 1:631-642, 1991.
22. Pérez, S., Meyer, C., Imberty, A. Practical Tools for molecular modeling of complex carbohydrates and their interactions with proteins. In: "Modelling of Biomolecular Structures and Mechanisms." A. Pullman, J. Jortner, B. Pullman (eds.) Dordrecht, Netherlands: Kluwer Academic Publishers, 1995:425-454.
23. Dowd, M.K., Zeng, J., French, A.D., Reilly, P.J. Conformational analysis of the anomeric forms of kojibiose, nigerose, and maltose using MM3. Carbohydr. Res. 230:223-244, 1992.

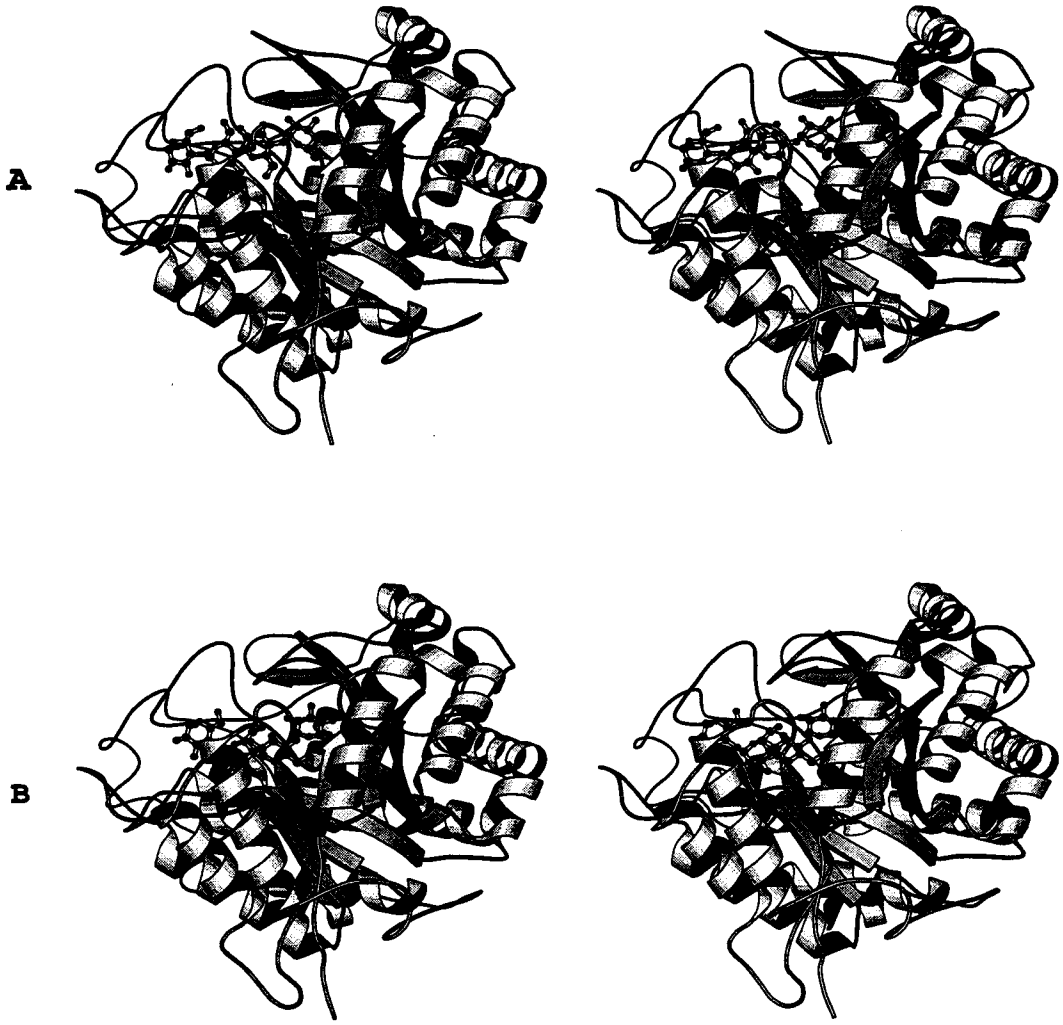

Fig. 1. Stereoscopic plots of soybean β-amylase visualized with Molscript.[10] **A**: Side view with open flap and docked top-energy conformer. **B**: Side view with closed flap and docked top-energy conformer. The flap clearly pushes Glc_B and Glc_C deeper into the cleft and closer to catalytic residues Glu186 and Glu380.

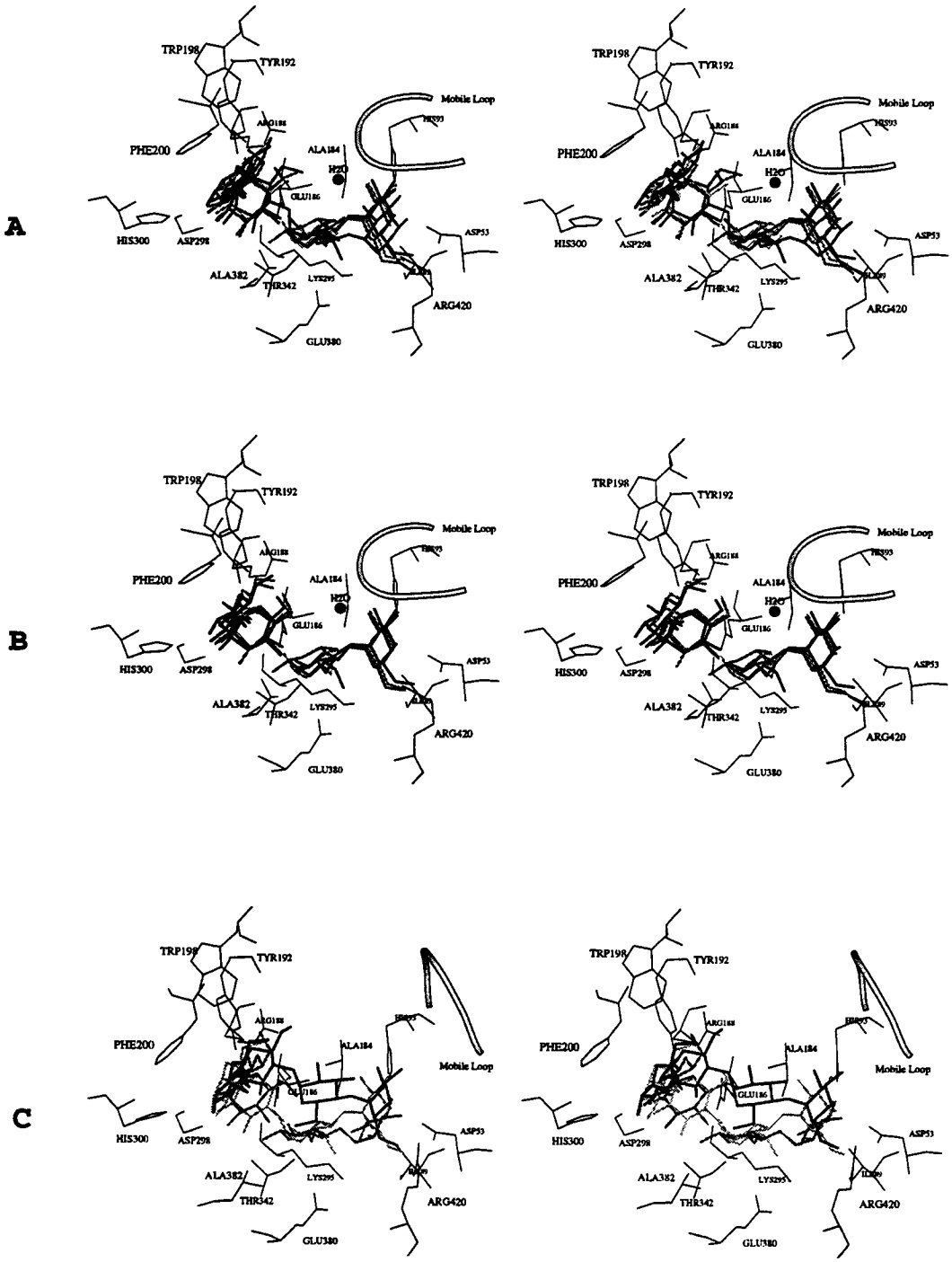

Fig. 2. Stereoscopic views of docked structures in the β-amylase active site visualized with Molscript.[10] Residues surrounding subsites -2,-1,+1,+2 and the catalytic water molecule are shown. **A:** Two α-maltose molecules (light grey), two β-maltose molecules (medium grey), one α-maltotetraose molecule (dark grey), crystal structure of two β-maltose molecules (black), all with a closed flap. **B:** Two α-2-deoxymaltose molecules (light grey), two β-2-deoxymaltose molecules (dark grey), crystal structure of two β-2-deoxymaltose molecules (black), all with a closed flap. **C:** Two α-maltose molecules (light grey), two β-maltose molecules (medium grey), and one α-maltotetraose molecule (dark grey), all with an open flap. The disaccharides can bind inside the active site when the flap is open, but maltotetraose cannot.

Table I. Docking of maltose into the closed-flap configuration

Cluster rank	Number in cluster	Total energy (kcal/mol)	Internal energy (kcal/mol)	Intermolecular binding energy (kcal/mol)	RMSD from **1byb** (Å)		
					-2,-1	-1,+1	+1,+2
α-Maltose (1400 runs considered)							
1	39	-110.33 [-109.31]*	1.27 [1.34]	-111.60 [-110.65]	0.43 [0.44]	3.80 [3.79]	6.67 [6.67]
2	98	-107.66 [-106.71]	-9.61 [-12.95]	-98.05 [-93.76]	6.72 [6.70]	3.90 [3.87]	0.49 [0.52]
3	53	-106.26 [-104.98]	4.52 [4.65]	-110.78 [-109.63]	0.54 [0.54]	3.94 [3.91]	6.77 [6.77]
4	118	-106.19 [-105.08]	-15.04 [-13.96]	-91.15 [-91.12]	6.72 [6.69]	3.84 [3.82]	0.52 [0.55]
5	135	-103.87 [-102.34]	-7.70 [-8.99]	-96.17 [-93.35]	1.25 [1.26]	3.55 [3.53]	6.53 [6.51]
β-Maltose (1300 runs considered)							
1	188	-108.75 [-106.90]	0.46 [0.63]	-109.21 [-107.54]	0.61 [0.60]	3.60 [3.62]	6.57 [6.58]
2	85	-105.99 [-104.31]	-15.59 [-12.95]	-90.40 [-91.35]	1.24 [1.25]	3.54 [3.48]	6.51 [6.47]
3	15	-103.37 [-102.21]	1.05 [0.83]	-104.42 [-103.04]	0.78 [0.78]	3.58 [3.58]	6.64 [6.65]
4	11	-102.36 [-101.65]	-8.04 [-8.23]	-94.32 [-93.42]	0.79 [0.79]	3.67 [3.67]	6.69 [6.70]
5	89	-101.19 [-100.45]	-9.49 [-8.83]	-91.70 [-91.62]	6.74 [6.71]	3.97 [3.93]	0.61 [0.59]

*Average.

Table II. Docking of 2-deoxymaltose into the closed-flap configuration

Cluster rank	Number in cluster	Total energy (kcal/mol)	Internal energy (kcal/mol)	Intermolecular binding energy (kcal/mol)	RMSD from **1byd** (Å)		
					-2,-1	-1,+1	+1,+2
α-2-Deoxymaltose (800 runs considered)							
1	222	-108.76 [-107.08]*	0.95 [0.75]	-109.71 [-107.83]	0.74 [0.73]	3.58 [3.62]	6.58 [6.60]
2	88	-108.05 [-107.39]	-5.39 [-4.84]	-102.66 [-102.54]	0.75 [0.76]	3.67 [3.66]	6.69 [6.68]
3	170	-106.24 [-104.05]	-12.42 [-12.83]	-93.82 [-91.23]	6.69 [6.71]	3.73 [3.76]	0.37 [0.43]
4	1	-102.13 [-102.13]	-14.18 [-14.18]	-87.95 [-87.95]	6.72 [6.72]	3.81 [3.81]	0.55 [0.55]
5	64	-99.80 [-97.93]	-9.32 [-6.44]	-90.48 [-91.49]	1.15 [1.07]	3.42 [3.42]	6.62 [6.56]

β-2-Deoxymaltose (900 runs considered)							
1	87	-108.32 [-106.72]	-2.31 [-1.43]	-106.01 [-105.29]	0.81 [0.83]	3.42 [3.41]	6.47 [6.46]
2	108	-104.54 [-103.29]	-9.97 [-7.44]	-94.57 [-95.85]	6.76 [6.80]	3.74 [3.79]	0.44 [0.41]
3	72	-104.21 [-102.73]	-1.42 [-1.05]	-102.79 [-101.68]	0.78 [0.80]	3.51 [3.49]	6.49 [6.49]
4	127	-102.93 [-102.00]	-12.51 [-12.35]	-90.42 [-89.65]	6.78 [6.80]	3.82 [3.83]	0.49 [0.49]
5	7	-100.75 [-100.16]	-1.78 [-2.52]	-98.97 [-97.64]	0.99 [0.98]	3.37 [3.43]	6.50 [6.58]

*Average.

Table III. Docking of α-maltotetraose into the closed-flap configuration

Cluster rank	Number in cluster*	Total energy (kcal/mol)	Internal energy (kcal/mol)	Intermolecular binding energy (kcal/mol)	RMSD from **1byb** (Å) -2,-1,+1,+2
1	277	-154.66 [-153.98]†	-12.47 [-11.04]	-142.19 [-142.93]	0.79 [0.78]
2	53	-144.05 [-143.83]	-7.68 [-7.53]	-136.37 [-136.31]	0.73 [0.73]
3	27	-138.67 [-138.02]	8.54 [7.57]	-147.21 [-145.59]	0.80 [0.81]
4	1	-127.27 [-127.27]	2.47 [2.47]	-129.74 [-129.74]	0.77 [0.77]
5	99	-112.30 [-112.26]	-1.10 [-1.09]	-111.20 [-111.17]	1.52 [1.52]

*800 runs considered.

†Average.

CUSTOMIZED INJECTABLE PLURONIC® GELS FOR SUSTAINED DRUG DELIVERY

Theodore Moore, Michael Oberhaus, Nita Pandit[a], and Surya Mallapragada
Department of Chemical Engineering, Iowa State University, Ames, IA 50011
[a]College of Pharmacy and Health Sciences, Drake University, Des Moines, IA 50311

Introduction

Controlled release is important in the design of drug products, as it reduces fluctuations in plasma levels, maintains drug concentrations within therapeutic limits for long periods, and reduces the amount of drug needed. A controlled release system reduces the dosing frequency and enhances patient compliance. A simple drug delivery system, customized with a suitable and predictable release rate that can be easily formulated as needed in a pharmacy for a variety of drugs, would be very attractive.

Poloxamers or Pluronics® (BASF) are polyethylene oxide-polypropylene oxide-polyethylene oxide copolymers that form micelles and thermoreversible gels. These gels, when injected, provide sustained release delivery of a variety of drugs[1-4]. Pluronic® F127 (F127), which has a nominal molecular weight of 12,500, has been the most widely used of these copolymers in pharmaceutical systems. Aqueous solutions of F127 of >20% w/w are liquid when refrigerated, but gel upon warming[5]. Gel formation occurs at a critical gel formation temperature (T_1) and further heating results in gel melting at a temperature T_2. For a 20% F127 gel, T_1 is 21°C, and T_2 is 75°C [6]. Thus, the formulation can be injected into the body as a liquid at a temperature below 21°C, will gel in the body (37°C), and will then provide sustained release of drug for an extended period of time. This approach eliminates the need to implant devices in the body to deliver drugs.

Pluronic copolymers have a structure enabling them to form micelles in aqueous solutions[7-11]. The ability of F127 to form micelles also made it attractive to use with hydrophobic drugs. Such drugs would be solubilized in the interior of the micelle, while polar drugs would remain in the outer aqueous region of the gel. F127 systems can stabilize proteins, and so these systems could be very useful to deliver unstable proteins[12]. It is possible to design customized Pluronic F127 gels with predictable dissolution rates by changing the concentration of F127, or by including certain additives, like salts. It has been shown by Pandit and Kisaka[6] that buffers and other salts added to the gels can significantly alter T_1 and T_2.

Methods

Gel Dissolution

The F127 gels were prepared by weight, using the cold method[5]. While cold, 20 g of the polymer was placed in a dissolution container with known surface area. Four different types of containers with varying areas were used to demonstrate the relationship between dissolution rate and surface area. The system was allowed to gel by placing it in a 37°C oven. The gel container was carefully placed in a US Phamacopeia dissolution apparatus (Figure 1) containing various volumes of water maintained at 37°C. The volume of water did not affect the dissolution rate measured, and 800 mL of water was subsequently used for all experiments. The dissolution of gel was measured gravimetrically by the method of Bhardwaj and Blanchard[3], by weighing the gel periodically. Dissolution studies were carried out under both static and stirred (20-100 rpm) conditions. The effect of temperature (25-45°C) on the dissolution rate was also examined.

Drug Release

The rate of drug release was measured by periodically removing a small sample (3 mL) of the dissolution medium, diluting if necessary, and determining the concentration of the dissolved drug

spectrophotometrically. The absorbance of propranolol was measured at a wavelength of 290 nm, and that of metronidazole at a wavelength of 319.5 nm. The concentrations were calculated from appropriate calibration curves.

Volume Fraction Measurements

The volume fraction of water in the gel was measured using a buoyancy technique. The weight of the gel in air (W_a) was measured. The sample was immersed in heptane[13], a non-solvent for the polymer, and the weight of the gel in heptane (W_n) was also recorded. The gel was then dried completely in an oven at 50°C. The weights of the dried sample in air (W_a') and in heptane (W_n') were recorded. Using Archimedes' principle, the volumes of the dry (V_d) and swollen polymer (V_s) were computed according to the relations

$$V_s = (W_a - W_n) / \rho \qquad \text{and} \qquad V_d = (W_a' - W_n') / \rho$$

where ρ is the density of heptane. The volume fraction of polymer in the gel, υ_2, is

$$\upsilon_2 = V_d / V_s$$

Results and Discussion

Figure 2 illustrates the key finding of our work, that release of a drug from the gels is entirely dependent on the dissolution rate of the gel, and is independent of the properties of the drug. Figure 2 includes data from several experiments with three different drugs, done under conditions of varying drug loading, F127 loading, surface area of dissolution and stirring. In all these situations, the relationship between drug released and gel dissolved is linear and proportional.

The rate of drug release needs to be customized to the properties of the drug and the dosage needs of the patient. The most direct way to do this is to change the loading of F127 in the gel. Figure 3 shows the influence of F127 concentration on the fraction of gel dissolved and hence the fraction of propranolol released at 37°C and static conditions. We expect that our static set-up most closely resembles *in vivo* conditions, and thus gives a reasonable estimate of expected release rates. As the concentration of F127 in the gel increases, the gel dissolution rate decreases significantly. In all cases, the zero-order gel dissolution and drug release is observed, which is characteristic of phase erosion or dissolving systems[14].

The drug loading can be used to tailor the amount of drug released, as seen in Figure 4. However, the drug loading had no significant effect on the rate at which the gel dissolves. At the beginning of the project, we had expected that two other variables, temperature and salts, would have a significant and predictable influence on release rates. The expected influence of salts was based on prior observations that their presence changes the gelation transition temperatures of F127 gels[6]. Table 1 shows the influence of sodium sulfate on the dissolution of a 20% F127 gel at 37°C and at 20 rpm. The F127 dissolution rate was calculated from the measured release rate of propranolol.

It is apparent from these data that Na_2SO_4 has little effect on the dissolution rate of the gel, and thus cannot be used to customize release rates of drugs. We have seen similar trends with the other salts studied (NaCl, Na_3PO_4).

Conclusions and Future Work

We have observed that the release of small molecular weight drugs is controlled by the gel dissolution rate, irrespective of the type of drug used. In all cases, we have obtained zero-order drug release. This makes these systems easy to formulate for any type of drug since the release

Table 1. Influence of salts on gel dissolution.

Na_2SO_4 conc. (% w/w)	F127 dissolution rate ($mg.cm^{-2}.min^{-1}$)
0.0	1.04
0.5	0.997
1.0	1.02
1.5	1.06
2.0	0.995

rate depends only on the gel dissolution rate. Based on our current results, it appears that F127 concentrations and drug loadings are the only variables that can be modified to alter release rates. In the future, we would like to explore how other hydrophilic polymers (other PEO-PPO-PEO block copolymers, celluloses and modified celluloses) can be used to alter gel properties and customize drug release rates for specific situations.

References

1. Suh, H. and Jun, H. W. *Int. J. Pharm.* **1996**, 129, 13.
2. Pec, E. A., Wout, Z. G., and Johnston, T. P. *J. Pharm. Sci.* **1992**, 81, 626.
3. Bhardwaj, R. and Blanchard J. *J. Pharm. Sci.* **1996**, 85, 915.
4. Stratton, L., Dong, A., Manning, M and Carpenter, J. *J. Pharm. Sci.* **1997**, 86,1006.
5. Schmolka, I. R. *J. Biomed. Mater. Res.* **1972**, 6, 571.
6. Pandit, N. and Kisaka, J. *Int. J. Pharm.* **1996**, 145, 129.
7. Rassing J., McKenna, W., Bandopadhyay, S. and Eyring E. *J. Mol. Liquids.* **1984**, 27, 165.
8. Linse, P. and Malmsten, M. *Macromolecules.* **1992**, 25, 5434.
9. Malmsten, M. and Lindman, B. *Macromolecules.* **1992**, 25, 5440.
10. Linse, P. *Macromolecules.* **1993**, 26, 4437.
11. Pandit, N. and Wang, D. *Int. J. Pharm.* **1998**, 167, 183.
12. Johnston, T. and Miller, S. *J. Parenteral Drug Assoc.* **1985**, 39, 83.
13. Ngui, M. O. and Mallapragada, S. K. *J. Polym. Sci. Polym. Phys.* (in press).
14. Mallapragada, S. K., Colombo, P. and Peppas, N. A. *J. Biomed. Mater. Res.*, **1997**, 36, 125.

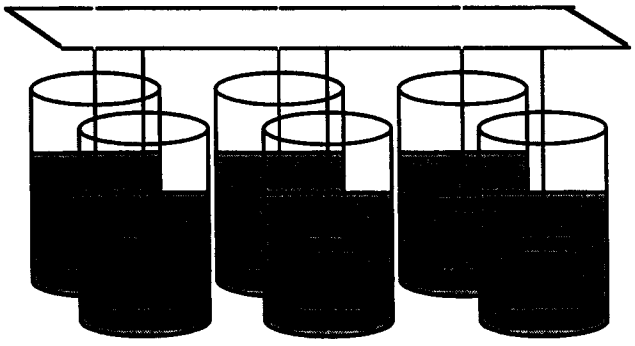

Figure 1. Schematic of experimental setup (USP Dissolution Cell)

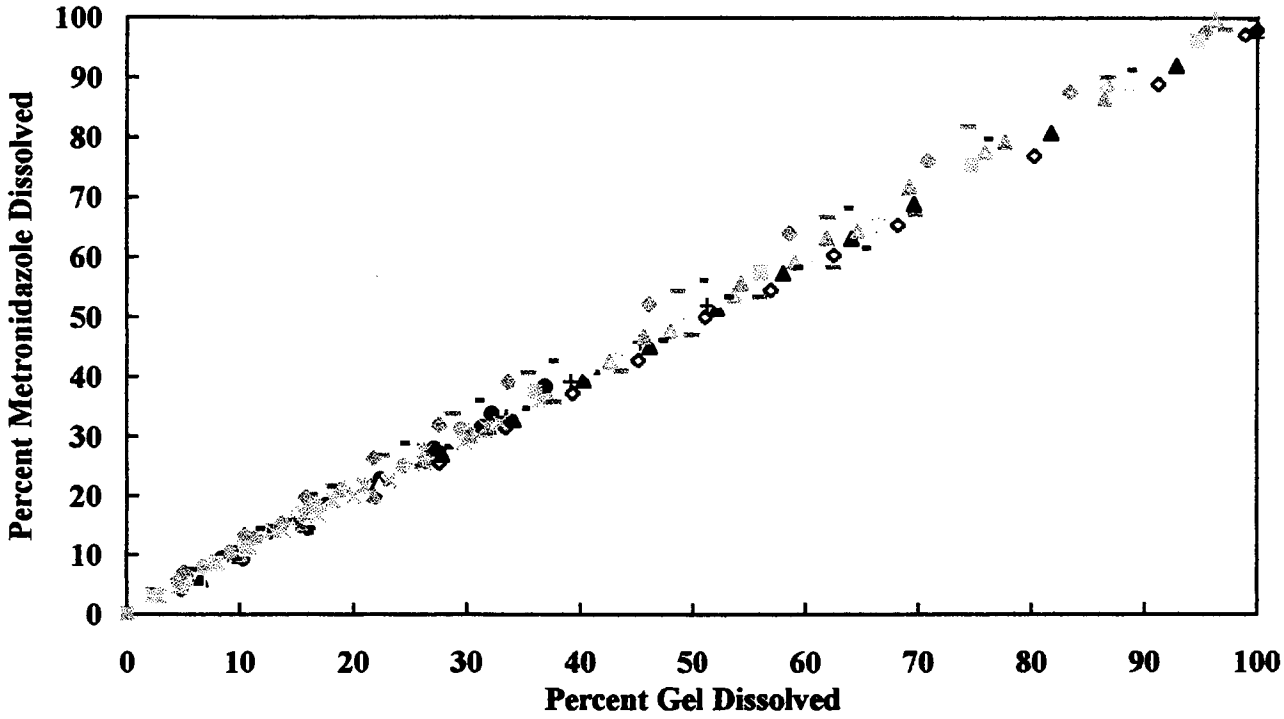

Figure 2. Percentage of drug dissolved as a function of percentage of gel dissolved for various drugs, gel concentrations, drug loadings, surface area of dissolution and stirring.

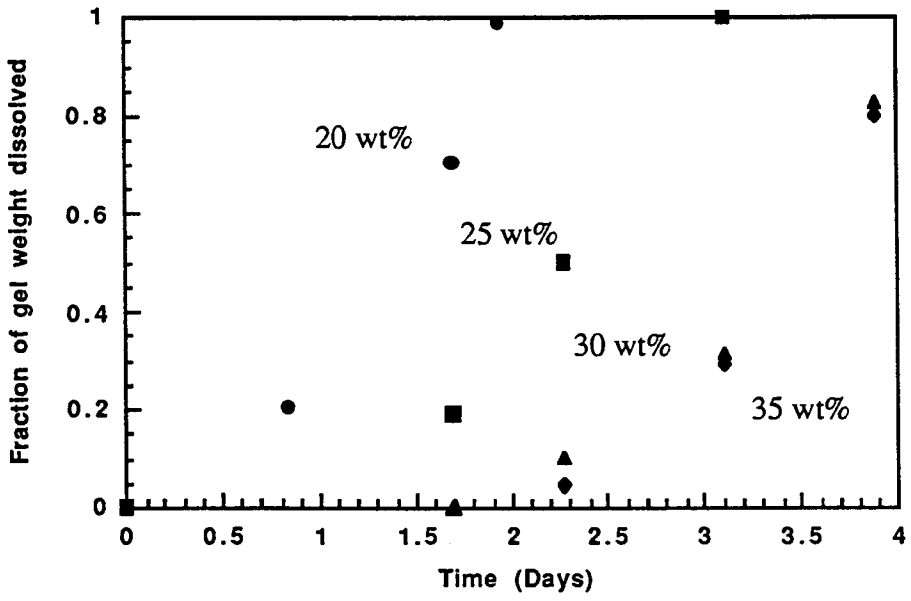

Figure 3. Effect of F127 loading on gel dissolution under static conditions.

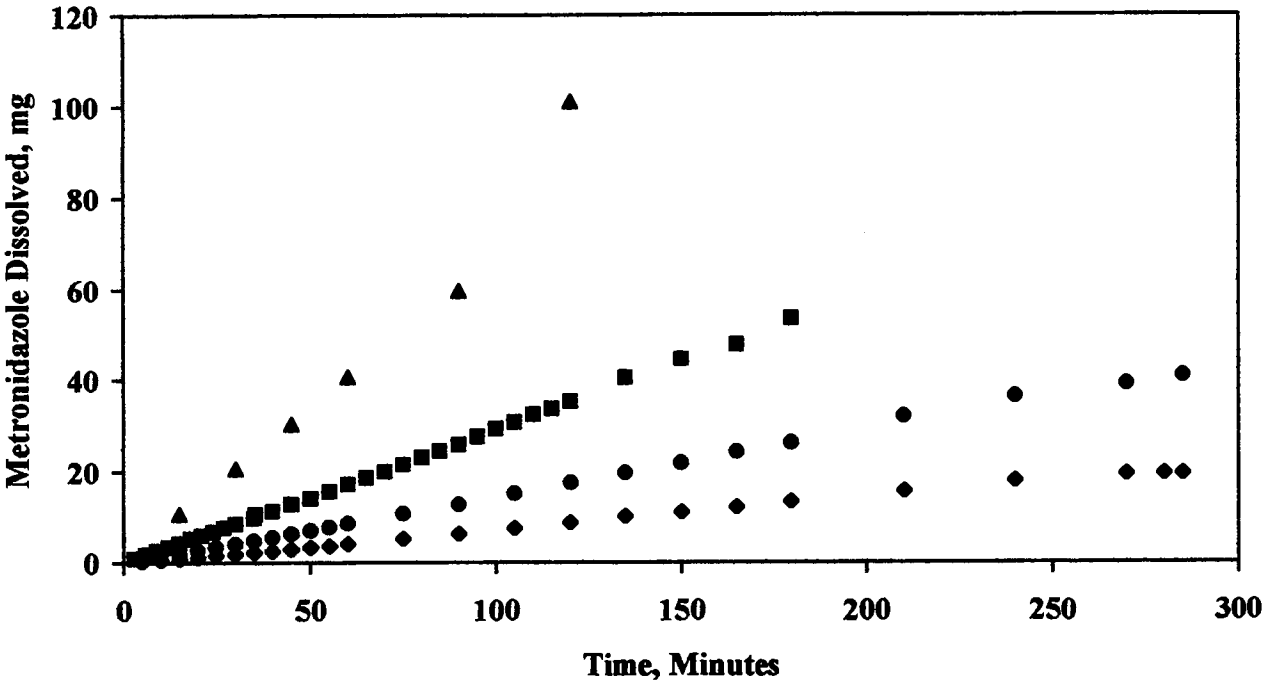

Figure 4. Effect of drug loading on gel dissolution: (▲) 0.8 wt% metornidazole; (■) 0.4 wt% metronidazole; (●) 0.2 wt% metronidazole and (◆) 0.1 wt% metronidazole.

EVALUATION OF SURGICAL LIMB LENGTHENING THROUGH RADIOGRAPHIC ABSORPTIOMETRY

Sridhar Sunderam[1], Brad W. Olney,[2] and Marylee Z. Southard[1], [1]Department of Chemical and Petroleum Engineering, University of Kansas, Lawrence, KS 66045, and [2]Department of Orthopedic Surgery, University of Kansas Medical Center, Kansas City, KS 66160

Abstract

The process of bone regeneration in limb lengthening by distraction osteogenesis is usually monitored and evaluated by visual inspection of radiographic exposures by a qualified surgeon, who must decide whether healing is satisfactory and when the external fixator can be removed and normal load-bearing permitted. This diagnosis is purely qualitative and requires considerable experience; moreover, some uncertainty exists as to whether bone that is judged to have healed from a radiograph will be comparable in mechanical strength to the untreated contralateral segment. In this pilot study, tibial lengthenings of 1 cm are performed on six rabbits that are sacrificed sequentially to have the extent of healing in the lengthened tibia estimated. Radiographs of the severed limbs are taken from two views along with an aluminum step wedge for calibration, and the images are digitized and analyzed using a computer program developed for this purpose on Matlab. The image analysis yields an axial measure of bone mineral density (BMD) and is used to compare the BMD of the lengthened bone with the contralateral control and also with measurements made in rabbits sacrificed at other times. The precision of the measurement across the control group of limbs was about 10%. Over the consolidation period, the BMD in the lengthened limbs approached the control value before dropping briefly; this is attributed to resorption before the remodeling phase sets in. The data were inadequate to determine the extent of bone healing. A broader study involving more samples over a longer duration is indicated.

Introduction

Limb lengthening procedures are required to treat congenital limb length discrepancy[1] as well as some cases of fracture and bony nonunion. Ilizarov's technique of *distraction osteogenesis* is today the most popular method in use for limb lengthening. This is based on the observation that gradual stretching of the soft callus in a fractured bone promotes osteogenesis or bone formation[2]. In the Ilizarov technique, the bone segment is subjected to an osteotomy and stabilized by an external fixator. After a latency period during which a fibrous callus forms between the cut surfaces, the two fragments are distracted away from each other at a controlled rate to stretch the callus until the desired length is reached. The distraction is stopped and the wound is allowed to heal until the callus bridges the gap and is remodelled into normal compact bone. Then the fixator is removed and full load-bearing is permitted. The progress of healing during the consolidation phase of distraction osteogenesis is usually followed by inspection of plain-film radiographs at weekly or fortnightly intervals. This evaluation is purely qualitative where the physician employs his expertise to make a diagnosis regarding the structural integrity of newly formed bone based on its radiographic appearance. The fixator should neither be removed before the member is stable, nor should it be kept on too long, since disuse leads to loss of bone mass by resorption. Hence it would be useful to determine accurately the optimal duration of the fixation period. A non-invasive, quantitative measurement technique that can provide this information would be invaluable to the orthopedic surgeon. In this study, radiographic absorptiometry

is used to measure and track the BMD during the bone consolidation phase of tibial lengthenings performed on rabbits. The objective is to quantify the extent of healing through the BMD. Achievement of this goal would make it possible to determine the optimal duration of the fixation period.

Methods

Tibial lengthenings of 1 cm were performed on six female white rabbits. A latency of one week was permitted following the osteotomy and before distraction, which was at the rate of 1 mm/day. One rabbit was sacrificed every three to five days after distraction was stopped, and both limbs were extracted from the body and radiographed simultaneously with an aluminum step wedge, which serves as a reference material of known density (2.67 g/cm^3). The radiographic exposures were scanned at a resolution of 75 dots/inch into 8-bit digital gray images of the JPEG format and analyzed by a program developed using Matlab (Mathworks, MA) on a Sun/Solaris 2 workstation. The attenuation of x-ray intensity on passage through a material depends on the material density and thickness. The steps of the reference wedge are of known height. Therefore, the intensity of the digital image can be calibrated in terms of its aluminum equivalent (thickness). Multiplying this by the material density gives a local areal density X, which varies from pixel to pixel across the bone image. Integrating X along a chosen cross-section (normal to the long axis) of the bone in the region of interest gives the bone mineral content[3] (BMC) measured in g/cm. The BMC divided by the cortical cross-section A_c of the bone gives the mean cortical BMD in g/cm^3. Here, we assume that the cross-section is a cylindrical annulus. Hence,

$$BMD\left(g/cm^3\right) = \frac{BMC(g/cm)}{A_c\left(cm^2\right)} = \frac{\int_{D_o} X dr}{\frac{\pi}{4}\left(D_o^2 - D_i^2\right)}$$

D_o and D_i are determined by locating the bone edges and local maxima for the cross-sectional X profile. Using this technique, BMD was measured along the axis of each lengthened bone segment and the internal control segment at intervals of 1/3 mm in the 4-cm long region between the inner pins of the external fixator. An average of these forty values was recorded as the mean BMD of the specimen.

Results and Discussion

Figure 1 shows the mean BMD for the defective tibia as a function of time. The mean and standard deviation of the control specimens are given by the continuous and dotted lines, respectively. The measurement was precise to within about 10% for the six control tibiae. The six-week study of tibial lengthening in rabbits showed a rise in BMD towards the control value interrupted by a brief dip, which could be attributed to a brief resorption phase before remodeling of the bone into the compact form takes place. The number of samples was inadequate to determine the time required for complete healing. Nor was it possible to make conclusions regarding the statistical significance of the data since only one sample was available at each time. However, it was demonstrated that the technique used here for measuring BMD is a viable tool for obtaining

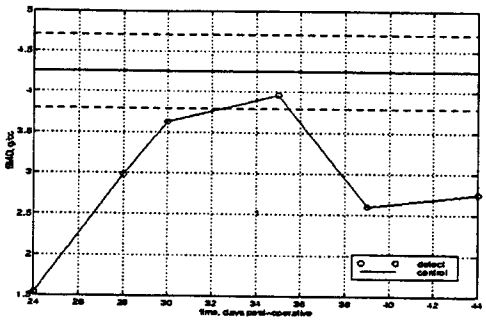

Figure 1. Mean BMD as a function of time.

dynamic data. Mechanical torsion tests are currently being conducted on the twelve specimens to correlate the measured BMD with the yield strength of the callus.

References

1. Dahl, M.T., Limb length discrepancy, *Pediatr. Clin. North Am.*, **43**, 849-865, 1996.
2. Maffuli, N. and Fixsen, J.A., Distraction osteogenesis in congenital limb length discrepancy: A review, *J. Royal Coll. Surg. Edinb.*, **41**, 258-264, 1996.
3. Huddleston, P.L., Bone Densitometry, CRC Press, Boca Raton, 1988.